Spring 6-18-2015

Interpretation of Centrifuge Test Results of the Seismic Response of Temporary Braced Excavations near Tall Buildings

Christina Louise Jones
University of Colorado at Boulder, chrjones11@gmail.com

Recommended Citation
Jones, Christina Louise, "Interpretation of Centrifuge Test Results of the Seismic Response of Temporary Braced Excavations near Tall Buildings" (2015). *Civil Engineering Graduate Theses & Dissertations*. 143.
https://scholar.colorado.edu/cven_gradetds/143

INTERPRETATION OF CENTRIFUGE TEST RESULTS OF THE SEISMIC RESPONSE OF TEMPORARY BRACED EXCAVATIONS NEAR TALL BUILDINGS

Presented by

CHRISTINA LOUISE JONES

A thesis submitted to the
Faculty of the Graduate School of the
University of Colorado in partial fulfillment
of the requirement for the degree of
Master of Science
Department of Civil, Environmental, and Architectural Engineering
2015

This thesis entitled:

Interpretation of Centrifuge Test Results of the Seismic Response of Temporary Braced Excavations near Tall Buildings

written by Christina Louise Jones

has been approved for the Department of Civil, Environmental, and Architectural Engineering

____
Dr. Shideh Dashti

____
Dr. Dobroslav Znidarcic

Date_______________

The final copy of this thesis has been examined by the signatories, and we

Find that both the content and the form meet acceptable presentation standards

Of scholarly work in the above mentioned discipline.

Jones, Christina Louise

Interpretation of Centrifuge Test Results of the Seismic Response of Temporary Braced Excavations near Tall Buildings

Thesis directed by Assistant Professor Shideh Dashti

Underground structures such as cut-and-cover box structures and retaining wall systems have performed relatively well during past seismic events. However, notable cases such as the failure of the Daikai Subway Station during the 1994 Kobe Earthquake show the importance of the seismic design of these types of structures. Braced excavations are a type of underground structure used to provide space for the construction of cut-and-cover tunnels, basements, foundations, and other permanent underground structures. Even though temporary, braced excavations need to be designed to withstand seismic loads.

Current seismic design of underground structures assumes the case of isolation with no adjacent buildings. In reality, underground structures such as braced excavations and subway systems are located in densely populated downtown areas, with adjacent buildings. This research aims to provide insight into the seismic response of braced excavations near tall buildings.

Data from three dynamic centrifuge tests were analyzed to evaluate soil-structure-underground structure-interaction (SSUSI) near a temporary braced excavation. Dry, medium dense, Nevada sand was used as the test soil. The first test studied the braced excavation in isolation with no adjacent buildings. The second and third tests studied the same excavation with an adjacent midrise and highrise building, respectively. Various methods of measuring small-strain soil properties in the far-field are explored in this thesis and compared. The seismic response of the braced excavation are presented during the three centrifuge tests in terms of racking displacements, dynamic lateral earth pressures, and bending moments along the excavation walls as well as axial forces on struts to evaluate the seismic impact of an adjacent tall building on the performance of a braced excavation.

The conclusions and observations presented in this thesis are preliminary and based on experimental results alone. Final, generalized design recommendations cannot be drawn from these observations. Results from numerical simulations currently being performed by the University of Illinois-Urbana under the direction of Professor Hashash will be used in addition to these experimental results to provide design recommendations in the future.

Acknowledgements

I would like to start with a big thank you to my family! I am utmost thankful for their love and support throughout my whole life. I would not have been able to gain my college experience without their generosity and encouragement over the last six years. My friends have provided essential mental escapes from academic life and have helped me discover new passions and appreciations. I have been able to share many amazing adventures with my boyfriend, Matt, over the last three years, and he has supported my goals unconditionally. I must also thank my great home state of Colorado. I am so pleased I chose to stay for my college education, both undergraduate and graduate. It has provided endless and necessary distractions. Even though I have chosen to move away for a while, it will always be home, and I will come back to continue enjoying all it has to offer.

Thank you to PhD Student, Kenny Gillis, an outstanding individual whom I worked with and learned from during this research. Kenny was the lead PhD student on this project. Kenny has not only been an exceptional research mentor, he has also been a great friend.

I completed my undergraduate degree at CU Boulder before continuing on into the graduate program. I would like to thank all of my professors during my undergraduate career. Particularly, I would like to thank Dr. Znidarcic for being my first geotechnical engineering professor and undergraduate advisor. He encouraged me to continue my studies in graduate school.

This research is a collaboration between the University of Colorado at Boulder and the University of Illinois Urbana-Champaign. Professor Dashti, my graduate advisor and PI of this research project, led the experimental component of this research. Professor Youssef Hashash at the University of Illinois-Urbana, Co-PI, and his PhD students, Maria Ines Romero and Michael Musgrove, led the numerical component of this research. Together, the two teams designed the centrifuge experiments and the structures involved. I joined and participated with this research team during the final experimental component of the overall project. I give credit to the rest of the team for the design of the centrifuge tests discussed in this thesis, as this was completed before I joined. Kenny Gillis performed the three centrifuge tests discussed in this thesis with my help only during the third test. A huge acknowledgement is given to this research team as their work and contributions are used throughout this thesis. I am also very grateful for the

discussions we had during our virtual meetings. Professor Hashash provided great feedback, which was challenging and motivating throughout this work.

Finally, I would like to thank my great advisor, Professor Shideh Dashti. First, she has been a great teacher during my undergraduate and graduate careers. She spurred my interest in geotechnical earthquake engineering and invited me into her amazing research group. She also immensely helped me throughout this research. Our weekly meetings kept me organized and directed. She was always responsive and willing to help. I thank her for her encouragement, advice, time, and effort in helping me complete this thesis.

The centrifuge experiments were performed at the University of California Davis Center for Geotechnical Modeling (UCD-CGM). I would like to thank the staff at this center for their help and input during the construction and testing of the centrifuge models. This work is supported by the NSF under Grant No. 11-34968. Any opinions, findings, and conclusions or recommendations expressed in this material are those of the author and do not necessarily reflect the views of the National Science Foundation. We would also like to acknowledge Hushmand Associates, Inc. and the Los Angeles Department of Water and Power (LADWP) for providing partial funding towards the purchase of tactile pressure sensors that were used extensively in this research and others.

Table of Contents

List of Tables

List of Figures

1 - INTRODUCTION

Today, the majority of the world's population lives in urban areas that continue to grow. Cities around the world need to construct new infrastructure in closer vicinity to each other to accommodate the growing population in a limited space. In dense, urban environments, using the underground space is essential to construct basements and foundations of tall buildings as well as underground transportation facilities that are a critical component of sustainable cities, Figure 1-1. The economy of cities ranging in scale from San Francisco to New York City and across the world from Mexico City to Tokyo depends on the resilience of the infrastructure. Therefore, in areas that are seismically active, these underground structures need to be designed to safely withstand earthquake loading as well as the load from adjacent tall buildings that are increasingly found in their vicinity.

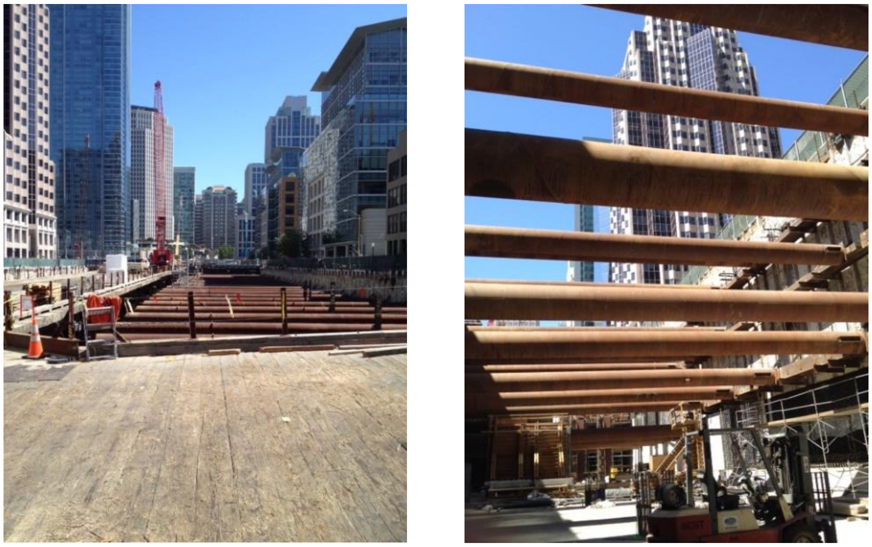

Figure 1-1. A temporary braced excavation currently utilized for the construction of the new Transbay terminal in downtown San Francisco, CA.

Even though temporary braced excavations are temporary structures typically used to provide space for the construction of a permanent box structure, when in a seismically active region, they too need to be designed to withstand earthquake loading. The state of practice for the seismic design of braced excavations relies either on simplified procedures that assume the excavation is in isolation (i.e., no adjacent structures present) or numerical tools that have not been previously validated against experimental studies. Tall buildings with multistory basements have the potential to alter the ground motions in the foundation soil and transmit significant forces to the adjacent underground structure due to their large base shear and moment. Previous analyses have shown that even small levels of shaking can impose these large forces, increasing the required number of internal struts in an excavation. The impact of the transmitted forces on the performance of the adjacent braced excavation is, however, uncertain.

This research involves a series of centrifuge tests to produce well-documented model “case histories” of the response of braced excavations near tall buildings under realistic confinement and loading conditions. The data from these tests are aimed to provide a better understanding of seismic soil-structure-underground structure-interaction (SSUSI). The centrifuge tests were performed at the Center for Geotechnical Modeling at the University of California, Davis (UCD-CGM). The baseline test, referred to as E-No Bldg, examined the seismic response of an open, braced excavation in medium-dense, dry sand (relative density of 55%), when in isolation (no adjacent buildings present). The second test referred to as E-Midrise tested the excavation in close proximity to a midrise building representing a 12-story structure. In the last centrifuge test called E-Highrise, the same braced excavation was placed adjacent to a highrise building, representing the key dynamic properties of a 42-story building. The same sequence of six ground motions was applied to the base of the model container in each experiment. The various ground motions provided unique characteristics in terms of intensity, duration, and frequency content, in order to evaluate the impact of these properties on the response of the soil-structure-underground structure system.

In each centrifuge experiment, the seismic performance of the braced excavation was studied in terms of three key design parameters: 1) displacements, 2) seismic lateral earth pressures, and 3) bending moments on the excavation walls and axial forces on the struts. These parameters were investigated by analyzing the recordings of instruments such as accelerometers, tactile pressure sensors, and strain gauges installed in each centrifuge model. This thesis first provides an overview of the existing literature on the seismic response of braced excavations and the current state of practice. The design and setup of the centrifuge model experiments are then described, followed by experimental results describing the influence of the adjacent tall building on the seismic performance of the braced excavation in terms of the three parameters above. Lastly, preliminary conclusions are made and future research recommendations provided.

2 - BACKGROUND AND MOTIVATION

In a seismically active area, temporary braced excavations must be designed for some level of ground shaking. The level of shaking used for the design of these temporary structures is often lower than that of a permanent box structure, due to their temporary lifespan. Past research has focused on the response of permanent cut-and-cover box structures constructed for underground transportation. Temporary braced excavations are used to provide the space required for the construction of these permanent underground structures, and similar seismic analysis methods developed for permanent structures are used in their design. These seismic analysis methods are primarily based on simplified procedures assuming the structure is in isolation, even though they are commonly constructed in proximity to tall buildings. Previous analyses have shown that tall buildings can apply significant forces to the underlying soil and an adjacent underground structure. The influence of these forces on the performance of temporary braced excavations are not well understood in terms of applied seismic earth pressures, bending moments, and racking deformations. Therefore, their current design may be, at times, overly conservative or insufficient.

2.1 State of Practice for the Seismic Design of Underground Box Structures

In comparison with structures on the surface, underground structures have performed better and induced less damage in previous earthquakes. However, the complete collapse of a modern, underground structure during the 1995 Hyogoken-Nambu Earthquake, the Daikai Subway station in Kobe, Japan, highlighted the importance of their seismic design (Nakamura 1996).

Unlike aboveground structures, the seismic response of underground structures is dominated by the response of the surrounding soil. Due to the constraints the soil imposes, the deformations and inertial response of the buried structure is controlled by the response of the soil mass (Wang 1993; Wu and Penzien 1994; Hashash et al. 2001; Arango 2008). Several factors dictate the extent of shaking induced damage to an underground box structure: (1) the shape, dimensions, and depth of the structure; (2) the properties of the soil or rock surrounding the structure; (3) the underground structure stiffness; and (4) the characteristics of ground shaking (Hashash et al. 2001).

Transverse shear waves transmit the greatest proportion of an earthquake’s energy to underground structures (Hashash et al. 2001) and are therefore the seismic wave of interest for this research. When seismic waves propagate through the soil in a direction perpendicular to the axis of the structure, shear strains are induced, causing transverse displacements of the underground structure (Hashash et al. 2001; Wang 1993). This type of deformation is known as ovaling or racking, which is explored in detail in this research. The extent of racking deformation depends on the racking stiffness of the structure compared to that of the surrounding soil (Hashash et al. 2001).

A soil-structure-interaction (SSI) analysis is often performed for the seismic design of underground box structures to evaluate their transverse deformation due to the deformation of the surrounding soil. Consideration of SSI is important because permanent box structures are commonly constructed with thick, reinforced concrete walls that increase the structure stiffness relative to that of the surrounding soil. Also, estimation of seismic lateral earth pressures requires input of the interactions between the surrounding soil and the structure walls.

Wang (1993) proposed a simplified method for the seismic design of underground rectangular box structures by performing a series of dynamic, finite element analyses. This pseudo-static method calculates racking of the box structure by using information about the surrounding soil. Free-field shear strains at elevations corresponding to the top and bottom of the tunnel provide free-field racking displacements. The strain compatible shear modulus of the free-field soil is used to estimate the soil's shear stiffness. These parameters along with racking stiffness and geometric properties of the box structure are used to calculate the racking displacement of the tunnel.

A primary factor of the seismic response of the soil-structure system is the shear stiffness of the buried structure as compared to the surrounding soil (Wang 1993). This measure of relative stiffness is referred to as the Flexibility Ratio (F), and is defined as:

$$F = \frac{G_M B}{K_S H} \qquad \text{(Eq. 2-1)}$$

where, G_M = mean, strain-compatible, shear modulus of the soil in the free-field, B = the width of the structure, K_S = the racking stiffness of the structure, and H = the height of the underground structure. To calculate the racking stiffness of the structure, a lateral force is applied to the top of the structure while its pinned at its base (e.g., in a frame analysis), and the lateral deflection is observed. The racking stiffness, K_S = force applied divided by the lateral displacement observed at the roof. If the flexibility ratio is less than one, the structure is stiffer than the soil, and vice versa for a flexibility ratio greater than one. Wang (1993) defined the Racking Ratio (R) as:

$$R = \frac{\Delta_{structure}}{\Delta_{free-field}} = \frac{\frac{\Delta_{structure}}{H}}{\frac{\Delta_{free-field}}{H}} = \frac{\gamma_{structure}}{\gamma_{free-field}} \qquad \text{(Eq. 2-2)}$$

where, Δ = racking displacement and γ = shear strain, as shown in Figure 2-1 (Hashash et al. 2010). Wang (1993) calculated racking ratios based on dynamic finite element analyses, which led to the development of a recommended design chart (Figure 2-2). Once the racking ratio has been found using the design chart, the box structure is analyzed with the racking displacement.

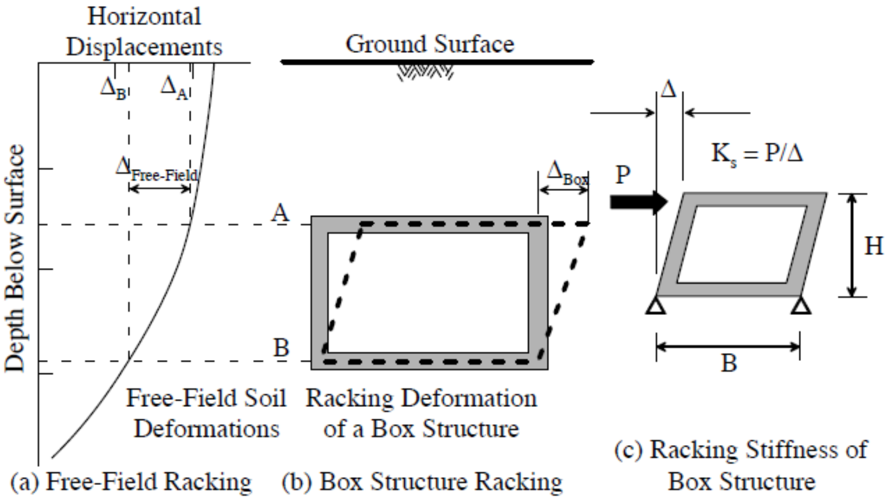

Figure 2-1. How to obtain: (a) free-field racking; (b) racking of a permanent box structure; and (c) racking stiffness of a box structure (Hashash et al. 2010).

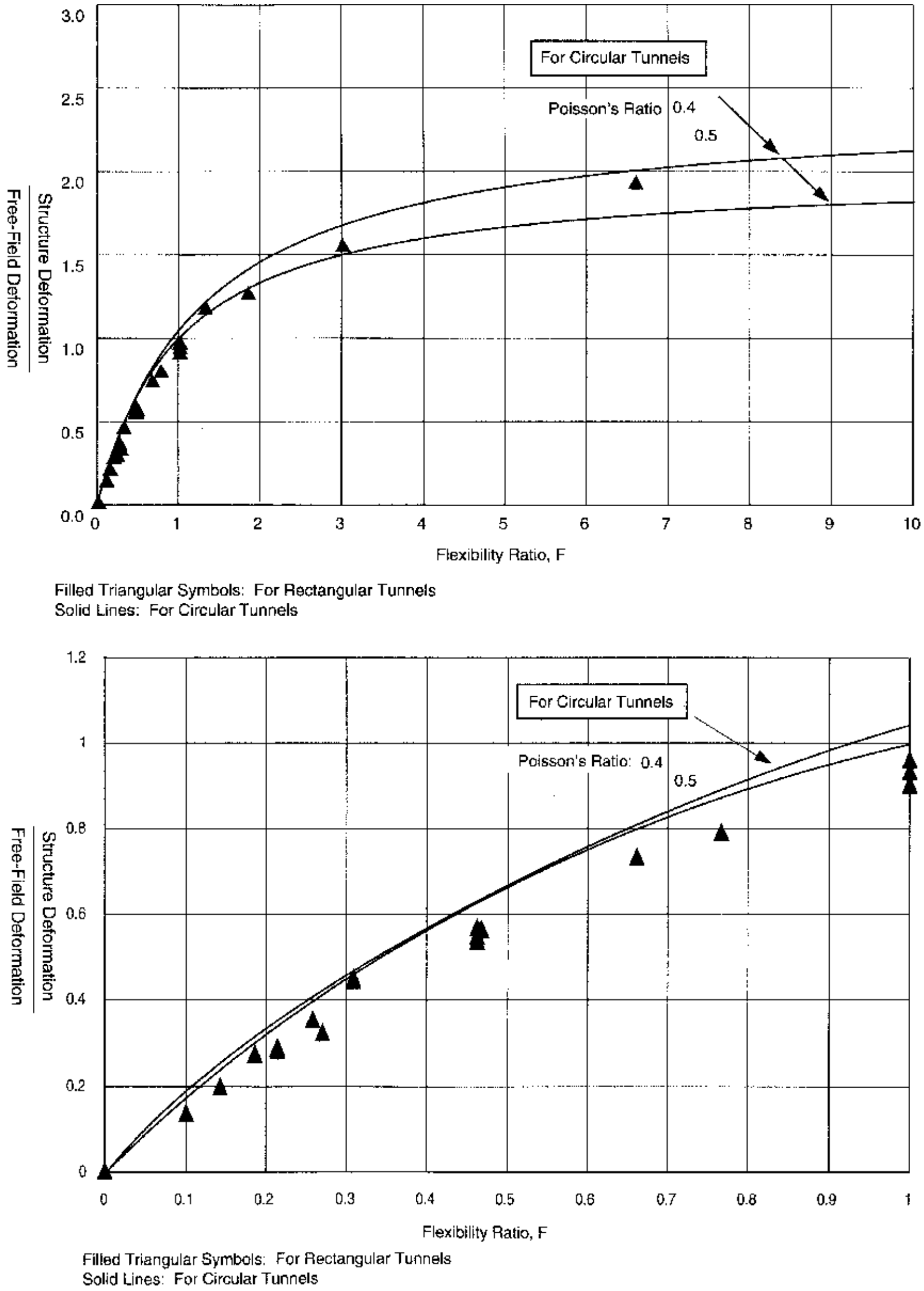

Figure 2-2. Racking versus flexibility ratios (R versus F) obtained from dynamic finite element SSI analyses performed on rectangular and circular tunnels (Wang 1993).

2.2 Seismic Design of Temporary Underground Structures

Either pseudo-static or more complex dynamic SSI numerical analysis methods are used in the design of a temporary braced excavation to evaluate racking displacements, in a similar manner as those used for permanent box structures. However, a more complex dynamic SSI analysis is preferred in this case due to a lack of soil cover. A dynamic, transverse SSI analysis can consider the properties of each soil sub-layer and its coupled interaction with a buried structure. Structural racking as well as other key design parameters, such as the induced lateral earth pressures (static and dynamic) can be estimated from this numerical analysis. Figure 2-3 shows the racking response of a temporary braced excavation. A large gap in knowledge exists in this area because the seismic response of temporary braced excavations has not been evaluated experimentally in the past in order to validate the described available simplified procedures and advanced numerical tools for this class of structure.

In addition to racking deformations, seismic lateral earth pressures experienced by the underground structure are another critical design parameter. Many researchers have evaluated seismic lateral earth pressures on retaining systems, analytically, numerically, or experimentally. Most of the previous studies, however, have focused on yielding walls, which move enough to develop active conditions. They have not considered flexible retaining structures that are restrained against excessive movement by their internal bracing. Hence, the results and observations obtained from prior studies may not be applicable to this class of underground structure.

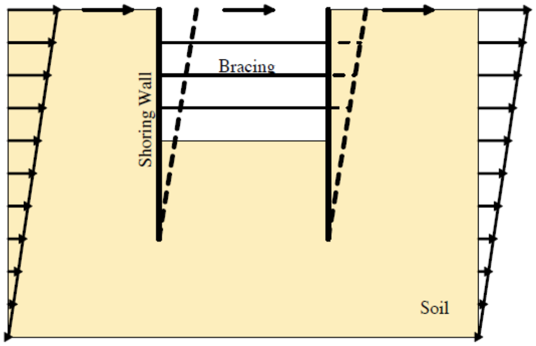

Figure 2-3.Schematic of racking deformations of a temporary braced excavation (Hashash et al. 2010)

3 - CENTRIFUGE TESTING PLAN

Three centrifuge tests were performed to study the seismic response of a braced excavation near tall buildings. The first of the three tests, E-No Bldg, was the baseline test, evaluating the braced excavation in isolation. The second test, E-Midrise, modeled the same excavation with an adjacent midrise building. The final test, E-Highrise, modeled a highrise building next to the braced excavation. Figure 3-1 shows a schematic drawing of the centrifuge testing plan in this study.

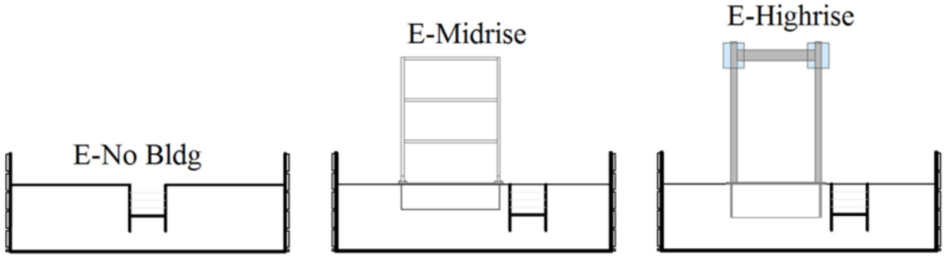

Figure 3-1. Centrifuge testing plan to study the seismic response of a braced excavation in isolation and near a midrise and highrise building.

3.1 Soil Properties

Because the measurements taken during the three tests were to be directly compared to one another, it was important to obtain the same soil properties in each test. A uniform layer of dry, Nevada sand was used in each model ($e_{min} = 0.531, e_{max} = 0.901$, and $G_s = 2.66$). The sand was dry pluviated into the centrifuge container to achieve a target relative density of 55%, correlating to a void ratio of 0.698 and a unit weight of 15.4 kN/m3. More details on the measurement of soil properties in centrifuge are provided in Section 4.1.

3.2 Base Motion Properties

The same six base motions were applied to the model during each experiment. These motions were selected by the research team to represent a range of characteristics in terms of amplitude, frequency, and duration to observe their effects on the excavation and on the interaction between the building and excavation. Table 3-1 summarizes the properties of the achieved base motions as recorded in E-No Bldg, and Figure 3-2 shows their 5%-damped spectral accelerations.

Table 3-1. Properties of the achieved base motions in E-No Bldg.

Event	Station	PGA* (g)	PGV (cm/s)	PGD (cm)	I_a (m/s)	D_{5-95} (s)
Northridge 1994	Newhall - WPC	0.47	48.1	12.7	1	5.6
Loma Prieta 1989	Santa Cruz - L. Obs.	0.1	7.5	0.6	0.1	10.9
Landers 1992	Joshua Tree	0.27	24.2	4.8	2.1	26.1
Chi Chi 1999	TCU078	0.37	31.3	4.7	2.9	25
Landers 1992	Lucerne	0.38	29.2	6.7	0.9	9.4
Kobe 1995	Takatori	0.5	55	17.5	3.7	10.1

*PGA/PGV/PGD = Peak Ground Accel./Vel./Disp; I_a = Arias Intensity; D_{5-95} = Significant Duration

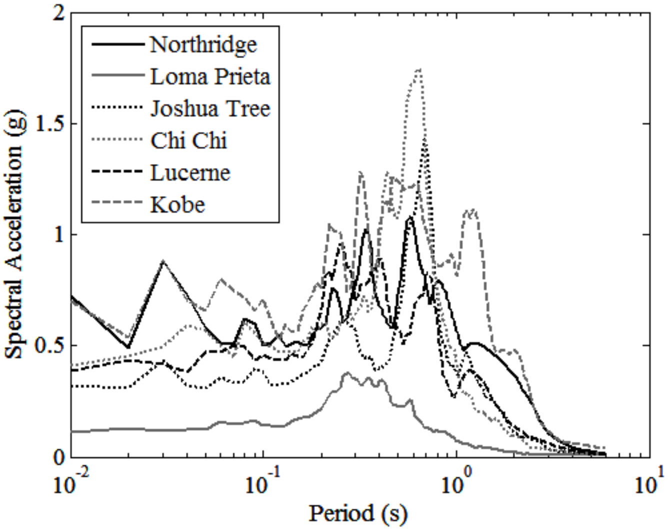

Figure 3-2. Spectral acceleration with 5% damping of the six achieved base motions in E-No Bldg.

3.3 Properties of the Temporary Excavation

The temporary, braced excavation used in the centrifuge tests was initially designed in accordance with FHWA-IF-99-015. Even though the design of the braced excavation is outside the scope of this thesis, finite element analyses in Plaxis were performed by the research team to check the stability of the excavation under static and dynamic loading with and without the adjacent structure. The target temporary excavation was designed based on the properties of steel soldier piles and steel tube struts. The model excavation used in the centrifuge tests was constructed with aluminum steel plates and aluminum tube struts, with equivalent racking stiffness, K_s, as the target braced excavation. Table 3-2 summarizes the properties of the designed prototype brace excavation and the simplified centrifuge model excavation.

The braced excavation used in the centrifuge tests measured 12 m deep by 14 m wide, in prototype scale. The excavation walls extended another 6m below the depth of the excavation. Struts were placed at 3, 6, and 9 m depths, horizontally spaced by 4.2 m. In order to reduce frictional effects from the centrifuge container, the length of the excavation was designed to be 5 mm shorter than the actual width of the container to allow room for Teflon sheets to be placed at the excavation-container interface. The model struts utilized all thread, acorn nuts, and standard nuts on the ends, so the strut could be lengthened slightly when positioned in-between the aluminum plates during model construction.

Table 3-2. Properties of the designed target temporary excavation compared to the simplified centrifuge model excavation (prototype scale).

	Design Properties	Centrifuge Model Properties
Height (m)	18 (6 embedded)	18 (6 embedded)
Width (m)	14	14
Material Type	Steel	6061 Al.
Wall Beams	W27x178 (horiz. spacing: 1.5 m)	0.41m thick plate
Struts	HSS14x0.625 (spacing: 2m horiz.; 2-3-3m vert. from top)	OD-0.41m, ID-0.39m (spacing: 4.2m horiz.; 3-3-3m vert. from top)
Density (kg/m^3)	7800	2700
Young's Mod. (kPa)	2.50E+07	6.89E+07
Poisson's Ratio	0.28	0.33
Racking Stiffness (MN/m/m)	2.0 (Anal. Solution)	1.5 (FEM)

3.4 Properties of the Midrise Building

The midrise building model was designed to represent the dimensions and dynamic properties (e.g., modal frequencies, base shear, and moment) of a typical steel-frame, 13-story structure in Los Angeles, CA. The target structure was simplified as a 3-DOF system for the centrifuge tests to capture its three primary vibration modes. Table 3-3 summarizes the properties of the midrise building as designed and simplified for centrifuge modeling.

3.5 Properties of the Highrise Building

A highrise building had not been tested before by other researchers in centrifuge, introducing new challenges in design and installation as well as safety. The tall structure was designed as a simplified single-DOF system to have realistic dimensions and key dynamic properties, while taking into consideration the space and overhead limitations of the centrifuge. The target building had footprint dimensions of 69 m x 69 m. This size was reduced to 39 m by 39 m because of the limited size of the centrifuge container. Overhead space in the centrifuge did not allow a proper simulation of the building’s center of gravity, and therefore its seismic moments were not captured by the model building. The seismic weight and fundamental period of the building, however, were simulated, which were expected to strongly influence SSUSI effects. Table 3-3 summarizes the properties of the highrise building as designed and simplified for centrifuge modeling.

Table 3-3. Properties of midrise and highrise buildings as designed and simplified for centrifuge.

	Design Properties Target Range	Centrifuge Model Properties		Design Properties Target Range	Centrifuge Model Properties	
		Prototype Dimensions	Model Dimensions N=65		Prototype Dimensions	Model Dimensions N=65
Number of Stories	13 to 15	13 simulated with 3 masses	3 mass system	42	42 simulated with 1 mass	1 mass system
Subterranean Levels	1 to 2	1	1	4	4	4
Seismic Structural System	RCMF or SMRF (1)	SMRF	SMRF	Concrete core with SMRF	SMRF	SMRF
Height Above Ground (m)	50 to 70	48.75 (2)	0.75 (2)	142	48.75 (2)	0.75 (2)
Depth below Ground (m)	4.5 to 6.5	4.25	0.065	13	13	0.2
Footprint Dim. (m x m)	23x59 / 53x53 / 38.5x22.5	38.5 x 22.5 (2)	0.592 x 0.346 (2)	Bldg: 69 x 69; Core: 33 x 33	33 x 33	0.508 x 0.508
Seismic Weight Density (kN/m^2/story)	RCMF: 7.13; SMRF: 3.5 to 3.81	3.5	-	Bldg. footprint: 2.27; Core footprint: 9.92	9.92	-
Weight of Superstructure (kN)	42,860 to 125,743	39,414	0.192	453,719	453,719	1.77
Fundamental Periods (sec)	RC: 2.6-2.7; SMRF: 3.03/1.08/0.65; 1.69/0.56/0.32	3.02/0.85/0.43 (3)	3.35/0.84/0.43 (5)	4.28 to 4.93	4.03	-
Base Shear (kN)	V_y/W = 0.088 to 0.094	Demand: 3,510; Yield: 3,510 (3)	-	Demand: 47,738	Yield: 57,858(4)	-
Max. Drift Ratio (m)	0.44 to 0.52	0.15 (3)		N.A.	N.A.	N.A.
Overturning Moment (kN-m)	Yield: 188,584 to 827,389	Demand: 167,602; Yield: 167,602	-	Demand: 1,057,538	Yielding: 2,820,580(4)	-
Column and Beam Model Sections	N.A.	N.A.	HSS 5/8" x 5/8" x 1/16"	N.A.	N.A.	HSS 3/2 x 3/2 x 1/8"
Basement Wall Sections (m)	N.A.	H= 10m, Th.= 0.2m	H= 154mm Th.= 3.2mm	N.A.	H= 200mm Th.= 9.5mm	H = 13m Th.= 0.6m

NOTE: (1) RCMF: Reinforced Concrete Moment Frame, SMRF: Steel Moment Resisting Frame;
(2) Due to centrifuge size limitations;
(3) Estimated using a 2D OpenSees model to meet seismic demand and allowable drift requirements from ASCE7-10 for the building properties selected;
(4) Estimated using a 2D OpenSees model to the demands estimated for the prototype building;
(5) Found experimentally using a hammer impact test;
(6) Not provided in the literature found.

3.6 Instrumentation Layout

Displacements of the braced excavation and the far-field soil during shaking events in addition to seismic lateral earth pressures were critical parameters to reliably measure in the centrifuge tests. Other important parameters were the bending moments along the excavation walls, axial forces in the struts, and settlements across the model. Four primary types of sensors were installed in the centrifuge models: accelerometers, linear potentiometers (LPs), strain gauges, and tactile pressure sensors. Cameras were also used to capture the movements of the system, but because of their low frame rate, no measurements were made from camera recordings. Figures 3-3 through 3-5 show an elevation view of the instruments used in E-No Bldg. Figures 3-6 through 3-8 show the instruments in E-Midrise, and Figures 3-9 through 3-11 show E-Highrise. The models were densely instrumented, and therefore multiple drawings are presented for each test to clearly document the locations and names of each instrument, which will be referenced in the following sections.

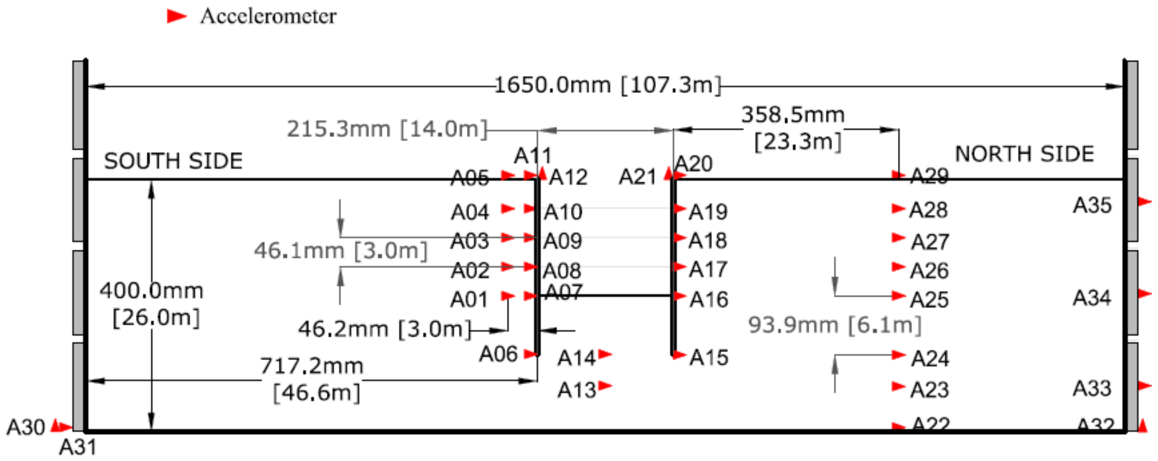

Figure 3-3. Elevation view of the partial instrumentation plan, showing wired accelerometers in E-No Bldg. Dimensions are shown in model and [prototype scales].

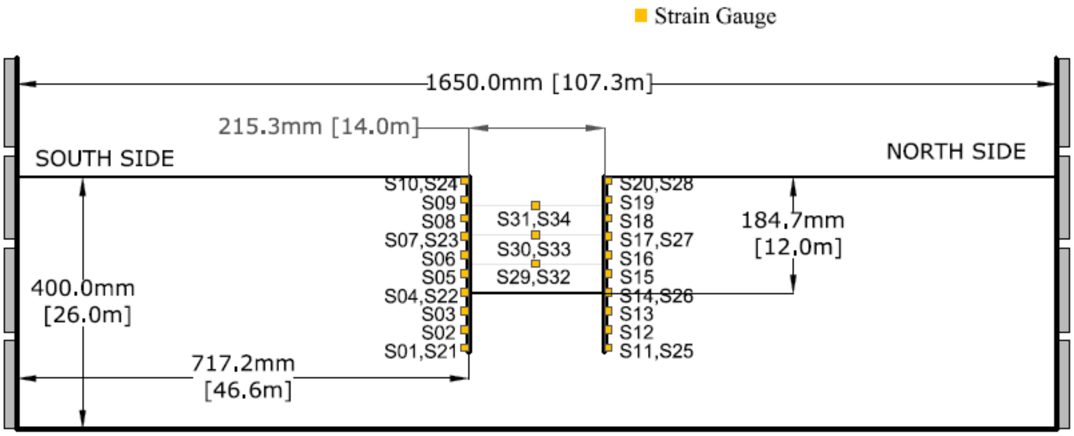

Figure 3-4. Elevation view of the partial instrumentation plan, showing strain gauges in E-No Bldg. Dimensions are shown in model and [prototype scales].

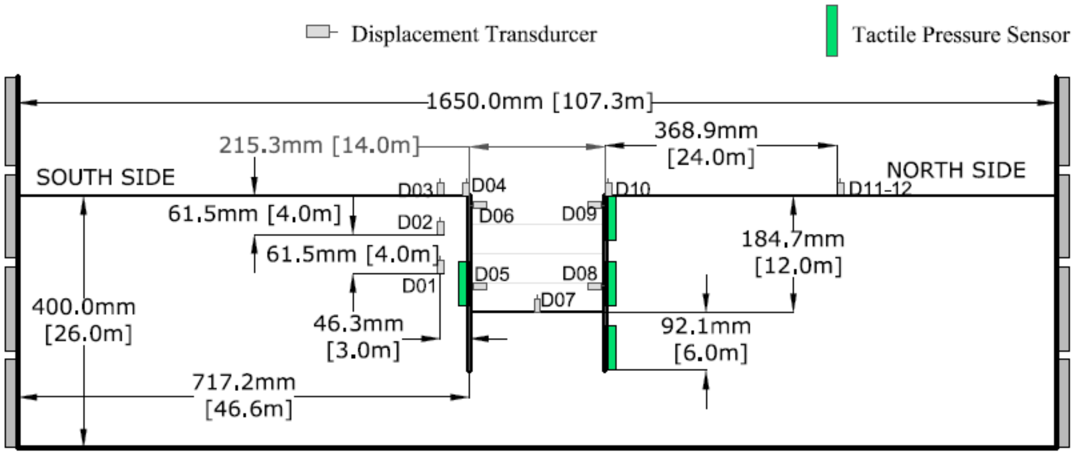

Figure 3-5. Elevation view of the partial instrumentation plan, showing tactile pressure sensors and linear potentiometers in E-No Bldg. Dimensions are shown in model and [prototype scales].

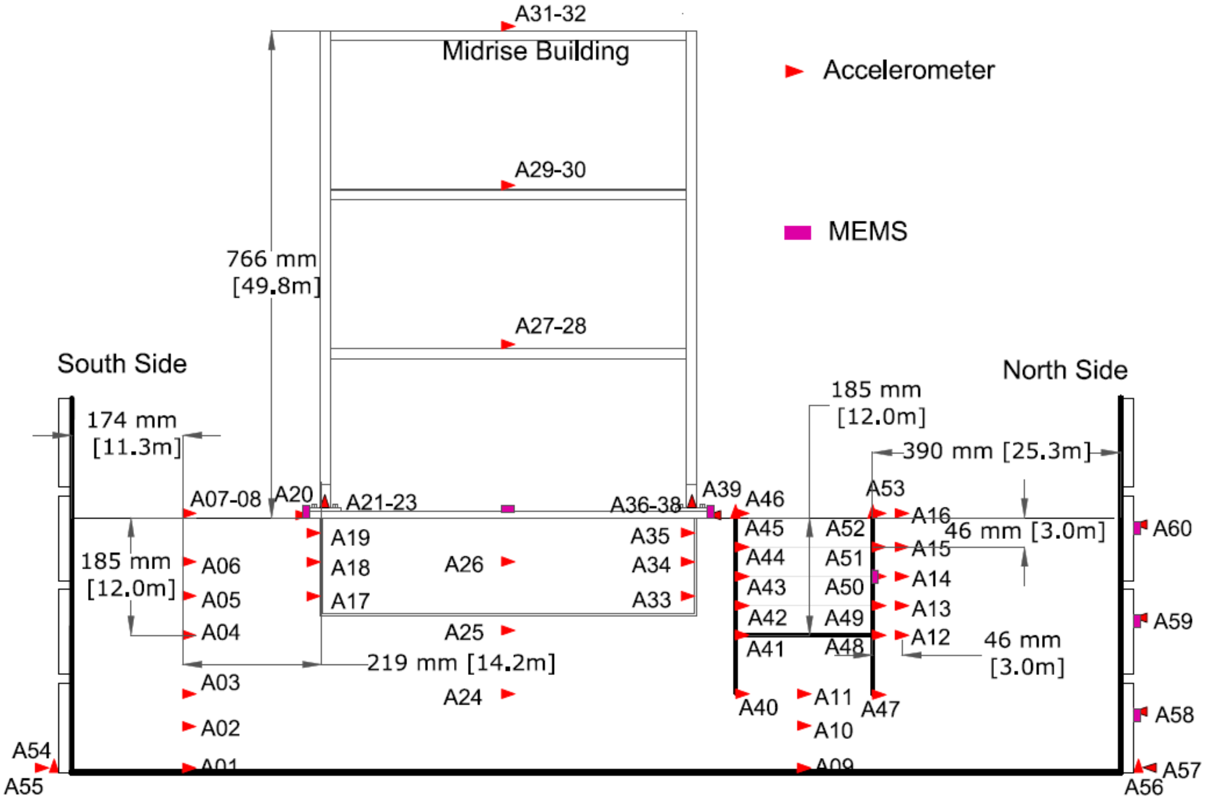

Figure 3-6. Elevation view of the partial instrumentation plan, showing wired accelerometers and wireless MEMS accelerometers in E-Midrise. Dimensions are shown in model and [prototype scales].

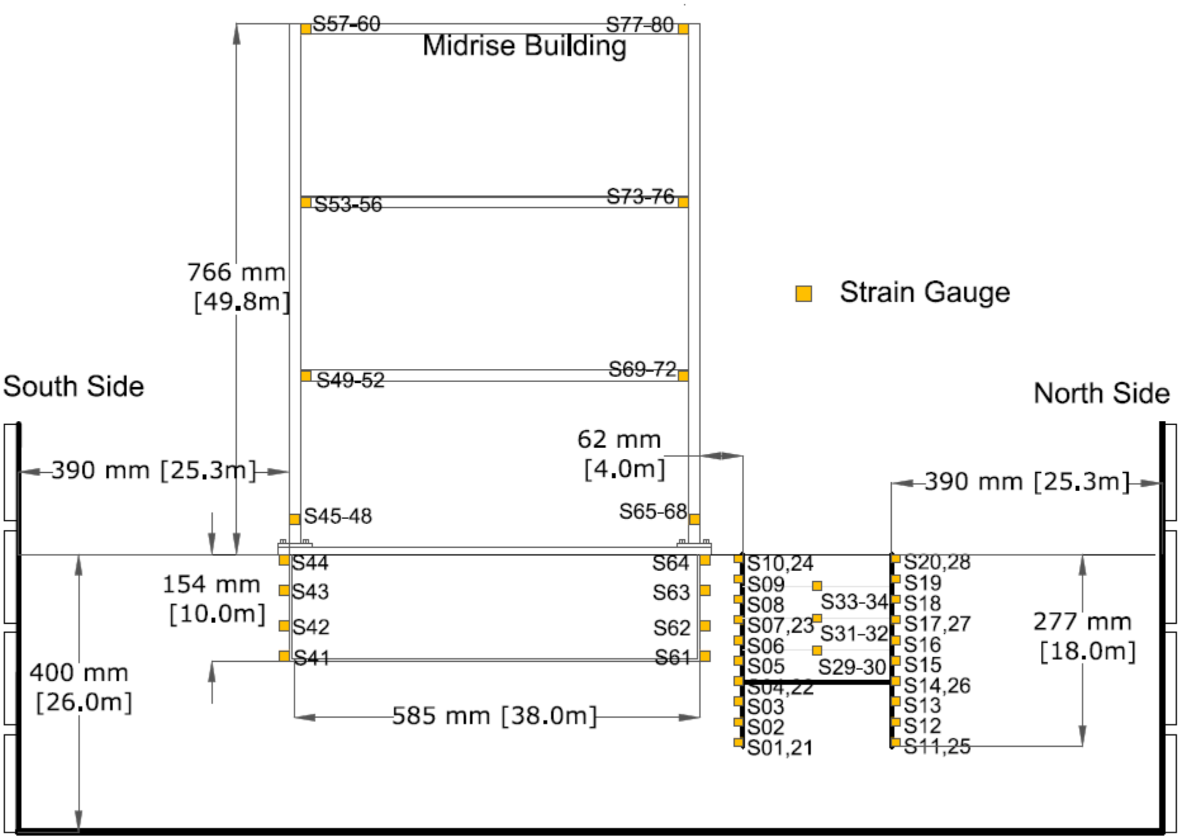

Figure 3-7. Elevation view of the partial instrumentation plan, showing strain gauges in E-Midrise. Dimensions are shown in model and [prototype scales].

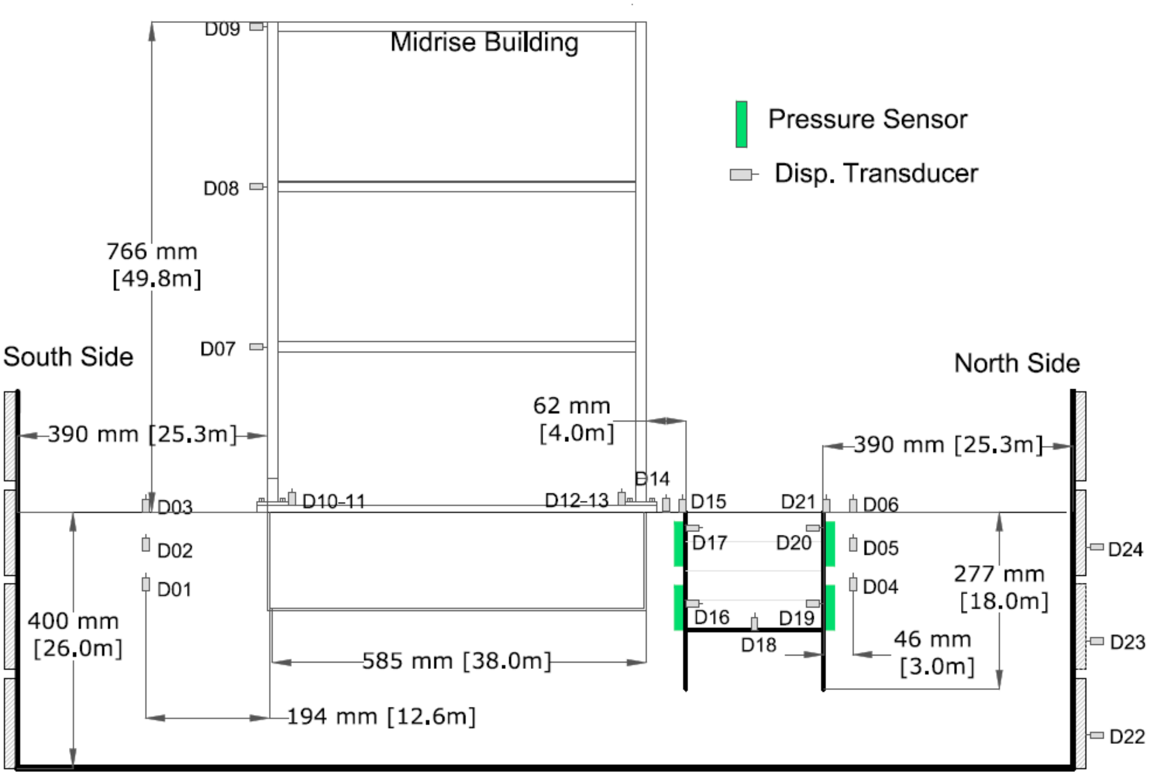

Figure 3-8. Elevation view of the partial instrumentation plan, showing tactile pressure sensors and linear potentiometers in E-Midrise. Dimensions are shown in model and [prototype scales].

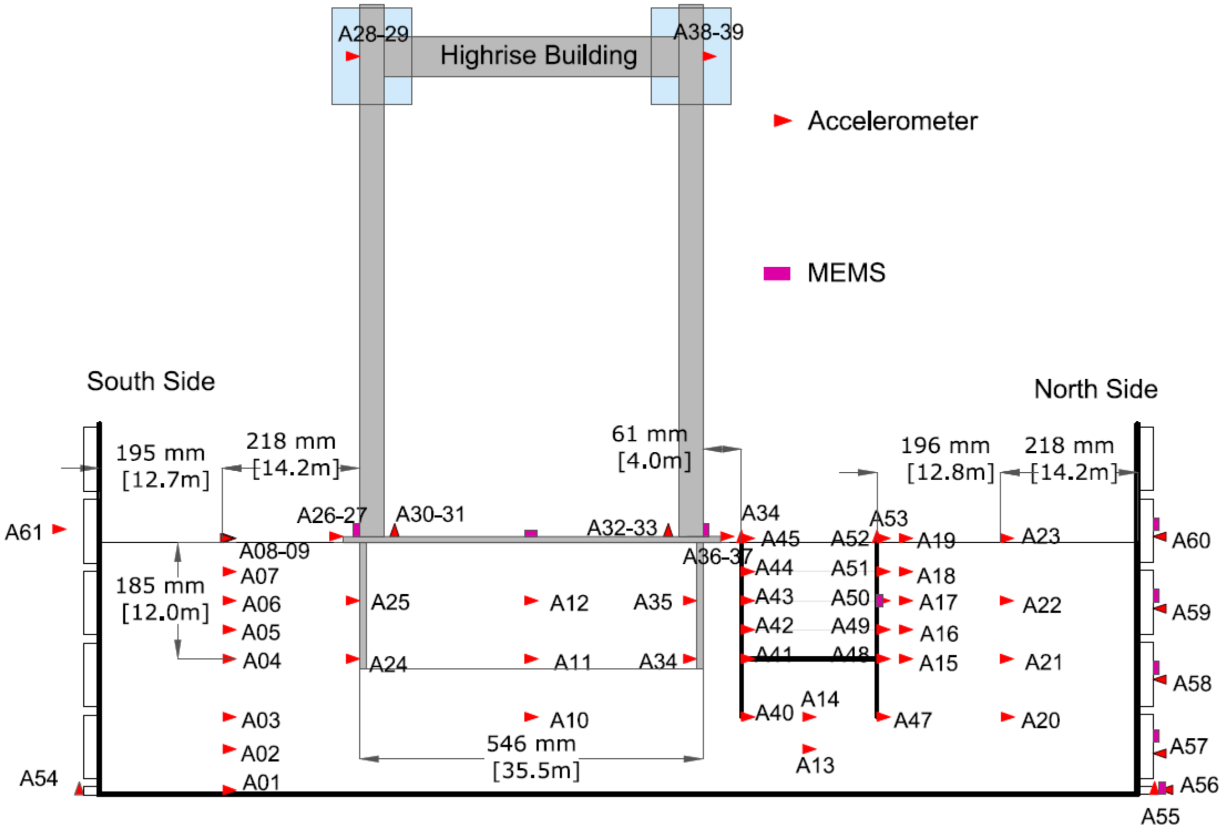

Figure 3-9. Elevation view of the partial instrumentation plan, showing accelerometers and mems accelerometers in E-Highrise. Dimensions are shown in model and [prototype scales].

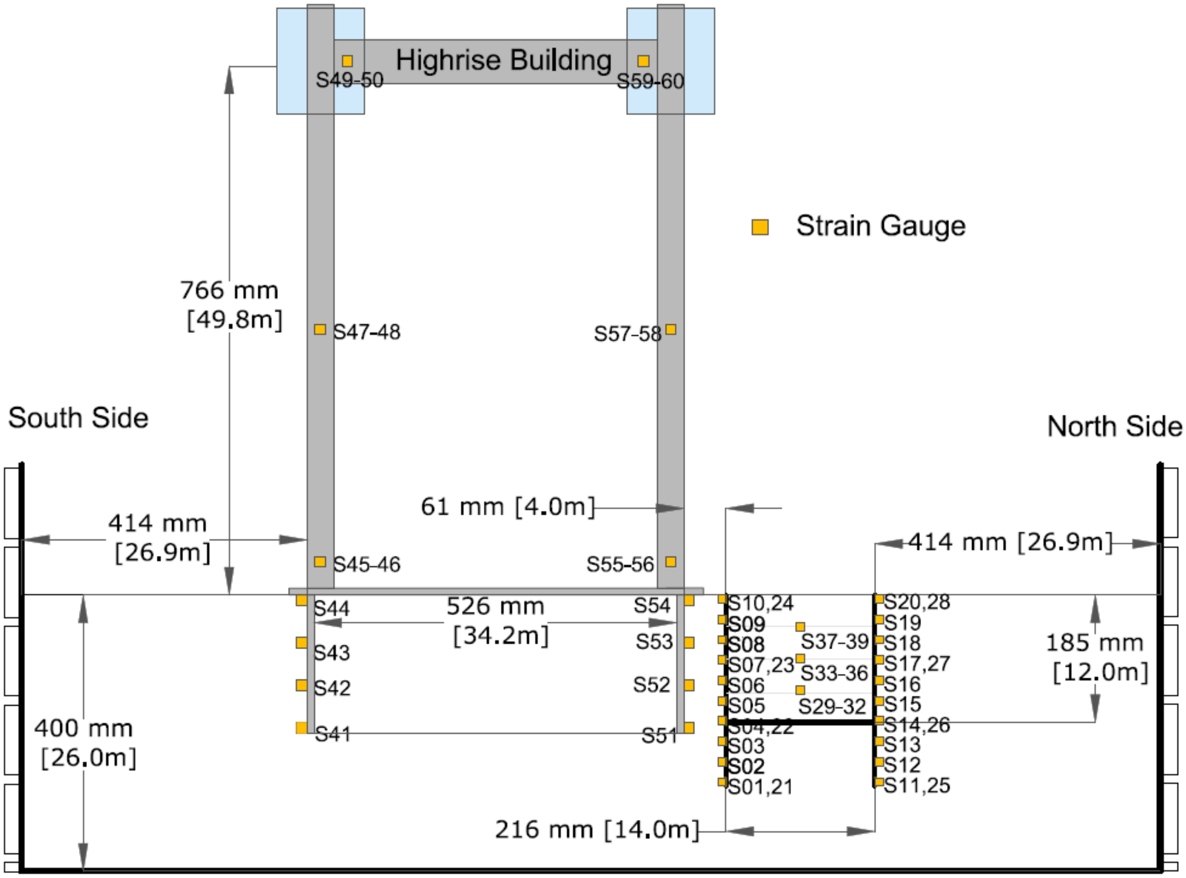

Figure 3-10. Elevation view of the partial instrumentation plan, showing strain gauges in E-Highrise. Dimensions are shown in model and [prototype scales].

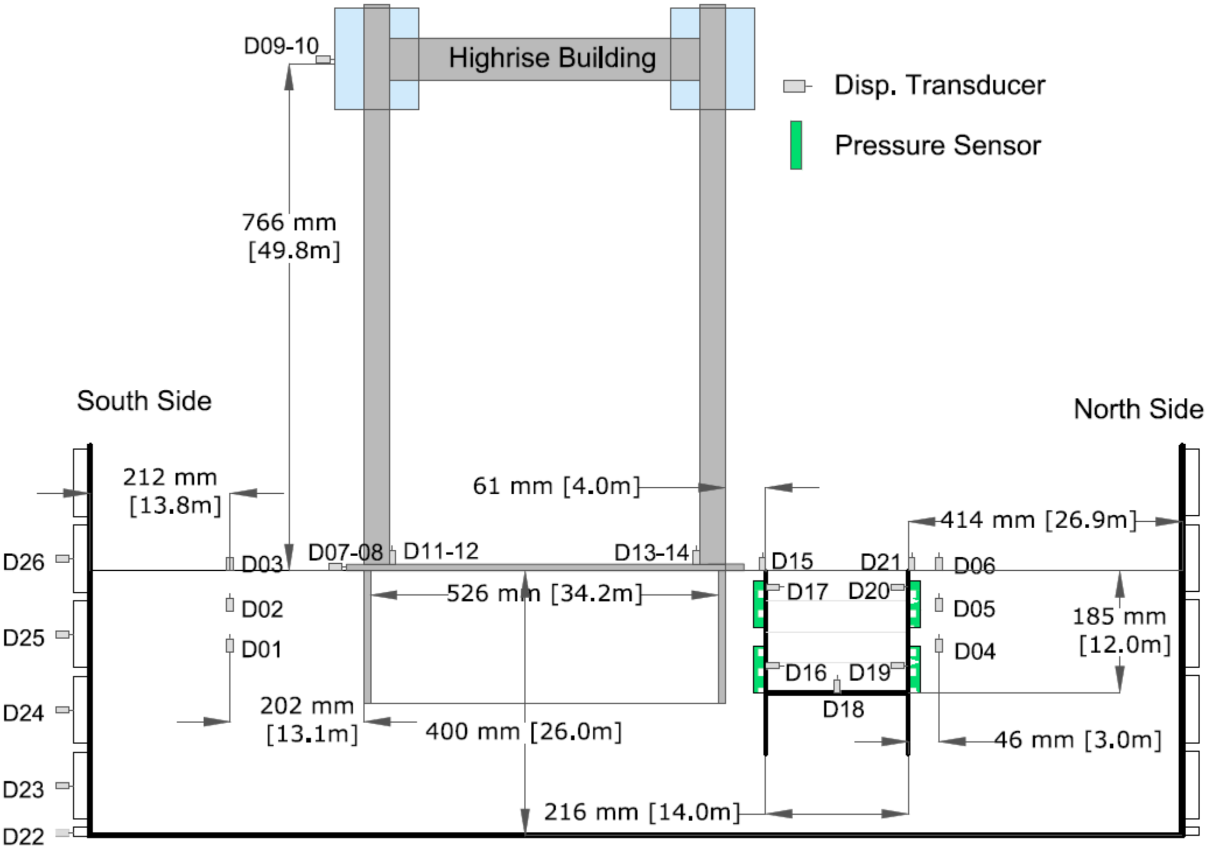

Figure 3-11. Elevation view of the partial instrumentation plan, showing tactile pressure sensors and LPs in E-Highrise. Dimensions are shown in model and [prototype scales].

4 - EXPERIMENTAL RESULTS

4.1 Measuring Soil Properties

Dry, uniform, medium-dense Nevada Sand was selected to provide a simplified soil stratum on which fundamental soil-structure-underground structure-interaction (SSUSI) could be observed. The sand was dry pluviated into the centrifuge container to achieve a relative density of 55% +/- 5%. At the elevations corresponding to instrumentation or structures, pluviation was stopped and a vacuum was used to level the soil surface.

In order to compare the observations made from one centrifuge test to another, the soil properties needed to be kept consistent from test to test. To ensure its consistency, the pluviator was calibrated before the construction of each model in order to achieve the desired relative density. After model construction, methods were also used during each centrifuge test to measure the far-field soil properties. The far-field soil response in each test was defined as half-way between a structure and the centrifuge container to be as far away as possible from these boundaries. Four methods were used in-flight to measure the far-field soil properties: 1) a miniature cone penetration test, 2) bender elements, 3) application of a small amplitude, high frequency sinusoidal motion, and 4) acceleration recordings of centrifuge vibrations.

4.1.1 Miniature Cone Penetration Test

A miniature cone available at UCD-CGM and shown in Figure 4-1a was used to measure the tip resistance and side friction with depth when pushed into the far-field soil prior to the first shake in each test. The cone measured 30.5 cm long with a cone diameter of 6 mm in model scale. The cone had a tip angle of 60 degrees, similar to a full-size CPT.

The cone was mounted on the centrifuge above the model where it was to be pushed on the north side of the container as shown in Figure 1-4c and Figure 4-2. Once the model reached and stabilized at its final g-level of 65g, the cone was pushed into the soil below. The total resistance, tip resistance, and displacement of the cone were measured in voltage by the data acquisition system (DAQ). The CPT was calibrated to convert the raw voltage to proper engineering units. During the calibration of the CPT, a known load was applied to the butt of the cone with a reference load cell, Figure 4-1b, and sensitivity values were calculated for the tip and butt load cells of the miniature CPT. The load measured by the butt of the cone during calibration was equal to the load measured by the tip because no load was carried along the sides of the cone from friction.

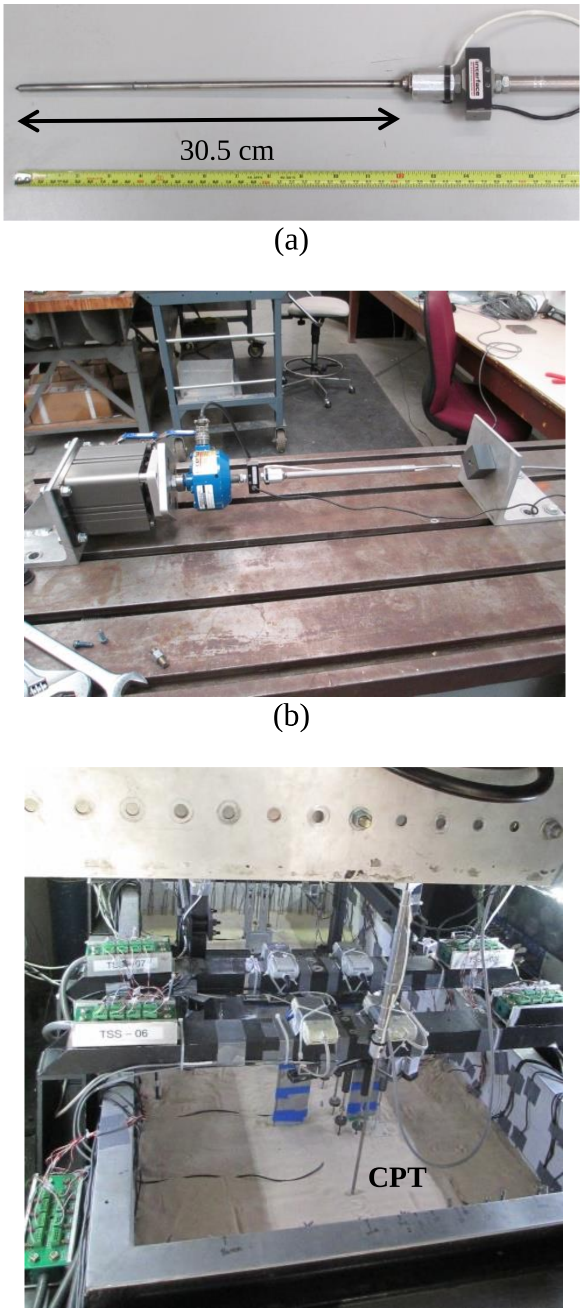

(a)

(b)

(c)

Figure 4-1. Miniature cone penetration test (CPT) to measure soil properties within the centrifuge model before shaking: (a) the model scale dimensions of the cone, (b) the calibration process for the CPT, and (c) the CPT mounted on the centrifuge above where it will electronically be pushed.

When the cone was pushed into the soil, the load cell on the butt of the cone measured the total resistance from the tip and side friction. The side friction, f_s, was therefore calculated by subtracting the load carried by the cone tip from the total load needed to push the cone. Since the load carried by the cone tip was directly measured, the cone-tip resistance, q_c, was calculated by dividing this load by the surface area of the cone.

The profiles of cone-tip resistance and side friction were used to calculate an equivalent shear wave velocity profile through empirical relations. Two relations proposed by Baldi et al. (1989) and Piratheepan (2002) were applicable to young sand deposits and were used to convert the CPT data to shear wave velocity profiles for the centrifuge tests.

$$V_s\ (Baldi\ et\ al.\ 1989) = 17.48 * q_c^{0.13} * \sigma_v'^{0.27} \quad \text{(Eq. 4-1)}$$

$$V_s\ (Piratheepan\ 2002) = 25.3 * q_c^{0.163} * f_s^{0.029} * D^{0.155} \quad \text{(Eq. 4-2)}$$

q_c, f_s, σ_v' are in kPa and depth (*D*) is in meters. To estimate the vertical effective stress, the dry unit weight of Nevada Sand corresponding to 55% relative density was used.

The shear wave velocity profile from Baldi et al. (1989) provided an upper bound profile, while the relation proposed by Piratheepan (2002) provided the lower bound shear wave velocity profile from the miniature CPT. These profiles are compared with other measurement methods later in this section.

4.1.2 Bender Elements

Six bender element pairs were installed at two depths during the model construction of E-Highrise: 8 m and 21.3 m below the ground surface, as shown in Figure 4-2. The pair consisted of a sender and a reciever spaced 150 mm apart. Before the first applied shake and between subsequent earthquake events, each pair of bender elements was triggered separately. The time of wave arrival was estimated graphically as a range and a shear wave velocity range was measured at that depth by dividing the distance traveled between pairs, 150 mm, by the time it took for the wave to travel this distance.

The bender element pairs 0 and 1 were placed in the far-field soil on the south side of the container. The bender element pairs 4 and 5 were placed in the far-field on the north side of the container. The results of these two far-field representations were comparable. The installation of far-field bender elements is shown in Figure 4-3 at a depth of 8 m below the soil surface.

Figure 4-4 shows the results of the bender element pairs in the far-field on the south side of the container. By comparing the measured shear wave velocity values in the far-field (south side) after each motion, soil densification was observed initially, which eventually plateaued.

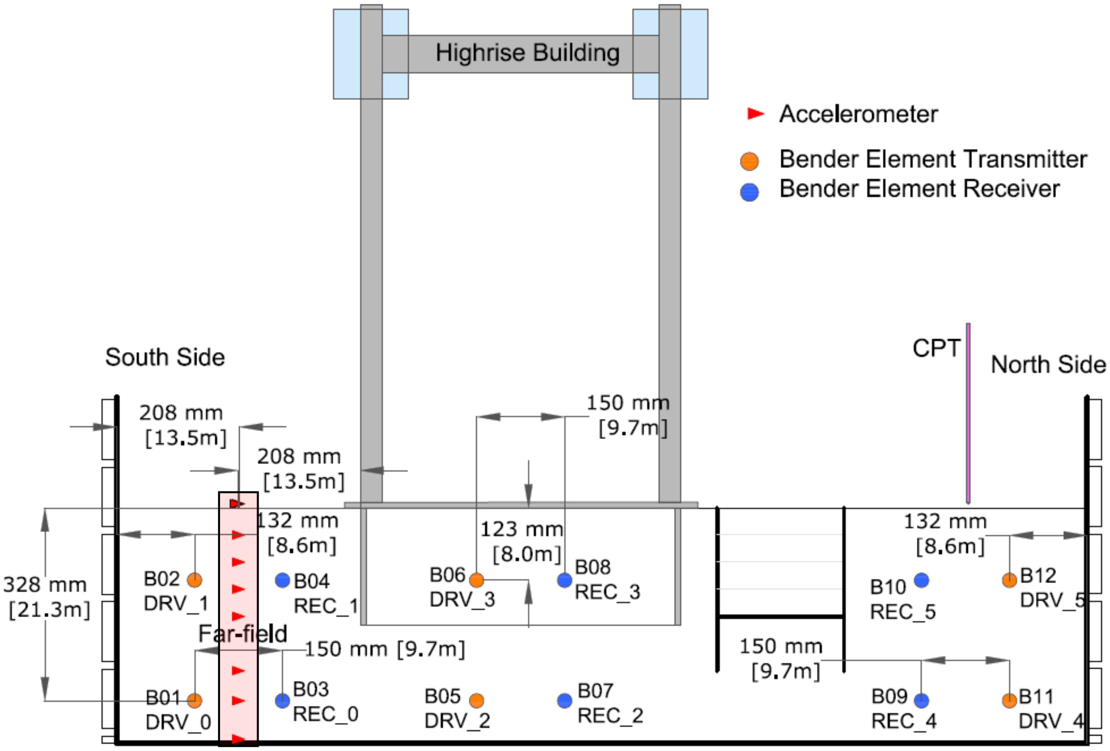

Figure 4-2. Drawing of the location of instrumentation used for measuring soil properties in E-Highrise: bender elements, the CPT, and the far-field array of accelerometers. Dimensions shown in model [and prototype scale] at 65g of centrifugal acceleration.

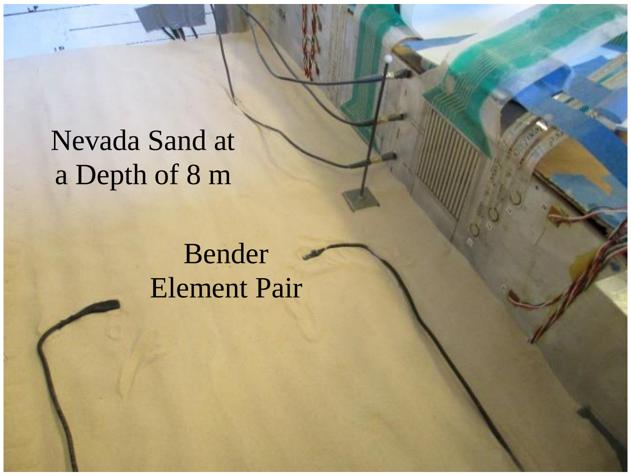

Figure 4-3. A pair of far-field bender elements installed outside of the braced excavation at a depth of 8 meters, prototype scale, during model construction of E-Highrise.

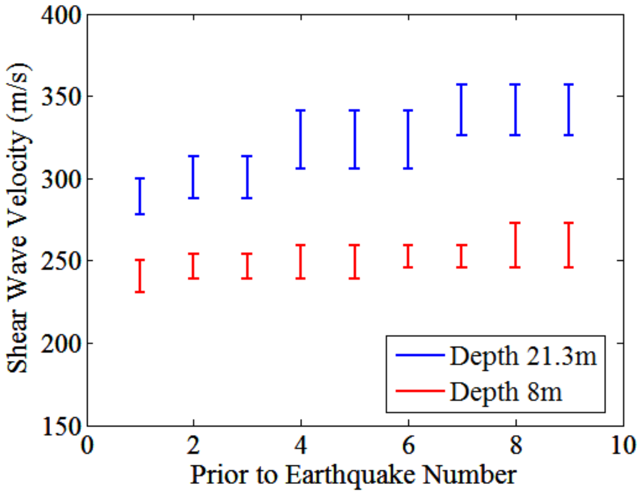

Figure 4-4. Results of two bender element pairs in the far-field of E-Highrise showing a range of shear wave velocities prior to different earthquake motions.

4.1.3 Ambient Vibration and Small Amplitude Sinusoidal Base Motion

The centrifuge created small vibrations, which contained content at a range of frequencies at small strains. Far-field accelerometer arrays, as highlighted in Figure 4-2, in each centrifuge test recorded data under these ambient vibrations. The frequency-dependent transfer function (TF) of accelerations recorded at the soil surface to container base was used to obtain the average fundamental frequency of the free-field soil column at small strains, f_{so}, which was then converted to an average $\overline{V_s}$ value (e.g., $\overline{V_s} = 4H.f_{so}$, where H is the total thickness of the soil column).

A small-amplitude, high frequency (PGA = 0.05 g; f = 500 Hz) sinusoidal motion was applied to the base at the beginning of E-Highrise, exciting the model specimen at small-strain levels. An array of far-field accelerometers recorded wave propagation through the soil during this motion similar to the data recorded during the ambient vibrations. The average wave arrival time and travel distance from base to soil surface was also used to independently obtain the $\overline{V_s}$. Together, the frequency-domain TF and time-domain arrival time approaches provided a range of $\overline{V_s}$ values from the high frequency sinusoidal base motion.

Figure 4-5 shows the TF of surface to base accelerations obtained from ambient recordings in E-No Bldg, E-Midrise, and E-Highrise and the small-amplitude sine wave in E-Highrise. The values of the average shear wave velocities, $\overline{V_s}$, corresponding to the peak TF are also shown on the figure in the corresponding color. These methods only provide an average value of shear wave velocity, $\overline{V_s}$, for the soil column as opposed to a V_s profile with depth provided by the cone or bender elements.

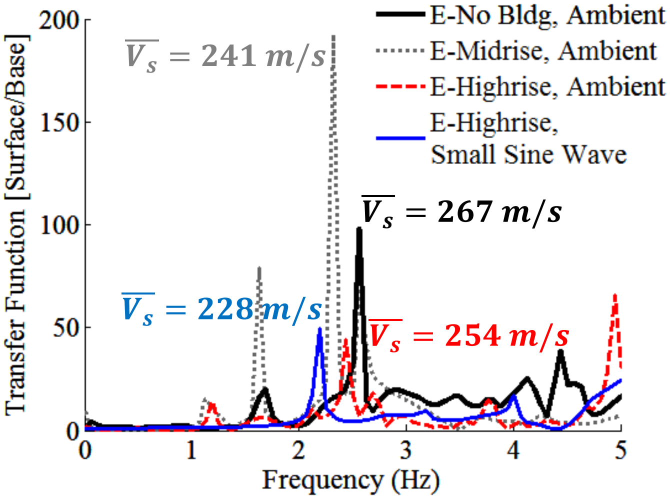

Figure 4-5. Frequency-dependent transfer function of the far-field soil column in the three excavation centrifuge tests to find the average shear wave velocity of the soil column, $\overline{V_s}$, from ambient vibrations and a small amplitude sinusoidal base motion.

4.1.4 Empirical Profiles of Shear Wave Velocity

These four methods of direct and indirect V_s measurements in the far-field were compared with empirically obtained shear wave velocity profiles (e.g., Seed and Idriss 1970; Bardet 1993; Jamiolkowski et al. 1991; Menq 2003; Hardin and Drnevich 1972) based on the properties of Nevada Sand at a relative density of 55%. These five empirical equations are given in Eq. 4-3 through 4-7.

Seed and Idriss (1970) proposed an empirical relationship for shear wave velocity with depth as the following expression:

$$V_s(Seed\ and\ Idriss\ 1970) = \sqrt{\frac{1000K_{2,max}(\sigma_m')^{0.5}}{\rho}} \qquad \text{(Eq. 4-3)}$$

where $K_{2,max}$ varies with the relative density of the soil and was taken as 45 for the Nevada Sand, corresponding to a D_r of 55%.

Bardet (1993) proposed an expression for shear wave velocity with depth given in the following equation:

$$V_s(Bardet\ 1993) = \sqrt{\frac{8811\frac{(1.935-e)^2}{1+e}(\sigma'_m)^{0.5}}{\rho}} \qquad \text{(Eq. 4-4)}$$

In 2003, Menq developed an empirical equation for shear wave velocity that also incorporated grain size and the coefficient of uniformity, C_u, as variables in the relation.

$$V_s(Menq\ 2003) = \sqrt{\frac{67100(C_u)^{-0.2}(e^{-1-\left(\left(\frac{D_{50}}{20}\right)^{0.75}\right)})\left(\frac{\sigma'_m}{P_a}\right)^{0.48(C_u)^{0.09}}}{\rho}} \qquad \text{(Eq. 4-5)}$$

Laboratory tests done by Cooper Lab on the Nevada Sand used in the centrifuge tests gave a C_u of 2.07 and a D_{50} of 0.144 mm so these parameters were taken for use in Menq's relation.

The fourth empirical relation considered was from Jamiolkowski et al. 1991 and is given below in Eq. 4-6.

$$V_s(Jamiolkowski\ et\ al.\ 1991) = \sqrt{\frac{625\frac{1}{e^{1.3}}OCR^k P_a^{0.5}(\sigma'_m)^{0.5}}{\rho}} \qquad \text{(Eq. 4-6)}$$

The coefficient k was taken to be 0, corresponding to a plasticity index of 0 for the Nevada Sand.

Hardin and Drnevich provided an empirical relation for shear wave velocity for sands in 1972 that was also taken to represent the sand deposit in the centrifuge models.

$$V_s(Hardin\ and\ Drnevich\ 1972) = \sqrt{\frac{2630(2.17-e)^2(\sigma'_m)^{0.5}}{(1+e)\rho}} \qquad \text{(Eq. 4-7)}$$

In all the empirical relations outlined above, a density of 1.57 Mg/m^3 and a void ratio of 0.698 were used, corresponding to a relative density of 55%.

Figure 4-6 shows these empirical profiles with depth and an average of the five relations. Out of these empirical relations, Bardet (1993) provided a lower bound and Jamiolkowski et al. (1991) an upper bound estimation, which are shown in the following figure.

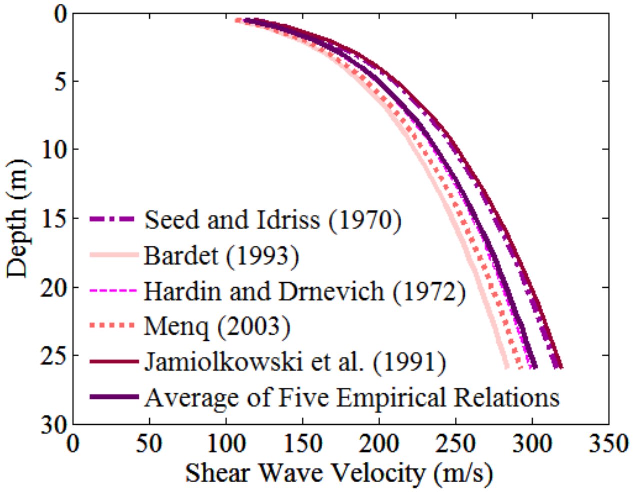

Figure 4-6. Five empirical relations for shear wave velocity of sand with depth.

4.1.5 Summary and Comparison

Figure 4-7 summarizes all of the methods outlined to measure soil properties in the far-field as compared to the lower and upper bounds of the empirical relations. Generally, lower values of V_s were obtained indirectly from CPT measurements compared to other methods in all centrifuge tests. This is likely due to the large-strain nature of cone penetration tests. Similarly, the low amplitude sine-wave method provided slightly lower estimates of $\overline{V_s}$ compared to ambient recordings and the empirical average shear wave velocity range. This is likely due the slightly larger induced shear strains by the sinusoidal base motion within the soil stratum. Ambient vibration and bender element results, which were judged most appropriate for obtaining small-strain soil properties, compared well with the average to upper bound empirical relations of V_s in the centrifuge tests (e.g., Seed and Idriss 1970, Jamiolkowski et al. 1991).

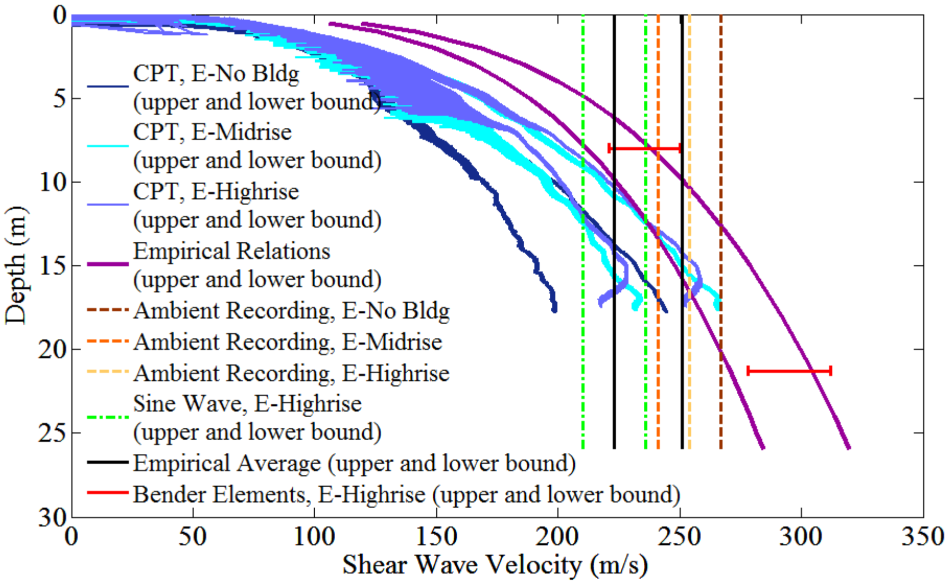

Figure 4-7. Comparison of all soil property measurement methods implemented during the three excavation centrifuge tests.

4.2 Displacements and Racking Deformations

Unlike aboveground structures, the seismic response of underground structures is dominated by the response of the surrounding soil. Due to the constraints the soil imposes, the deformations and inertial response of the structure is controlled by the response of the soil mass, as described in Chapter 3. Transverse displacements of the underground structure, known as racking displacements, are a critical measurement to evaluate seismic performance.

In this study, racking of the modeled braced excavation was defined as the relative displacement of the top of the excavation wall with respect to the bottom of the excavation (depth of 12m) as shown in Figure 4-8. Racking deformations of the braced excavation and surrounding soil over the height of the excavation were directly measured in the centrifuge tests with linear potentiometers (LPs) and were indirectly measured by double integrating accelerometer recordings. The horizontal LPs installed at the elevations to measure racking deformations were held in place with LP racks that were bolted to the centrifuge bucket or container. During ground motions, the LP racks experienced displacements themselves, which interfered with the displacement recording of the LP instrument. Therefore, since the walls were not expected to yield, the most reliable method of measuring displacements during the tests was from the double integration of accelerometer recordings. Racking of the braced excavation and of the far-field soil was measured using accelerometers placed at the soil surface and at a depth of 12 m below the surface, representing the elevation of the bottom of the excavation.

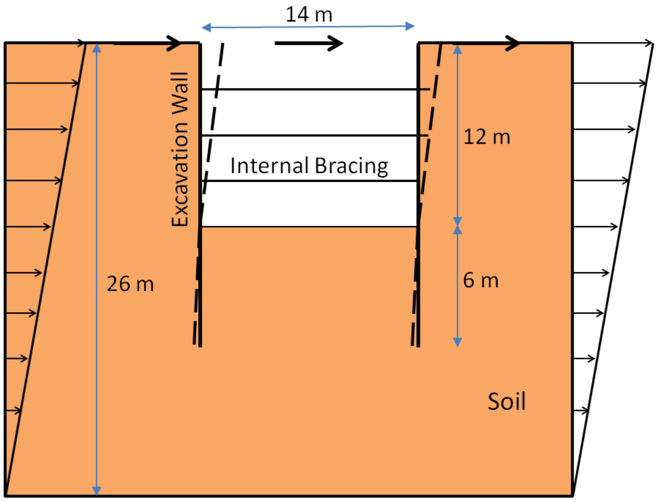

Figure 4-8. Schematic of racking deformations of the braced excavation shown with general dimensions of the modeled excavation in the centrifuge tests (deformations shown are not to scale).

4.2.1 Racking Displacements in the Far-Field Soil

During each centrifuge test, an array of accelerometers was placed half-way between a structure and the container boundary. This array was placed to best represent the free-field soil condition in each test. With the addition of the building in E-Midrise and E-Highrise, this array is in closer proximity to boundaries and structures than in E-No Bldg. Throughout the rest of this section, this array will be referred to as the far-field array because it may not represent a true free-field, due to some influence from the nearby structures. Referring back to the instrumentation layout drawings in the Centrifuge Testing Plan section, Figure 3-3 shows the accelerometers in E-No Bldg, where A22-A29 (bottom to soil surface) are considered the far-field array. Similarly, Figures 3-6 and 3-9 show the accelerometers A1-A7 and A1-A8 in E-Midrise and E-Highrise, respectively, representing the far-field.

Racking of the far-field soil over the height of the excavation was estimated by subtracting the displacement of the soil at a depth of 12 m from the displacement of the soil at the surface. Figure 4-9 shows the displacement time histories of these two elevations in the far-field soil column during the Northridge motion in E-No Bldg as an example, which was the first ground motion applied to the base of the container. The figure also shows the far-field racking time history. The maximum racking displacements experienced in the far-field were estimated in all the experiments and are summarized in Table 4-1.

The far-field was observed to experience larger racking in E-Highrise than E-Midrise, and they both showed larger racking compared to E-No Bldg. This increase in far-field racking was most likely due to the proximity of the far-field accelerometer array to structures and boundaries in the tests with a building. During E-No Bldg, the location of the far-field array was placed farther away from structures and the centrifuge container boundaries, and therefore these far-field measurements were taken as the free-field representation across all centrifuge tests. The base motions were compared among all experiments to ensure they were sufficiently similar in the frequency range of interest to allow this comparison.

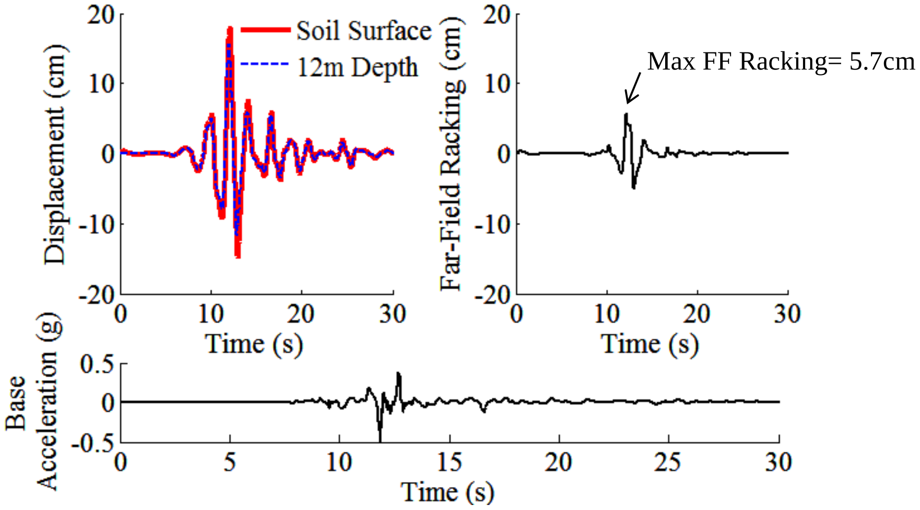

Figure 4-9. Displacement time histories in the far-field over the height of the excavation (soil surface and at a depth of 12m) are used to obtain the racking time history and maximum absolute racking in the far-field during the Northridge motion in E-No Bldg.

Table 4-1. Values of absolute maximum racking in the far-field over the height of the excavation during each motion in three centrifuge tests.

	E-No Bldg	**E-Midrise**	**E-Highrise**
Motion	FF Racking (cm)	FF Racking (cm)	FF Racking (cm)
Northridge	5.93	6.09	7.67
Loma Prieta	0.7	0.56	0.59
Joshua Tree	3.55	3.3	4.02
ChiChi	4.67	4.93	5.09
Lucerne	4.48	3.38	5.57
Kobe	6.41	7.08	8.49
Northridge Strong	-	8.28	10.59

4.2.2 Average Lateral Displacement and Racking of the Braced Excavation

Horizontal displacements of both excavation walls were measured separately during all three centrifuge experiments. During E-No Bldg the walls are referred to as the North Side and South Side. During the tests with a building, the two walls are referred to as the North or Open Side and the South or Bldg Side of the excavation, where the Open Side is the excavation wall away from the adjacent building and the Bldg Side is the excavation wall near the adjacent building. An accelerometer array was attached to each excavation wall to measure accelerations along the height of the two walls. In E-No Bldg, accelerometers A06-A11 (bottom to top) were placed on the south wall and accelerometers A15-A20 were on the north excavation wall (Figure 3-3). In E-Midrise, A40-A45 were on the South/Bldg Side and A47-A52 were on the North/Open Side as seen in Figure 3-6. A40-A45 were on the South/Bldg Side in E-Highrise and A47-A52 on the North/Open Side (Figure 3-9). Acceleration time histories along the excavation walls were double integrated with respect to time to obtain displacement time histories along the height of the wall. Two quantities were calculated from these measurements to analyze the displacements and deformations of the excavation wall: 1) the average absolute displacement along the whole height of the wall, and 2) the racking displacement of the wall (top with respect to the base of excavation at a 12m depth).

The average absolute displacement along the wall was calculated from the sum of displacements along the wall height divided by the total height of 18 m. This quantity represents the average horizontal displacement experienced by the whole wall. The racking displacement of the excavation wall was calculated similarly to the racking in the far-field, to evaluate the deflection of the top of the wall with respect to the base of excavation. Two accelerometer recordings on the excavation wall, at the soil surface and at a depth of 12 m, were converted to displacement, and the displacement at the bottom of the excavation was subtracted from the displacement at the top of the wall to calculate racking.

Figure 4-10 shows the time histories and Fourier amplitude spectra of these two displacement measurements for all three excavation tests during the Joshua Tree motion. The South/Bldg Side is plotted in the left column and the North/Open Side of the excavation in the right column. In Figure 4-10a, the average absolute displacement of the two excavation walls is shown for the three centrifuge tests. The average absolute displacement of the North/Open Side during E-Midrise could not be shown because of malfunctioning instruments during this motion. The total displacement experienced by the two excavation walls is shown to be similar in the time and frequency domains in a given test. Between the three excavation tests, however, E-Highrise experienced greater average absolute displacement than E-No Bldg or E-Midrise. The addition of an adjacent highrise building slightly increased the total horizontal displacement experienced by the braced excavation walls during a seismic event. This observation also applied to the majority of the other motions as shown in Figures 4-12a, 4-13a, and 4-14a, with the exception of the Northridge motion.

Figure 4-10b shows the racking displacement experienced by the two excavation walls during the Joshua Tree motion in all three tests. On the South/Bldg Side, racking is seen to decrease from E-No Bldg to E-Midrise and again from E-Midrise to E-Highrise. This is especially noted when racking displacement is represented in the frequency domain, but it can also be seen by comparing the racking time histories. In other motions, with the exception of Northridge (Figures 4-12b, 4-13b, and 4-14b), both sides of the excavation experienced a decrease in racking displacements from E-No Bldg to E-Midrise and then again from E-Midrise to E-Highrise.

Figure 4-11 shows the displacement response of the excavation walls during the Northridge motion of the three centrifuge tests. In terms of average absolute displacement, E-No Bldg showed slightly higher total displacements for both excavation walls when compared to E-Midrise and E-Highrise. Also, on the North/Open Side of the excavation, E-Midrise experienced less racking than E-No Bldg, but E-Highrise showed larger racking displacements compared to the other tests and the South/Bldg wall during this same test. These opposite observations from other motions could be attributed to a looser soil condition, lack of proper contact between the backfill soil and the structures, or the pulse-like energy of the motion in this case.

Another important observation made from these plots was the comparison of racking experienced by the two excavation walls in a given test. During E-No Bldg, the excavation experienced symmetric loading on the two walls. During E-Midrise and E-Highrise, a building was placed on one side of the underground structure, creating an asymmetric loading scenario. In terms of average absolute displacement, the tests with a building showed the North/Open Side displacing slightly greater than the South/Bldg Side, but relatively similar total horizontal displacements were observed for both walls during a given test. However, racking displacement was observed to be greater on the North/Open Side of the excavation when compared to the South/Bldg Side of the excavation in all motions during the tests with a building as a result of the asymmetric model. The presence of the tall adjacent building appeared to alter the response on the two excavation walls in terms of racking displacements and cause asymmetry, despite their connection through struts.

As an example, in the Fourier amplitude spectra of Figure 4-12b, reduction in racking is shown on both sides of the excavation, but this reduction was greater on the South/Bldg Side than the North/Open Side during both E-Midrise and E-Highrse. The presence of the building constrained the South/Bldg Wall and caused a reduction in racking displacement on this wall during every motion. The reduction was observed in E-Midrise from E-No Bldg, but became more prevalent with the addition of the highrise building.

The trends seen in these figures of racking displacements can also be deduced from the maximum racking value experienced by each wall during the tests. Table 4-2 summarizes the values of maximum absolute racking displacement recorded on each wall during the three centrifuge experiments. Overall, the maximum racking experienced decreased on both walls from E-No Bldg to E-Midrise and then again from E-Midrise to E-Highrise, with the exception of the North/Open Wall of E-Highrise during the Northridge motion. Also from these values, the North/Open Wall in the tests with a building is seen to have greater racking displacements than the South/Bldg Wall during the same test.

The horizontal displacements observed on the two braced excavation walls at different elevations in E-Highrise are visually shown in the simplified sketches of Figure 4-15 during three representative motions. The dimensions shown are displacements of the excavation walls at the time of maximum racking on the North/Open Wall. The sketches show displacements at four elevations on the wall: the top, bottom of the excavation at a depth of 12m, middle of the excavation depth at 6m, and bottom of the wall at 18m depth. The difference in the displacement response of the two walls occurred in the relative displacement between the top of the wall and the bottom of the excavation. The building basement adjacent to the South/Bldg Wall of the excavation forced this excavation wall to move more together horizontally, which reduced the racking on that wall. The North/Open Wall away from the building did not have an adjacent structure at this proximity and therefore experienced more racking deformations for a similar average overall displacement.

In summary, the presence of an adjacent building slightly increased the total lateral displacement of the excavation walls, but reduced their relative deflection that is a more critical measure of performance. In other words, with the presence of the adjacent structure, the excavation walls experienced displacements across the whole wall but deflected less. Also, the presence of a tall building on one side of the excavation led to an asymmetric racking deformation pattern on the walls, despite their connections through struts.

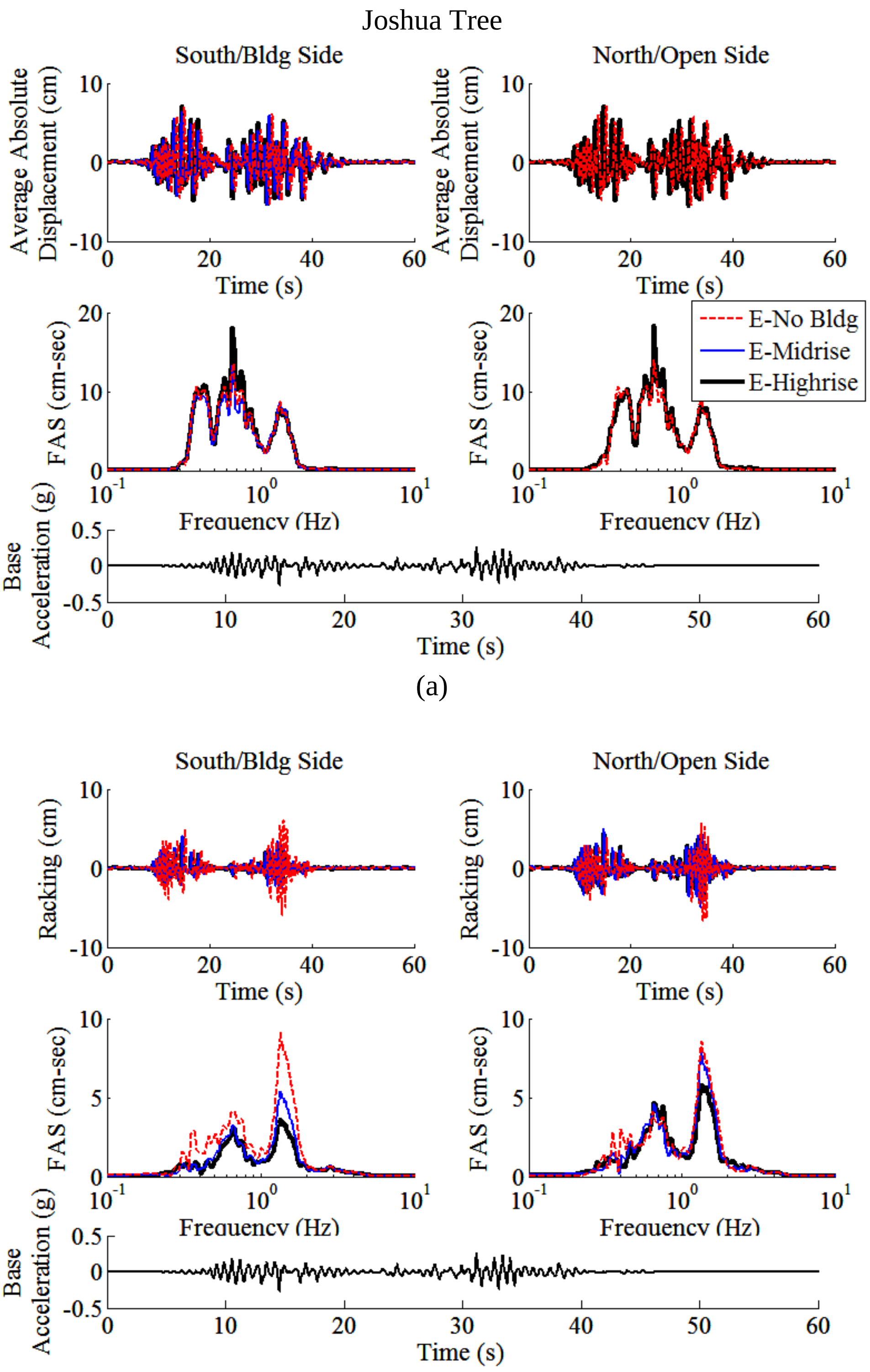

(b)

Figure 4-10. Displacements measured on the excavation walls in E-No Bldg, E-Midrise, and E-Highrise in both time and frequency domains during the Joshua Tree motion: (a) the average absolute displacements of the excavation walls; (b) racking displacement of the walls (relative displacement of top with respect to the base of the excavation).

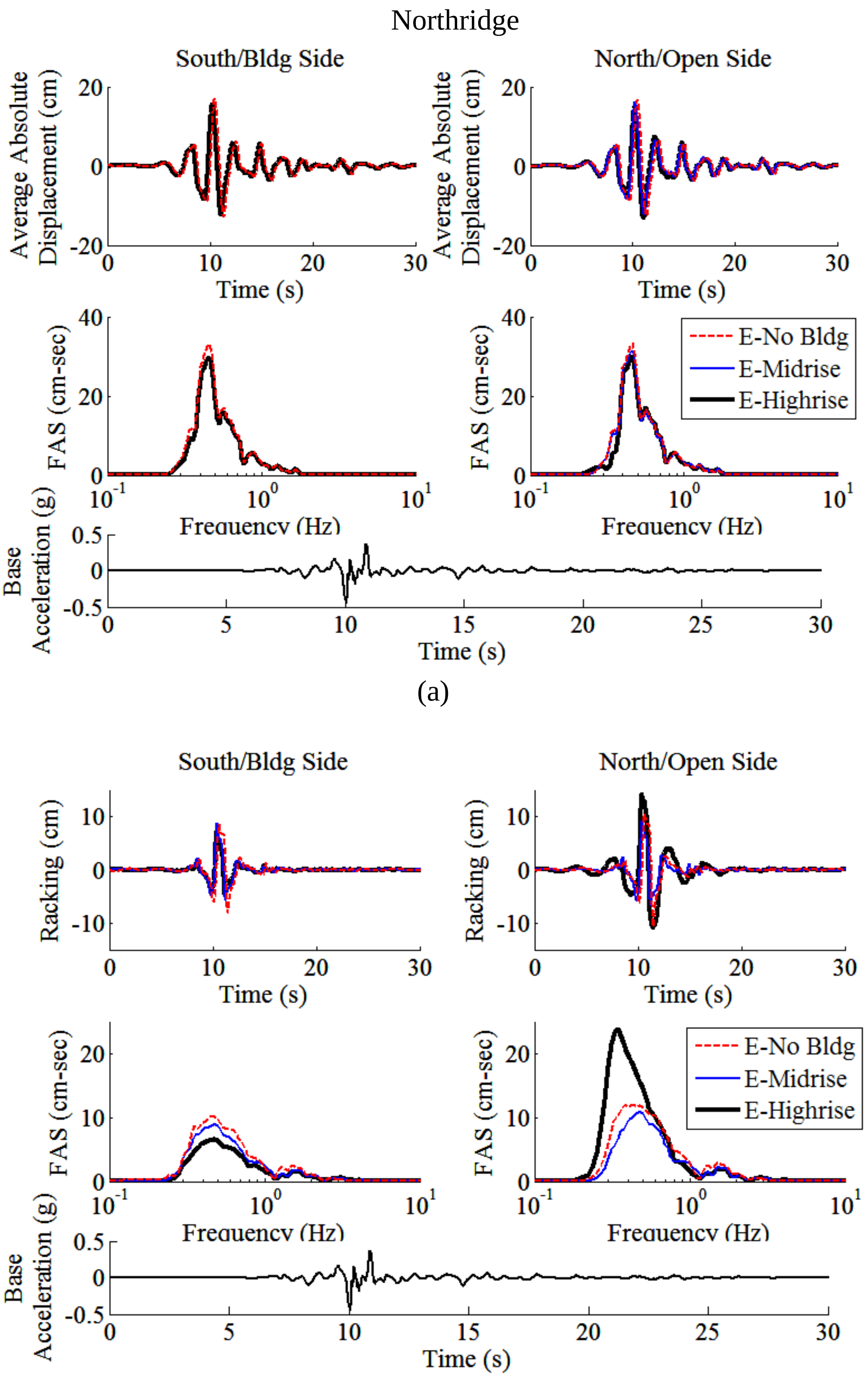

(a)

(b)

Figure 4-11. Displacements measured on the excavation walls in E-No Bldg, E-Midrise, and E-Highrise in both time and frequency domains during the Northridge motion: (a) the average absolute displacements of the excavation walls; (b) racking displacement of the walls (relative displacement of top with respect to the base of the excavation).

Chi Chi

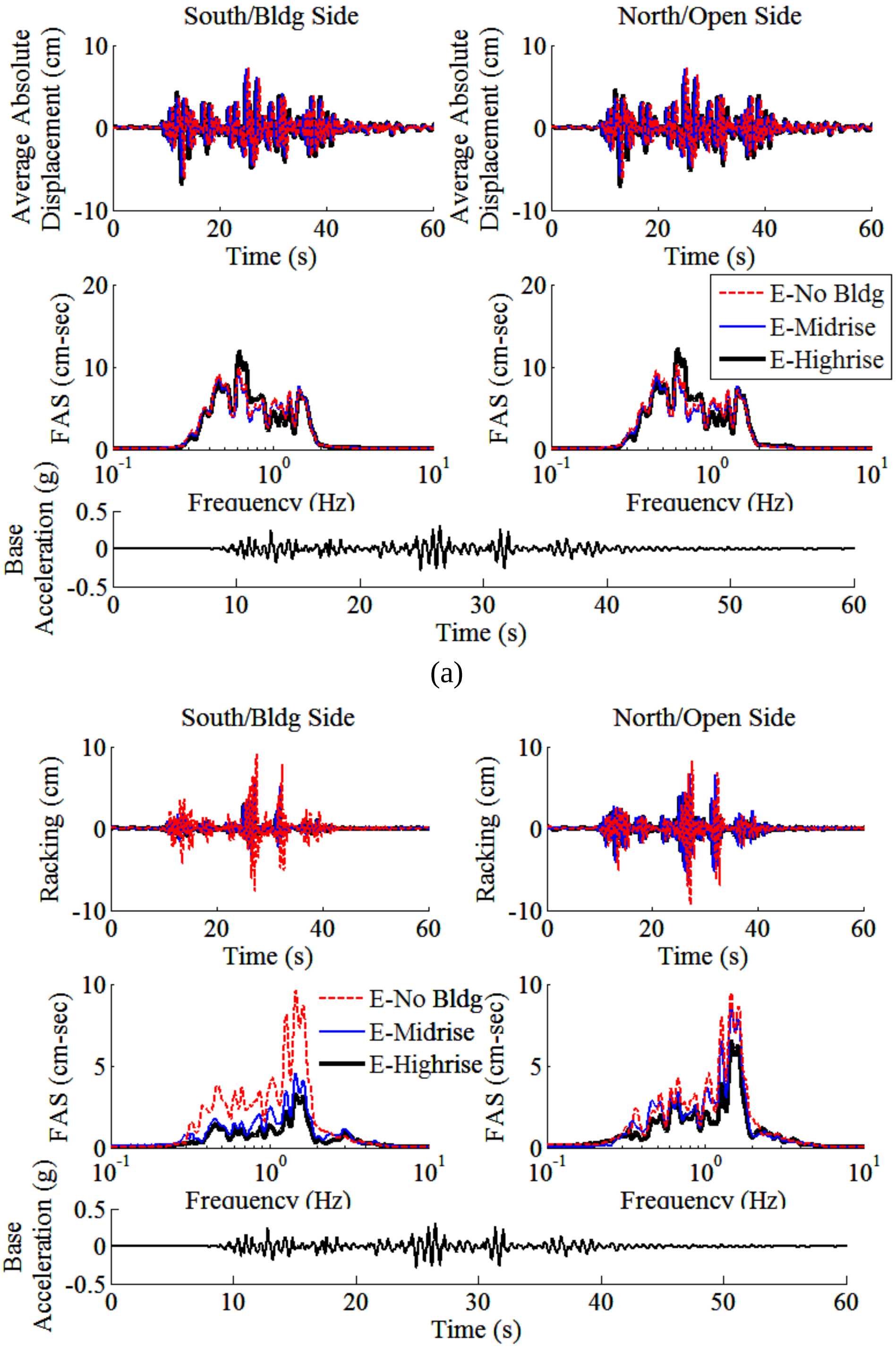

(a)

(b)

Figure 4-12. Displacements measured on the excavation walls in E-No Bldg, E-Midrise, and E-Highrise in both time and frequency domains during the Chi Chi motion: (a) the average absolute displacements of the excavation walls; (b) racking displacement of the walls (relative displacement of top with respect to the base of the excavation).

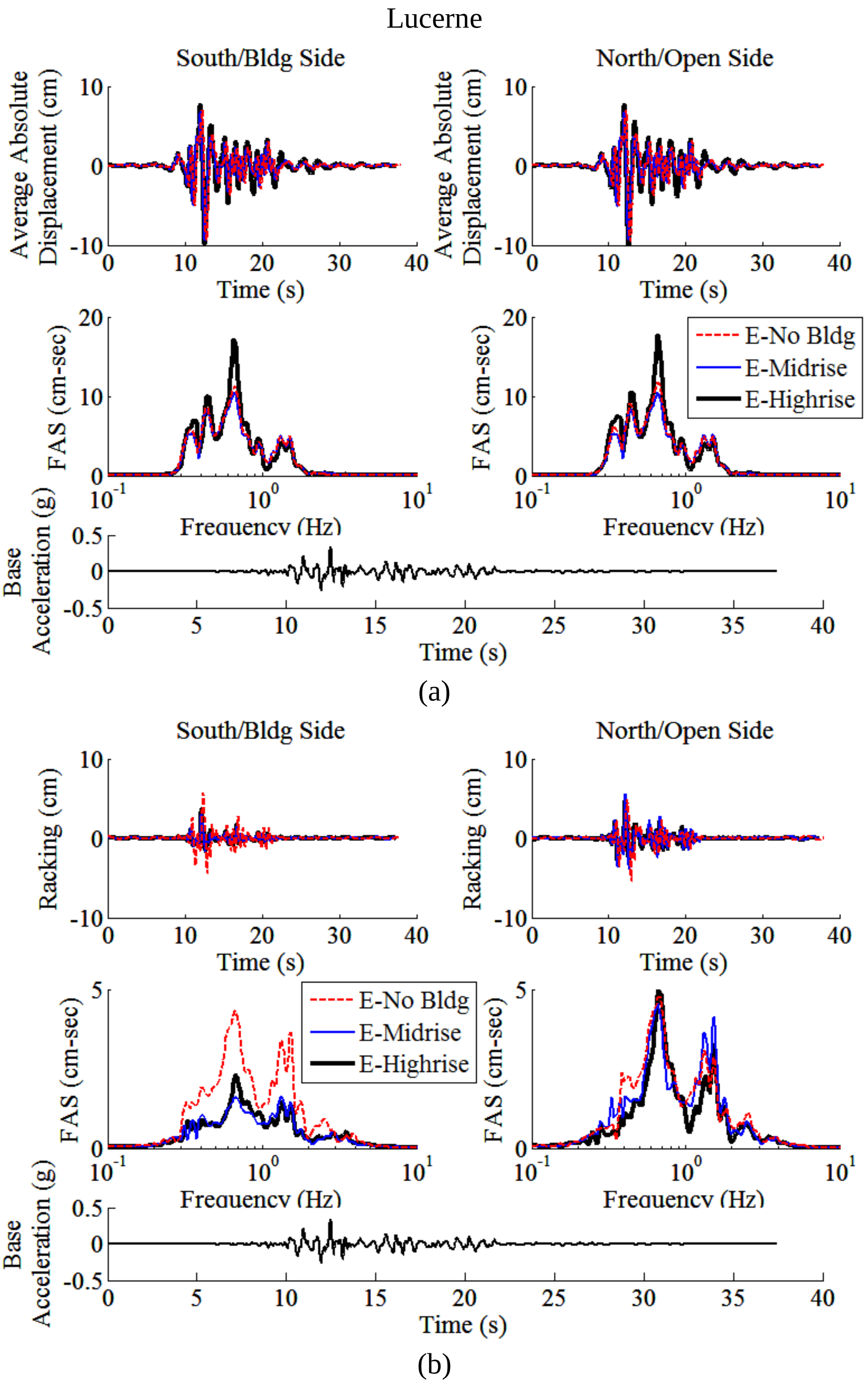

Figure 4-13. Displacements measured on the excavation walls in E-No Bldg, E-Midrise, and E-Highrise in both time and frequency domains during the Lucerne motion: (a) the average absolute displacements of the excavation walls; (b) racking displacement of the walls (relative displacement of top with respect to the base of the excavation).

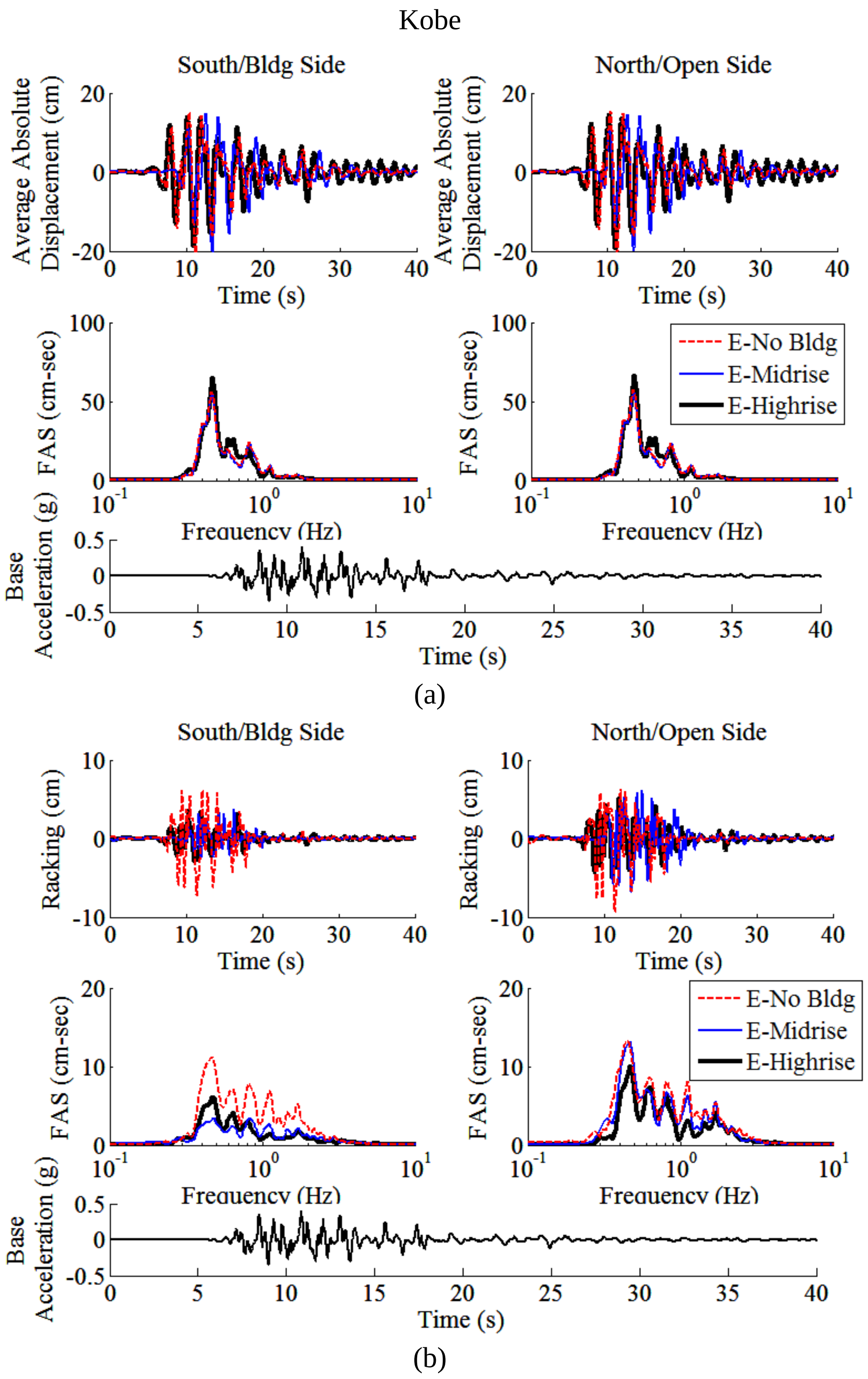

Figure 4-14. Displacements measured on the excavation walls in E-No Bldg, E-Midrise, and E-Highrise in both time and frequency domains during the Kobe motion: (a) the average absolute displacements of the excavation walls; (b) racking displacement of the walls (relative displacement of top with respect to the base of the excavation).

Table 4-2. Values of absolute maximum dynamic racking displacements recorded on the two sides of the braced excavation during each motion in the three centrifuge tests.

		E-No Bldg Racking (cm)		E-Midrise Racking (cm)		E-Highrise Racking (cm)	
Motion	Base PGA (g)	South Wall	North Wall	South Wall (Bldg Side)	North Wall (Open Side)	South Wall (Bldg Side)	North Wall (Open Side)
Northridge	0.47	8.64	10.56	8.77	9.28	7.2	14.17
Loma Prieta	0.1	1.11	1.2	0.718	1.08	0.62	1.02
Joshua Tree	0.27	5.99	6.69	4.07	5.06	3.81	4.41
ChiChi	0.37	9.06	9.32	5.79	6.76	4.01	4.91
Lucerne	0.38	5.71	5.44	3.42	5.548	3.69	4.71
Kobe	0.5	7.24	9.39	3.74	6.75	3.54	5.15
Northridge Strong	0.53			5.26	7.34	7.78	7.5

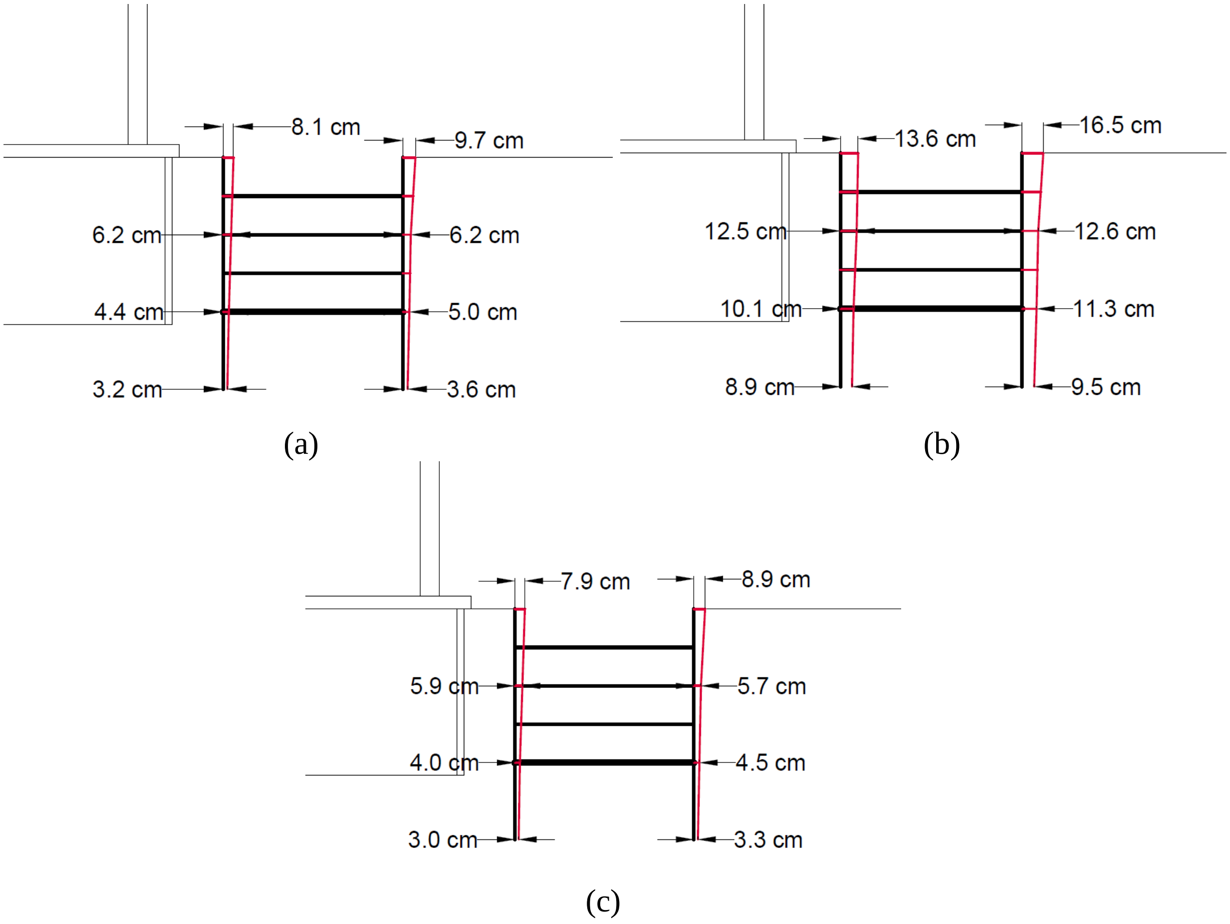

Figure 4-15. Simplified sketch showing the effect of the adjacent building during E-Highrise on the braced excavation in terms of dynamic average horizontal displacements and racking deformations at the time of peak racking on the North/Open side of the excavation during (a) Lucerne, (b) Kobe, and (c) Joshua Tree. (Horizontal displacements are exaggerated for visual purposes in the simplified sketches)

4.2.3 Comparison of Racking Displacements on the Excavation and Far-Field Soil

The racking measurements in these centrifuge tests were compared to the NCHRP 611 guidelines for racking of rectangular underground box structures, which is based on work by Wang (1993). According to the NCHRP 611 report, the flexibility ratio of an underground structure is defined as Eq. 2-1 presented in Chapter 3. The flexibility ratio (F) is a measure of the racking stiffness of the surrounding soil to the racking stiffness of the structure itself. With a known F, the racking ratio (R) of the structure can be estimated using the following relation:

$$R = \frac{2F}{(1+F)} \qquad \text{(Eq. 4-8)}$$

The racking ratio (R) is also defined as the ratio of the peak absolute racking deformation of the structure to peak absolute racking of the free-field soil (Wang 1993). This definition, Eq 2-2, was used to experimentally find the racking ratio for each ground motion during each centrifuge test.

In the calculation of the flexibility ratio, B = 14m and H = 12m from the excavation dimensions, and a structure racking stiffness of 1.5 MPa was estimated to represent the excavation from numerical simulations performed in Abaqus. Also for the calculation, G_m needed to be obtained for each ground motion. In the process of estimating $G_{m,}$ uncertainties existed such that a range of flexibility ratios could be calculated. The strain over the height of the excavation in the free-field was estimated first during each shake from accelerometers within the best representative far-field array. As discussed earlier, the far-field array in the baseline tests, T-No Bldg, was found most representative of free-field conditions. Racking in the far-field over the height of the underground structure was divided by the height of the excavation, 12 m, to calculate the strain time history in the far-field. The maximum far-field soil shear strain ($\gamma_{\max}$) and effective shear strain level ($0.65*\gamma_{\max}$) were then obtained for each motion, as shown in Figure 4-16.

The median shear modulus reduction curve proposed by Darendeli (2001) at the overburden pressure corresponding the mid-height of the excavation (6 m) was adopted and corrected for implied shear strength based on two different shear wave velocity profiles, as detailed by Romero et al. (under review). The shear wave velocity profiles were chosen based on the measured soil properties discussed in the previous section. The empirical relations proposed by Seed and Idriss (1970), Bardet (1993), Menq (2003), Jamiolkowski et al (1991), and Hardin and

Drnevich (1972) were considered. The average of these five relations and the upper bound shear wave velocity profile from Seed and Idriss (1970) were found to best represent the soil properties that were measured during the centrifuge tests, as described in Section 4.1. These empirical shear wave velocity profiles were used to correct the shear modulus reduction curve. The two corrected median Darendeli (2001) shear modulus reduction curves and their +/- 1 standard deviation curves, Figure 4-17, were used together with the effective shear strain level in the far-field to obtain a range of six G/G_{max} values. These values were unnormalized using the corresponding G_{max} value at the mid-height of the excavation as estimated from the shear wave velocity profile used for the implied shear strength correction. This procedure resulted in six values of mean, strain-compatible, shear moduli, G_m, of the soil in the far-field that were used in the calculation of the flexibility ratio.

The experimental values of racking and flexibility ratios were produced for each earthquake event in E-No Bldg, E-Midrise, and E-Highrise and are compared to the NCHRP 611 relation in Figure 4-18. The two sides of the excavation are shown separately due to their differences in racking displacements. The median and +/- 1 standard deviation of the flexibility ratio range for each motion is represented by error bars in Figure 4-16. The reduction in racking from E-No Bldg to E-Midrise and then again from E-Midrise to E-Highrise can also be observed from the decrease in racking ratio. The one exception to this trend, as shown before, was on the North/Open Side of E-Highrise during the Northridge motion. This large racking is seen also in Figure 4-18b. Overall, the experimental data from E-No Bldg shows good agreement with the NCHRP 611 relation. However, this relation was found to slightly overestimate the expected racking of a deep, braced excavation with adjacent highrise buildings, especially if buildings were to be located on both sides of the underground structure.

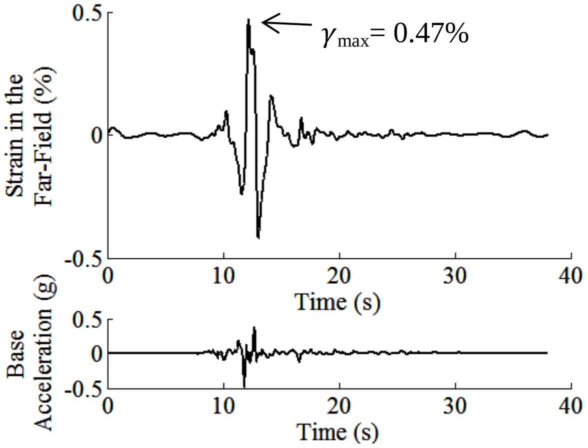

Figure 4-16. Maximum strain picked off of the strain time history in the far-field over the height of the excavation during the Northridge motion in T-No Bldg.

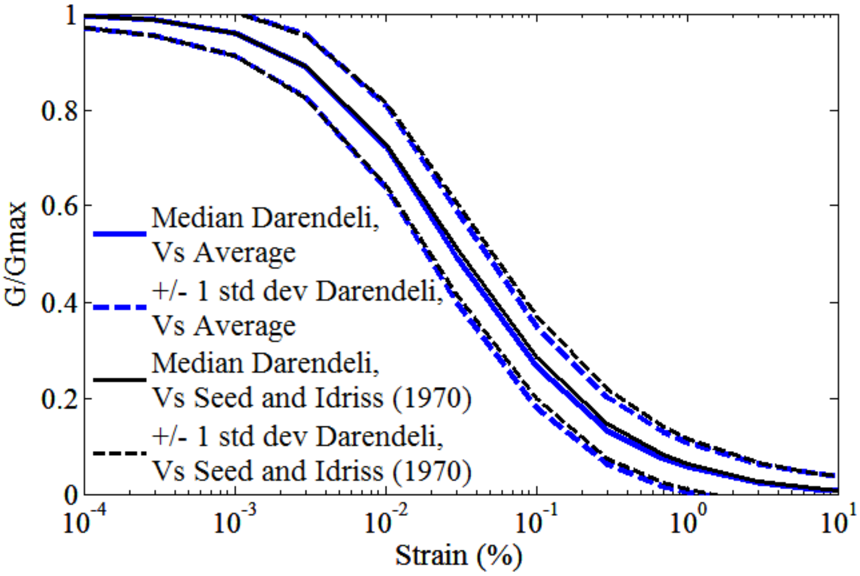

Figure 4-17. Darendeli (2001) modulus reduction curves corrected for implied shear strength using two different shear wave velocity profiles: Seed and Idriss (1970) and an average of the five empirical relations for V_s presented in section 4.1.

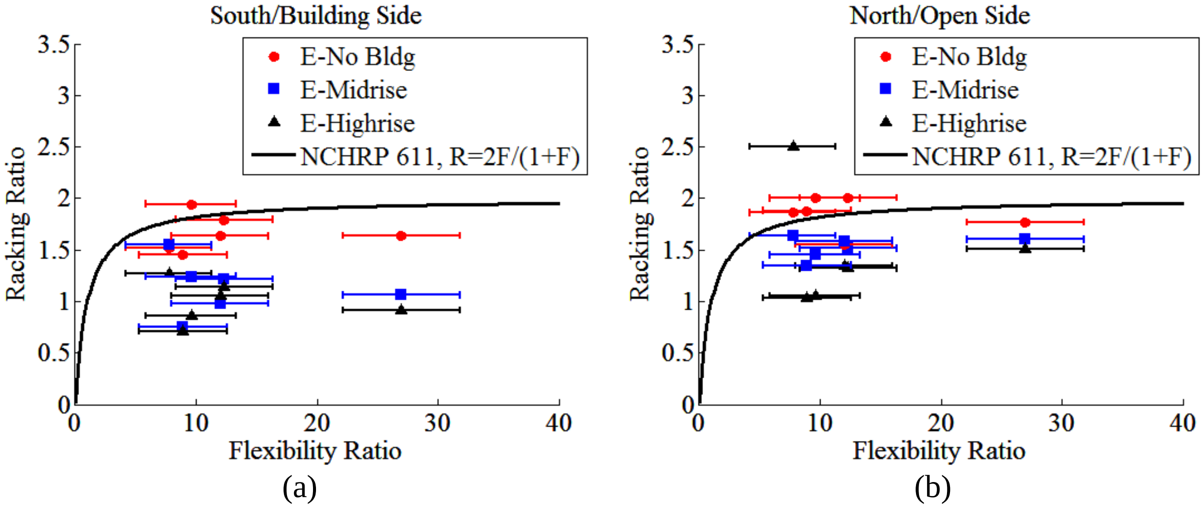

Figure 4-18. Ranges of racking versus flexibility ratio measured on: (a) the south or building side of the excavation; and (b) the north or open side of the excavation during all motions compared to the NCHRP guideline.

4.4 Static and Seismic Lateral Earth Pressures

Static and seismic lateral earth pressures on the excavation walls were a critical measurement taken during the centrifuge experiments. Earth pressures were obtained by three methods: 1) direct measurements by tactile pressure sensors, 2) indirect measurements using bending strain gauges and accelerometers along the excavation walls and axial strain gauges on the struts, and 3) indirect measurements using the axial forces on the excavation struts. All three of these methods are described in this section and their results are compared. Figure 4-19 highlights the instrumentation on the excavation wall that was used in measuring lateral earth pressures. All methods were used to estimate lateral earth pressures from the soil surface to the base of excavation (i.e., depth of 12 m beneath the surface).

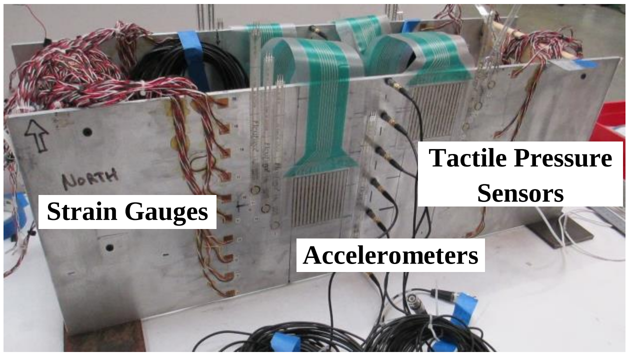

Figure 4-19. Instrumentation on the temporary excavation wall used to measure lateral earth pressures: tactile pressure sensors, accelerometers, and strain gauges.

4.4.1 Direct Pressure Measurements with Tactile Sensors

The tactile pressure sensors used in the experiments were made by Tekscan Inc. Preparation of sensors for testing includes static and dynamic calibration, equilibration, and conditioning. Equilibrating and static calibration was performed with a pneumatic loading device before sensor installation. If trapped air in the sensor was observed it was removed by poking a small hole in the sensor area, releasing the trapped air by placing the sensor through a roller device, and placing a small piece of tape over the hole to seal it. A previously determined, frequency-dependent dynamic calibration was applied during data analysis. Also, conditioning of the sensors was performed with the pneumatic device prior to calibration as well as during spin-up of the model in centrifuge. These preparation and calibration details are critical when working with tactile pressure sensors in centrifuge (Dashti et al. 2012 and Gillis et al. 2015).

Two tactile sensors were placed on each side of the excavation as shown schematically in instrumentation Figures 3-5, 3-8, 3-11. The sensors were installed with a weak double sided tape that held the sensor and its stem on the excavation wall, as shown in Figure 4-20. Great precaution was taken to seal the stem of the sensor at the top of the excavation walls to avoid sand entering the space between the sensor and the wall, which could affect measurements.

The sensels (measuring points) on each tactile sensor directly measured earth pressures between depths of 0.7 to 4.6 m and again from 6.8 to 10.7 m, with a gap in between. Each sensor contained 14 rows by 14 columns of sensels. Pressure was recorded at 4,000 samples per sec (sps) on each sensel during earthquake loading. Then 9-cell averaging was used to obtain one pressure time history at each row of sensels corresponding to a given depth, as detailed by Gillis et al. (2015). The pressure in between the two sensors was approximated using linear interpolation when needed for analyses. Pressure data were also extrapolated at the top and bottom of the profile to cover the height of the excavation when estimating thrust.

During E-No Bldg and E-Midrise, 50 psi capacity sensors were used on both sides of the excavation walls. During E-Highrise 50 psi capacity sensors were used on the North/Open Side of the excavation and 100 psi capacity sensors were installed on the South/Bldg Side of the excavation with the expectation of larger earth pressures (observed during E-Midrise). The low signal to noise ratio (SNR) of these high capacity sensors on the building side of the excavation resulted in poor recordings. Hence, their measurements are not presented in E-Highrise. Also, the tactile pressure sensors on the South Side of the excavation during E-No Bldg were damaged so the baseline test was represented by pressure data along the North Wall only.

The static lateral earth pressures were measured before an earthquake motion was applied. A total earth pressure profile was measured at each time step throughout the seismic event. The dynamic increment of earth pressure at each depth was then calculated by subtracting the static pressure before the event from the total earth pressure at each time. At each instance of time, a dynamic thrust was also calculated from integrating the dyanmic increment of earth pressures along the excavation height (only focusing on the height of the wall above the excavation).

Figures 4-21, 4-22, and 4-23 summarize the results obtained from tactile pressure sensors for the three centrifuge experiments during the Northridge, Lucerne, and Kobe motions, respectivley. The first column shows the results from E-No Bldg, followed by results from E-Midrise and E-Highrise. The first row shows the dynamic thrust time histories measured by tactile pressure sensors over the height of the excavation walls. The time of maximum dynamic thrust is highlighted in these time histories. At this time, the total earth pressure profile is shown in the second row of plots along with the static earth pressures measured before the corresponding earthquake. In the third row, the dynamic increment of earth pressure profile is shown at the time of maximum thrust. Data for both excavation walls was measured in E-Midrise, which are presented. Reliable data from tactile pressure sensors was measured only on the North/Open Wall during E-No Bldg and E-Highrise so only one data set is presented for those tests. Note that struts were placed at depths of 3, 6, and 9 m.

The figures showing pressure profiles are also compared to Rankine's theory of active and at-rest triangular pressure profiles assuming a unit weight of the Nevada Sand corresponding to 55% relative density ($\gamma_{\text{soil}} = 15.4\ \frac{kN}{m^3}$) and a friction angle of 33°. The measured pressure profiles are also compared to the apparent earth pressure diagram for a braced excavation in sand as proposed by Peck (1969). The equations to obtain these empirical profiles are shown in the equations below, where D is the depth in question and H is the full height of the wall.

$$P_{active} = K_a \gamma_{soil} D, where\ K_a = \tan^2\left(45 - \left(\frac{\varphi'}{2}\right)\right) \quad \text{(Eq. 4-9)}$$

$$P_{at-rest} = K_o \gamma_{soil} D, where\ K_o = 1 - \sin\varphi' \quad \text{(Eq. 4-10)}$$

$$P_{apparent} = 0.65 K_a \gamma_{soil} H, where\ K_a\ is\ the\ same\ as\ above \quad \text{(Eq. 4-11)}$$

Dynamic thrust increased from E-No Bldg to E-Midrise and then again from E-Midrise to E-Highrise consistently during all motions. Before any shaking, prior to the Northridge motion, the static earth pressure profiles increased with depth and roughly corresponded to values between the theoretical active and at-rest lateral earth pressures in all tests. The apparent pressure profile (Peck 1969) was often slightly greater than the static earth pressures measured on the excavation walls.

In E-No Bldg, the static and dynamic pressure profiles showed a jump in pressure at the elevation corresponding to the lowest strut level, 9 m depth. When an adjacent building was present, an increase in dynamic pressure was also observed at depths near 3 to 6 m, most likely from the loads imposed by the top and middle struts. As shown in the Soil Properties section, the soil was observed to densify as more shakes were applied throughout a given test. These changes in soil properties are also evident in the static pressure recordings. Further, the denser soil may have amplified the dynamic pressures on the excavation walls (e.g., comparing Lucern dynamic pressures with Northridge).

In the case of E-Midrise, pressure sensors measured data on both sides of the excavation. The South/Bldg Side was seen to show higher static and dynamic pressures than the North/Open Side due to the extra surcharge on this side of the excavation. This is especially noticeable toward the top of the excavation wall. Importantly, dynamic pressures increased on both sides of the wall with the addition of an adjacent tall building. Ultimately, an increased pressure on the South/Building Side increased pressures on the North/Open wall as well.

Lastly, these plots show the shape of the dynamic increment of pressure measured by tactile sensors at the time of maximum thrust. The dynamic pressure is shown to increase with depth on both walls and during all three centrifuge tests. The centriod of the dynamic pressure profile will be discussed in more detail later in this section.

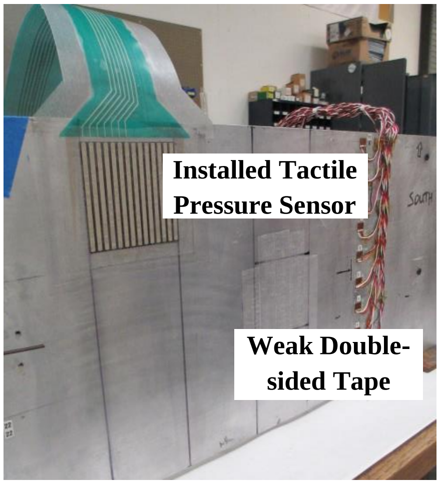

Figure 4-20. Installing the tactile pressure sensors with weak, double-sided tape at the two elevations on the excavation walls.

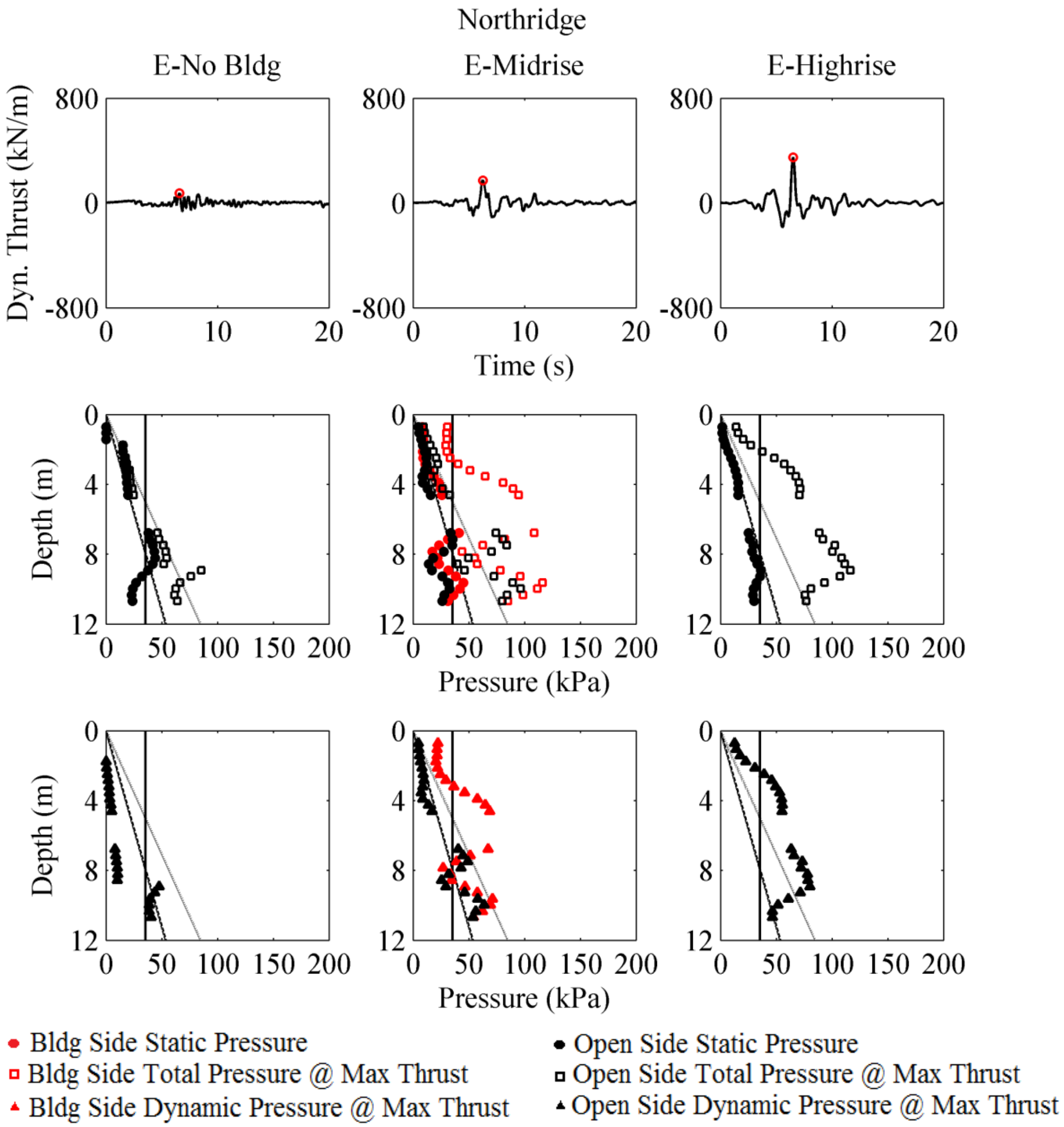

Figure 4-21. Results from the tactile pressure sensors on the excavation walls during the Northridge motion in the three excavation experiments.

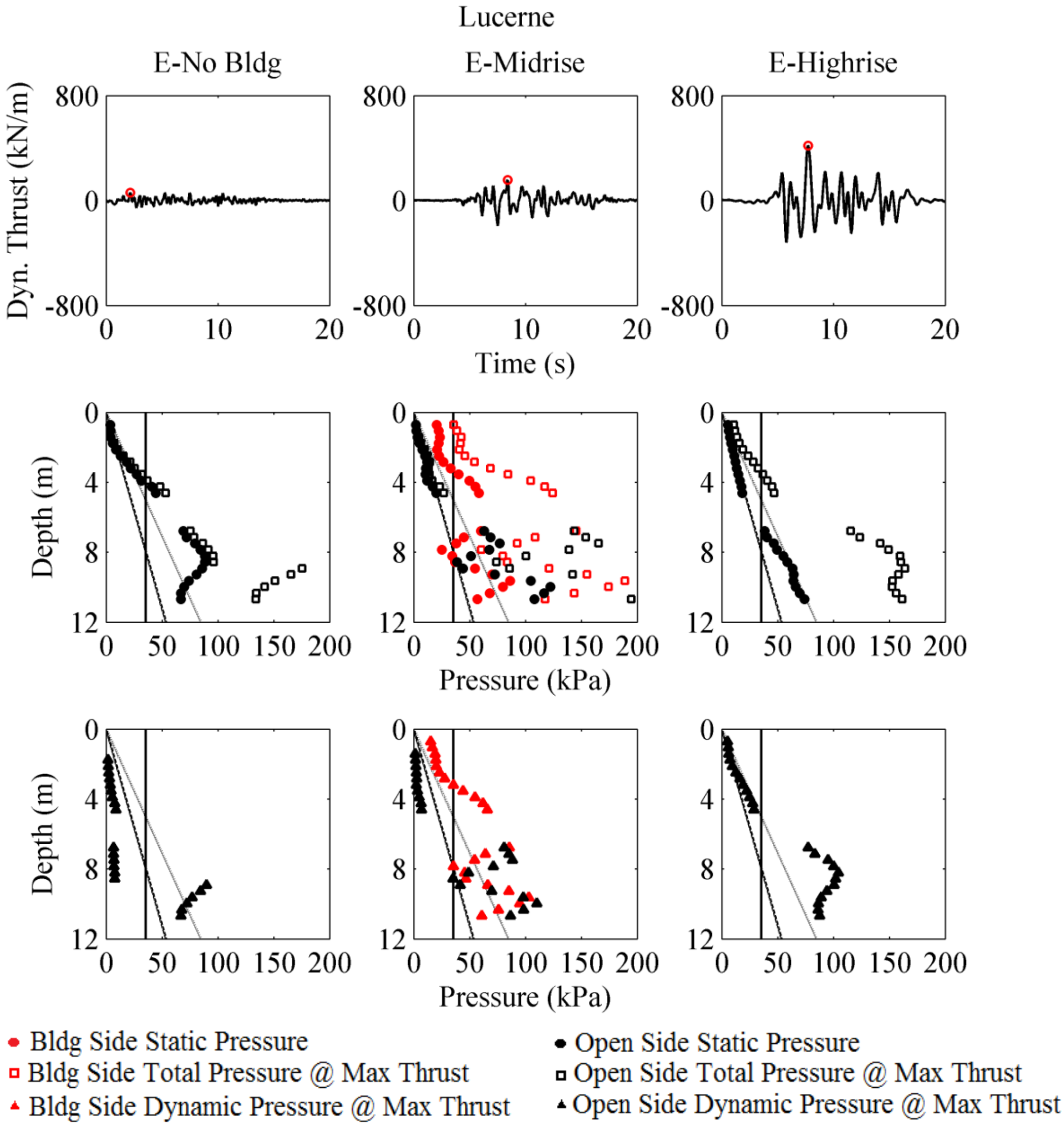

Figure 4-22. Results from the tactile pressure sensors on the excavation walls during the Lucerne motion in the three excavation experiments.

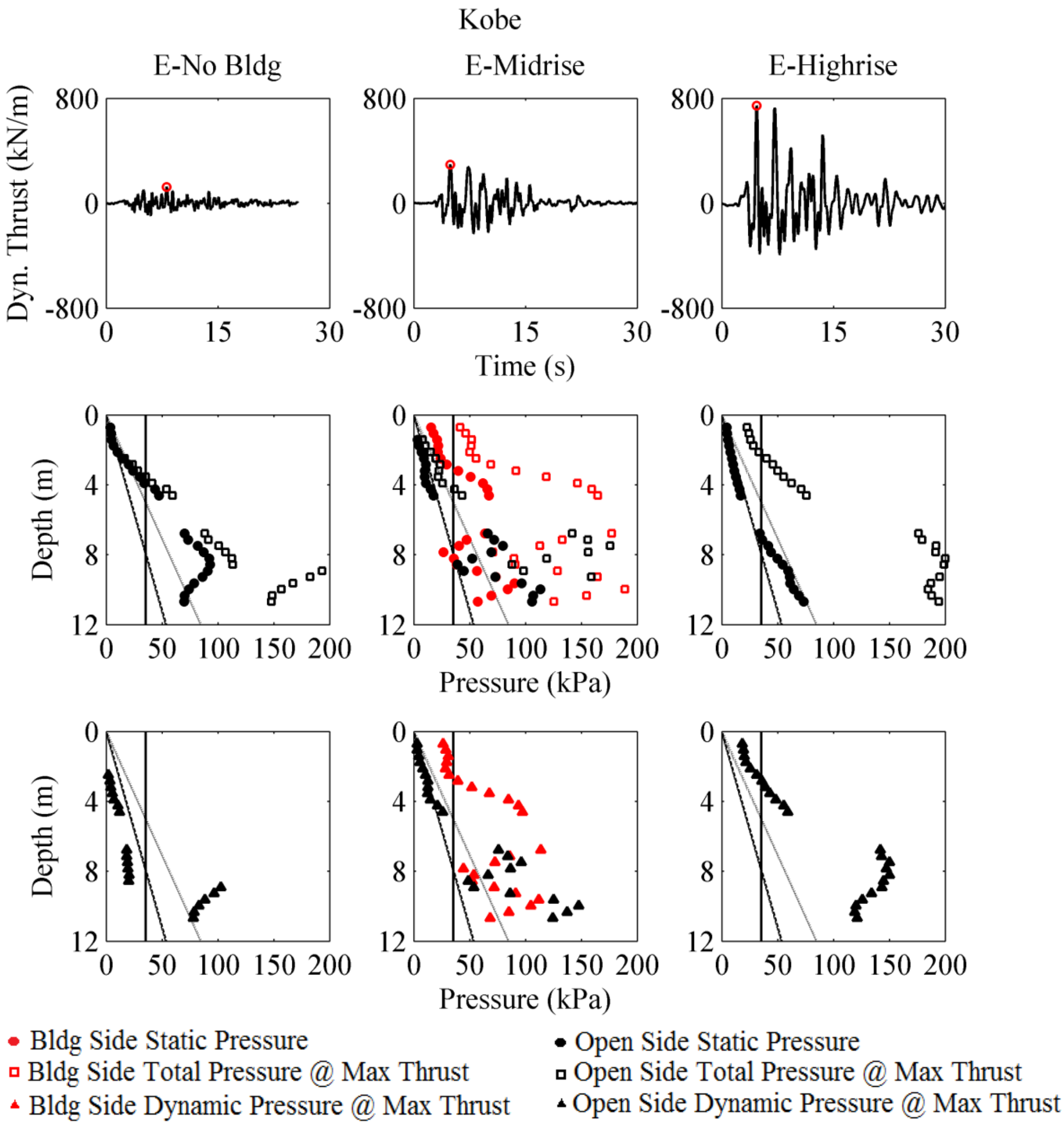

Figure 4-23. Results from the tactile pressure sensors on the excavation walls during the Kobe motion in the three excavation experiments.

4.4.2 Indirect Pressure Measurements with Strain Gauges

The tactile pressure sensors measured lateral earth pressures directly, which was advantageous. However, their response is highly sensitive to trapped air inside the sensor. Therefore, it was important to have other means of obtaining pressure in parallel. Lateral earth pressures can also be back-calculated from strain gauges along a retaining wall. Even though it is an indirect measurement of pressure, the computation has been completed with successful results by other researchers in the past (Mikola 2012 and Al Atik 2008).

In this section, bending strain gauges and accelerometers along the excavation walls as well as axial strain gauges on the struts (e.g., Figure 4-24) are used to calculate static and seismic earth pressures. Referring back to the instrumentation layout in the Centrifuge Testing Plan section, strain gauges (SG) 1–20 and SG29–34 were used in E-No Bldg (Figure 3-4) and SG1–20 and SG29–39 were used in E-Highrise (Figure 3-10). Unfortunately, the strain gauges on the excavation struts during E-Midrise did not save data. Hence, pressure could not be estimated from strain gauges in this test. The same accelerometers used for the displacement and racking measurements were also used in this process of back-calculating pressure.

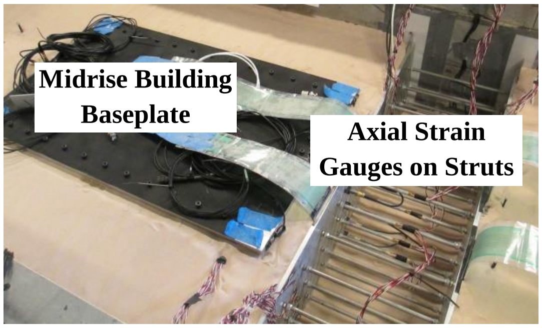

Figure 4-24. Excavation struts with axial strain gauges installed in the temporary excavation during model construction of E-Midrise.

Static bending moments on the excavation walls are caused by the lateral earth pressures applied from the backfill soil and the forces from struts. Dynamically, the bending moments along the wall are caused by seismic lateral earth pressures, seismic axial forces from struts, and the wall inertia. In order to calculate the static and dynamic lateral earth pressures from bending moments that are measured by strain gauges on the walls, the bending moment caused by the components other than earth pressure must be estimated and removed from the total bending moment profile (Roozbeh 2012; Al Atik 2008). The process of obtaining static and dynamic earth pressures is described here step-by-step. Figures at each step of the process and at one instance in time are presented as an example to clarify the process and assumptions.

The first step was to calculate bending moment from the bending strain measured by the strain gauges. Assuming the walls behaved like an Euler-Bernoulli beam, the strain was converted to moment using the following equation.

$$M = \frac{\varepsilon E I}{c} \quad \text{(Eq. 4-12)}$$

where E is the modulus of elasticity of aluminum, which was taken as 69e6 kN/m^2, I is the moment of inertia of the wall per unit length of the excavation (all units in prototype scale), and c is half the width of the excavation wall. The static bending moment profile of the two excavation walls before the first motion during E-No Bldg is shown in Figure 4-25. The elevations of the struts and the bottom of the excavation are indicated in these figures.

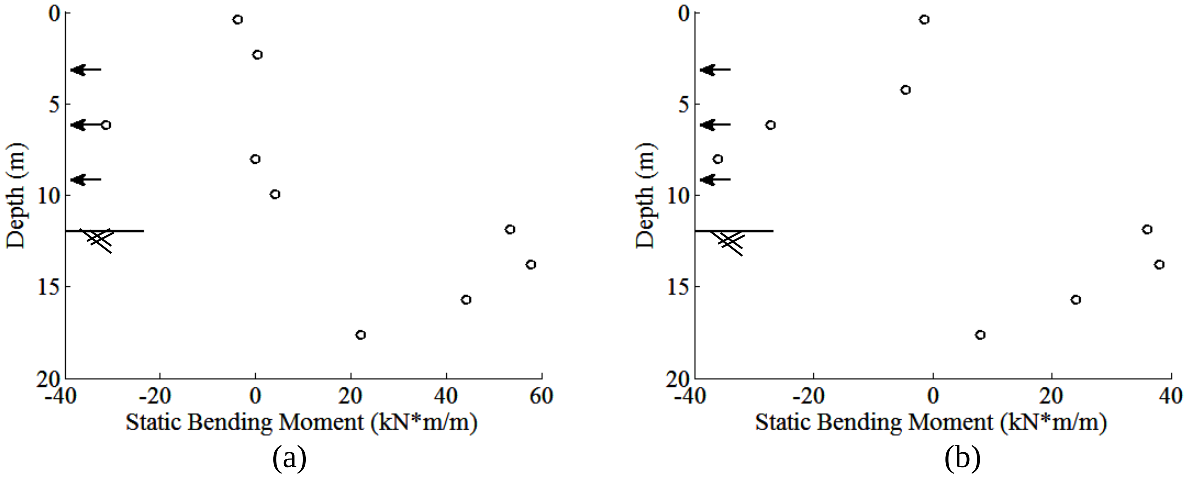

Figure 4-25. Static bending moment on (a) the south wall and (b) the north wall of the temporary excavation prior to the Northridge motion of E-No Bldg.

Statically, the earth pressure and the strut loads cause strain in the excavation walls. The bending moment caused by the strut loads must be estimated and subtracted from the profiles shown in Figure 4-25 to obtain the bending moment profiles from earth pressure only. The axial strain in each strut was measured by axial strain gauges. The axial strain was converted to axial force assuming linear-elastic behavior:

$$F = AE\varepsilon \quad \text{(Eq. 4-13)}$$

where A is the cross-sectional area of the hollow circular strut (0.064 m^2 in prototype scale) and E is the modulus of elasticity of the aluminum strut. In this way, the total axial force was measured on each excavation strut at each time. It was assumed for all centrifuge tests that half of this axial force was applied back to each wall as a reaction force.

The bending strain caused by three strut forces on the excavation wall was estimated by assuming a depth at which the wall was constrained to rotate. When a force and moment balance calculation was performed assuming static soil pressures, the point of no rotation was calculated to be near the very bottom of the wall. However, in the measured static bending moment profiles (e.g., Figure 4-25), the largest bending moments consistently measured near a depth of 14 m. The bending moment near the bottom of the wall approaches zero. Therefore, the depth where the largest bending moment was measured within the embedded area of the wall was chosen as the assumed point of no rotation in order to estimate the bending moment profile caused by strut axial forces, shown in Figure 4-26. Because the force on the strut was assumed to be applied by both walls equally, the profile of the bending moment caused by strut forces is the same for both excavation walls.

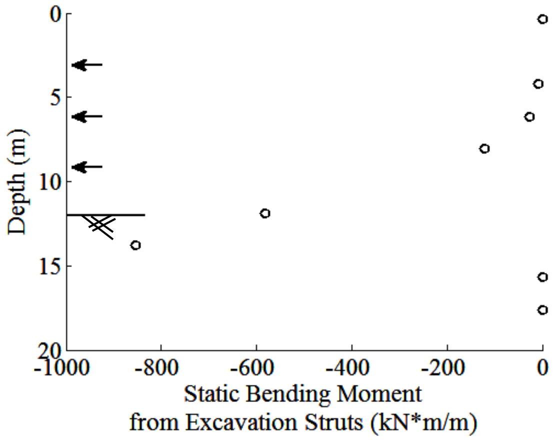

Figure 4-26. Static bending moments due to the strut axial loads on both excavation walls prior to the Northridge motion in E-No Bldg.

The calculated static bending moment profile from excavation strut loads (Fig. 4-26) was then subtracted from the total static moment profile obtained from bending strain gauges (Fig. 4-25), in order to calculate moments only due to static earth pressures, as shown in Figure 4-27.

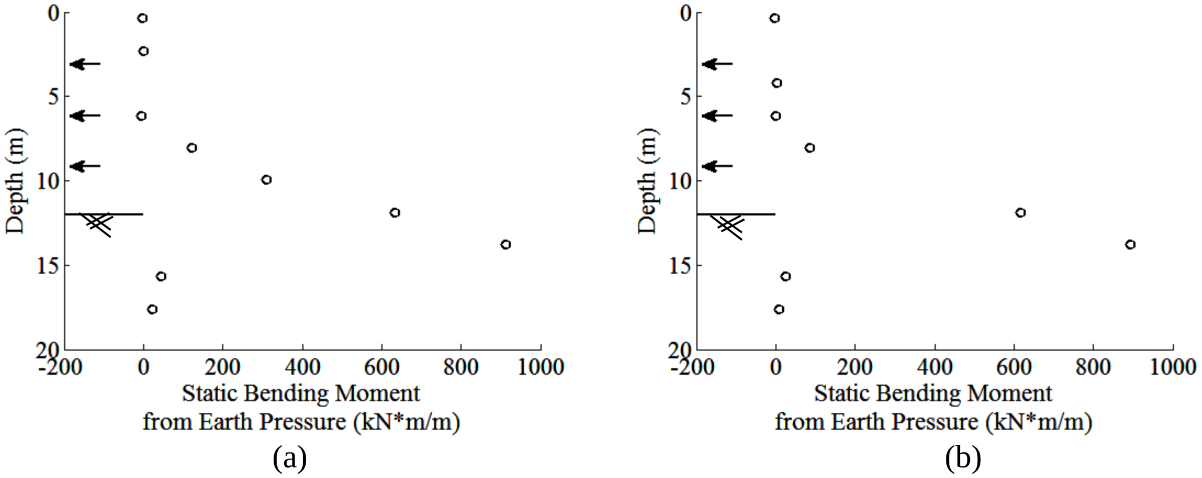

Figure 4-27. Static bending moment just from earth pressure (after accounting for the bending moment from struts) along: (a) the south wall and (b) the north wall of the temporary excavation prior to the Northridge motion in E-No Bldg.

The bending moment profiles are differentiated twice with respect to the depth of the wall to calculate the static pressure profiles in Figure 4-28. The profiles were not fit with polynomials and differentiated because the order of the fitted polynomial would determine an order of the pressure profile. Instead, the differentiation was performed numerically by taking the slope between two points. Caution was taken in using this method because accumulated error was known to be a possibility. Note that small negative pressures can sometimes be observed when using this method.

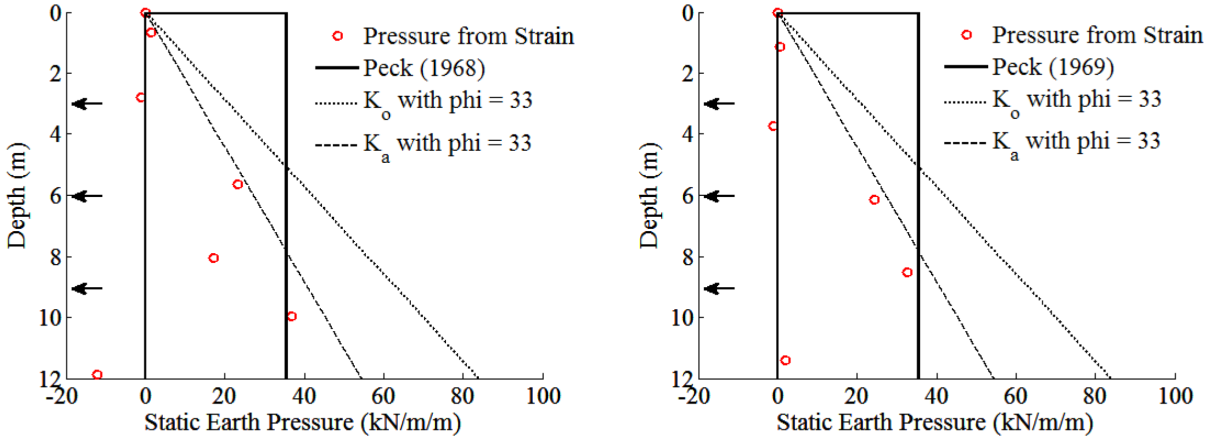

(a) (b)

Figure 4-28. Static earth pressures along: (a) the south wall, and (b) the north wall of the temporary excavation prior to the Northridge motion in E-No Bldg as compared to Peck (1969) apparent earth pressure diagram and the at-rest and active earth pressure profiles.

Static earth pressures obtained from strain gauges were small at the top of the excavation walls and increased with depth up to the depth of the lowest strut (9m), after which they appeared to decrease. This decrease in pressure toward the bottom of the excavation was consistent with tactile pressure measurements. The largest static pressures were observed at the depth of the bottom strut both from strain gauge and tactile sensor measurements. The static pressure profiles obtained from strain gauges were generally smaller than the theoretical active condition.

Dynamically, the bending moment along the excavation wall was caused by seismic lateral earth pressures, dynamic strut axial forces, and wall inertia. An example of the total dynamic bending moment profiles obtained from bending strain gauges is shown in Figure 4-29 on each excavation wall at the time highlighted in the base acceleration time history, which corresponded to the time of maximum bending moment recorded on the corresponding wall.

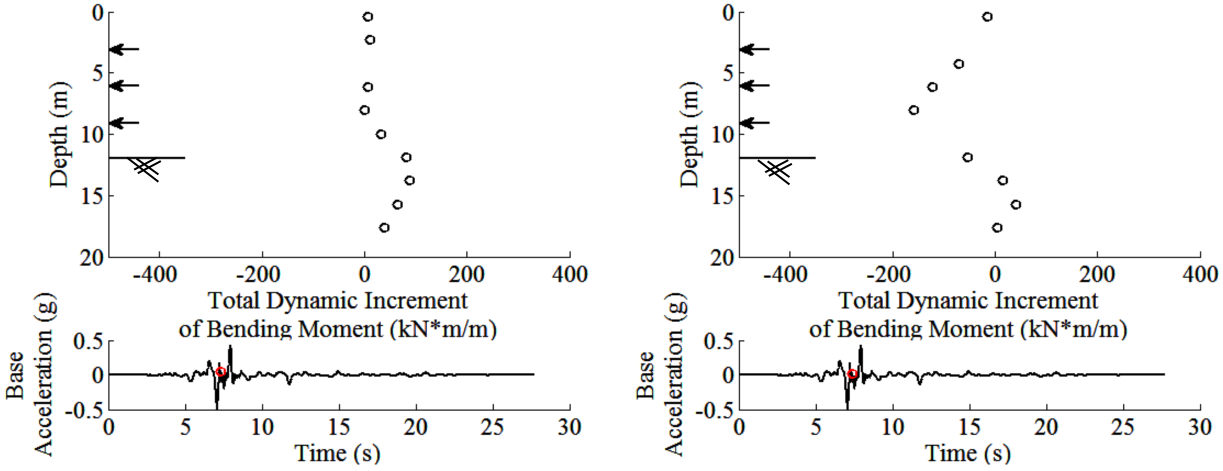

(a) (b)

Figure 4-29. Dynamic increment of bending moments along: (a) the south wall and (b) the north wall of the temporary excavation at the time of maximum bending moment on each wall during the Northridge motion in E-No Bldg.

The bending moment caused by wall inertia was estimated from the accelerometer recordings along the height of each excavation wall. The process to estimate the bending moment caused by wall inertia was adopted by Al Atik (2008). The inertial force profile along the excavation wall was calculated by the equation below.

$$f_I(z,t) = -m * A^t(z,t) \qquad \text{(Eq. 4-14)}$$

where

- $f_I(z,t)$ = inertial force at instant t and location z on the wall
- m = mass of the wall per unit height
- $A^t(z,t)$ = total acceleration at depth z and time t on the wall

Instead of using a limited number of accelerometers at the top and bottom of the wall and assigning a mode shape to the wall deformation (as done by Al Atik, 2008), all the accelerometers along the walls were used directly at each time to calculate the inertial force. The bending moment profile caused by wall inertia at each time was approximated by double integrating the inertial force profile with respect to the depth of the wall. Figure 4-30 shows an example of the bending moment profile caused by wall inertia during the Northridge motion in E-No Bldg at the time of maximum bending moment recorded on each wall.

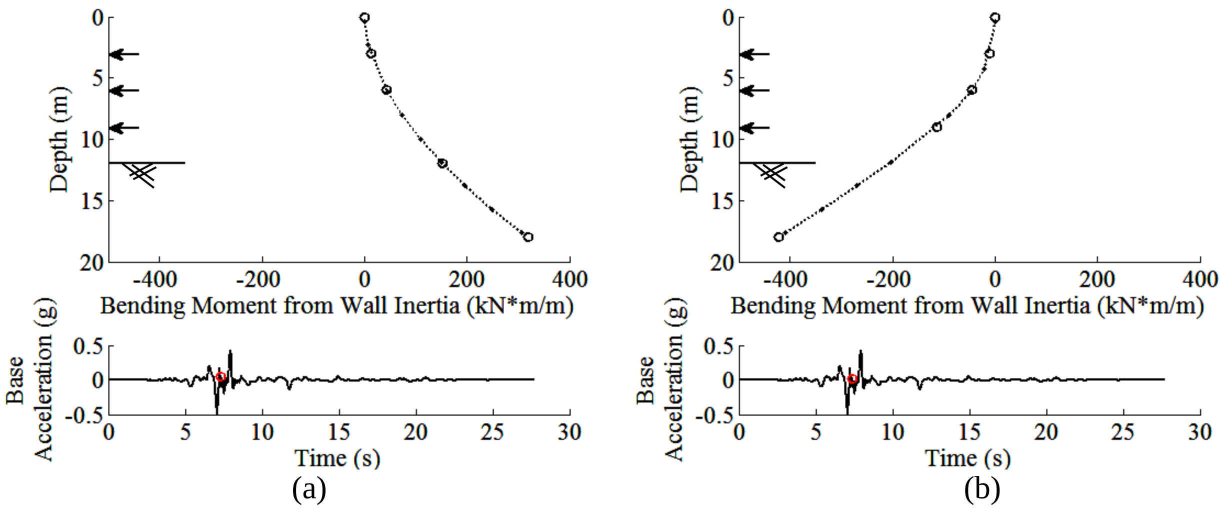

Figure 4-30. Dynamic bending moments due to wall inertia estimated from accelerometer recordings on: (a) the south wall, and (b) the north wall of the excavation at the time of maximum bending moment during the Northridge motion in E-No Bldg.

The bending moment from strut forces was estimated at every time step during shaking through a similar process as the static case. The assumed depth of no rotation was chosen at each time step as the depth where the maximum bending moment occurred in the embedded portion of the wall. The forces measured in each strut at each time were considered to be distributed equally between the two excavation walls, and the dynamic bending moment from excavation struts at each time step was estimated. An example is shown in Figure 4-31 of this profile.

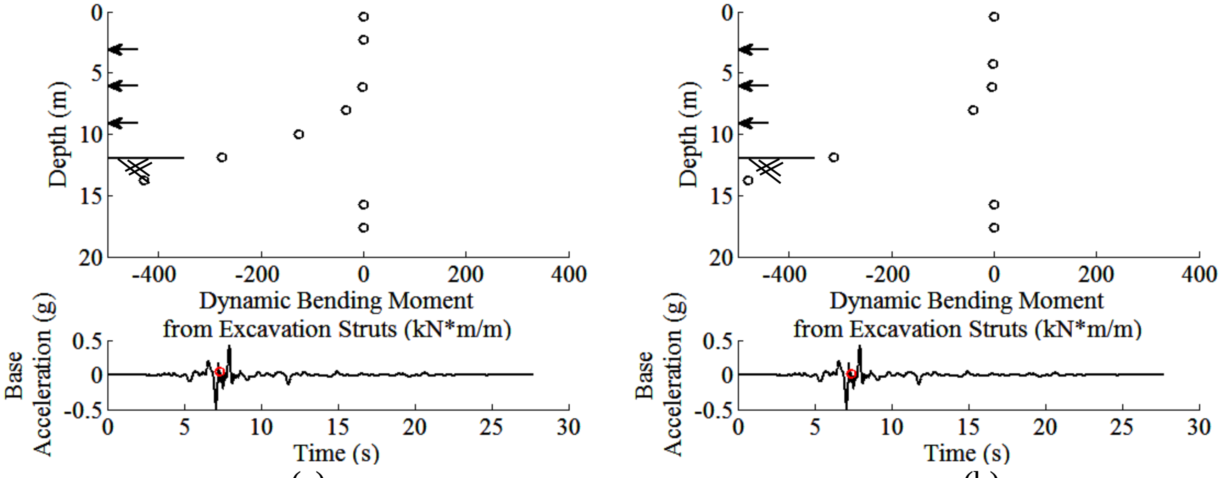

(a) (b)

Figure 4-31. Dynamic bending moments from the excavation struts on: (a) the south wall, and (b) the north wall of the excavation at the time of maximum bending moment during the Northridge motion of E-No Bldg.

The estimated dynamic bending moment profiles obtained from strut forces and wall inertia were subtracted from the total dynamic bending moments to obtain a moment profile only caused by earth pressures. These moment profiles are shown in Figure 4-32 at the time of maximum moment recorded on each wall during Northridge in E-No Bldg.

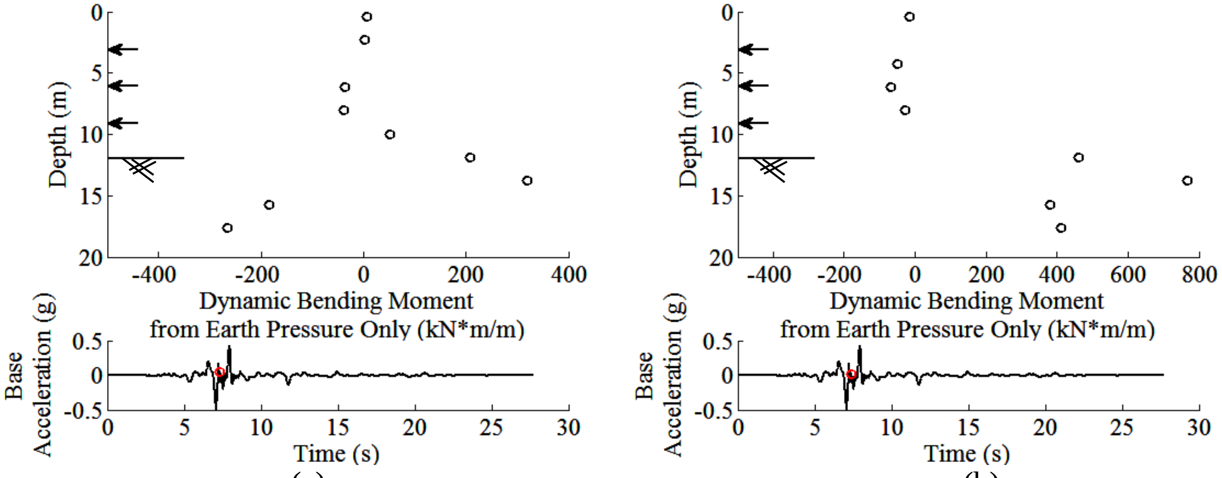

(a) (b)

Figure 4-32. Dynamic bending moments induced by lateral earth pressure only (after accounting for wall inertia and strut loads) on: (a) the south wall, and (b) the north wall of the excavation at the time of maximum moment during the Northridge motion in E-No Bldg.

These bending moment profiles shown in Figure 4-32 where then double differentiated numerically to obtain the dynamic increment of pressure profiles shown in Figure 4-33. The dynamic pressure profiles back calculated from strain gauges are compared in this figure with Rankine's active and at-rest linear static profiles and Peck's apparent earth pressure profile for braced excavations in sand.

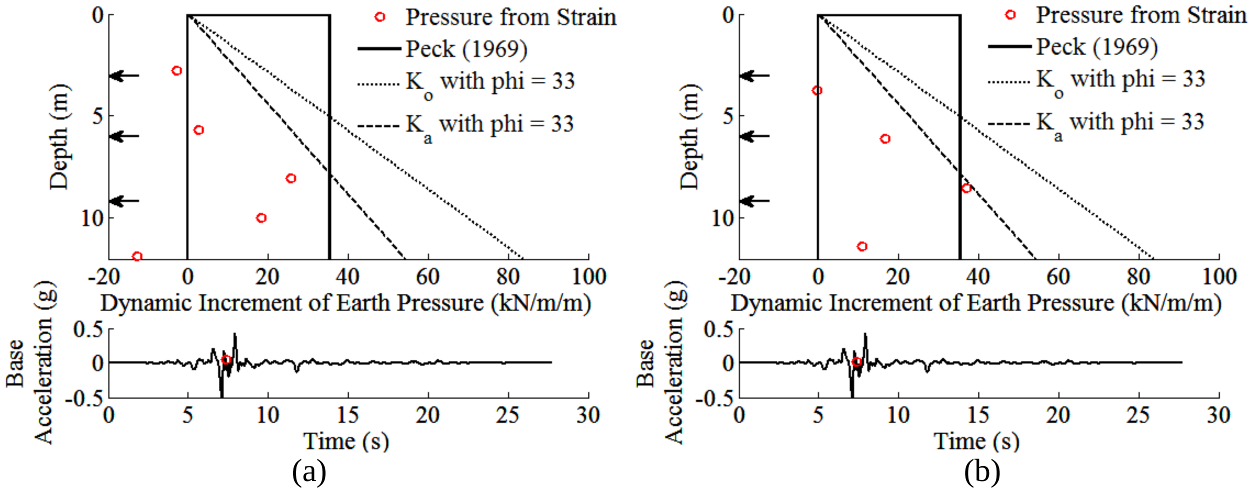

Figure 4-33. Dynamic increment of earth pressure computed from strain gauges on: (a) the south wall, and (b) the north wall of the excavation at the time of maximum moment measured during the Northridge motion in E-No Bldg as compared to Peck (1969) apparent earth pressure diagram and the at-rest and active earth pressure profiles.

These figures have presented an example calculation to obtain the dynamic pressure profile at one instance of time. This process was repeated for each time step, and similar to the tactile pressure sensors, a dynamic thrust was calculated from the dynamic pressure profiles through numerical integration. The next set of figures shows the dynamic thrust time histories on both walls of the excavation during E-No Bldg and E-Highrise along with static pressure profiles before the shaking event and the dynamic increment of pressure profiles at the time of maximum thrust on each wall. Each figure summarizes the lateral earth pressures obtained from strain gauges, and four different motions are shown in Figures 4-34 through 4-37.

Many of the same conclusions can be made from these summary plots as were made from the measurements by the tactile pressure sensors. In both E-No Bldg and E-Highrise, the dynamic thrust on the South/Bldg Wall and North/Open Wall were similar. This observation was expected for the case of E-No Bldg where the loading condition was symmetric. However, it was expected that the dynamic thrust would be slightly greater on the South/Bldg Wall based on tactile sensor recordings. The dynamic thrust time histories from strain gauges showed that the walls were loaded almost equally during E-No Bldg and E-Highrise. Importantly, the presence of a tall building amplified the dynamic thrust on both walls of the excavation. This was consistent with tactile sensor recordings (Figures 4-21 through 4-23).

In addition to the method described above, lateral earth pressures were also indirectly obtained by distributing the axial strut forces over the tributary area of that strut on the wall. This method assumes that the earth pressures were fully translated into the struts. This simplifying assumption provided another method to estimate lateral earth pressures and a simple comparison to the other methods.

The excavation struts were placed at depths of 3, 6, and 9 m and spaced 4.2 m apart laterally (into page). The force acting on the top strut, for example, was assumed to act over its tributary area (e.g., $\text{Area}_{\text{trib}}$ = [3m + 3m/2]*4.2m). The axial force measured on the top strut was divided by two to account for equal exertion on both excavation walls and then by this tributary area to calculate the earth pressure on the wall over the top 4.5 m. A similar process was repeated for the other struts, and static and dynamic pressure profiles with a stair-step shape were estimated from strut loads. This method estimated equal pressure profiles on both excavation walls statically and dynamically because of the inherent assumptions.

Figures 4-38 through 4-41 show the dynamic thrust time histories as calculated by strut loads as well as the static and total (i.e., static + dynamic) pressure profiles on the two walls. The static pressures were measured before the event and total pressures are presented at the time of maximum thrust, indicated in the thrust time history.

During E-No Bldg and E-Highrise the top strut experienced a decrease in load statically after each motion. Dynamically, the top strut measured compression, especially apparent in E-Highrise. In between shakes, the top strut showed approximately zero loads in both E-No Bldg and E-Highrise, and the bottom strut measured an increase in static loads between shakes. The excavation walls experienced a small degree of permanent racking (evident in direct displacement measurements) after each earthquake event that slightly increased the distance between the walls toward the top of the excavation, leading to near zero static axial loads on the top struts. At the bottom of the excavation, the wall experienced permanent displacements inward into the excavation, which in turn increased static earth pressures at lower struts.

Figures 4-42 through 4-44 compare the dynamic thrust from the two strain gauge methods during three representative shaking events in E-No Bldg and E-Highrise both in terms of time histories and Fourier amplitude spectra. The first motion presented in Figure 4-42 is during the Northridge motion. Note that both walls are presented based on the first strain gauge method, but only one wall is presented for the second strut strain gauge method, because the latter assumes equal pressures on the two walls. The three measurements compared reasonably well in the time and frequency domains during E-No Bldg and E-Highrise.

The dynamic thrust time histories from the two strain gauge methods were similar to each other in both tests. The dynamic thrusts were also similar on the two excavation walls in E-No Bldg, but were slightly larger on the building side in E-Highrise. The difference was small, however. Importantly, all methods indicated an increase in dynamic earth pressures in E-Highrise compared to E-No Bldg, which was consistent with tactile sensor recordings. Further, both methods showed a permanent change in thrust (typically an increase in thrust) after each motion, which could not be observed from tactile sensor recordings due to the need for a band-pass filter when using those sensors.

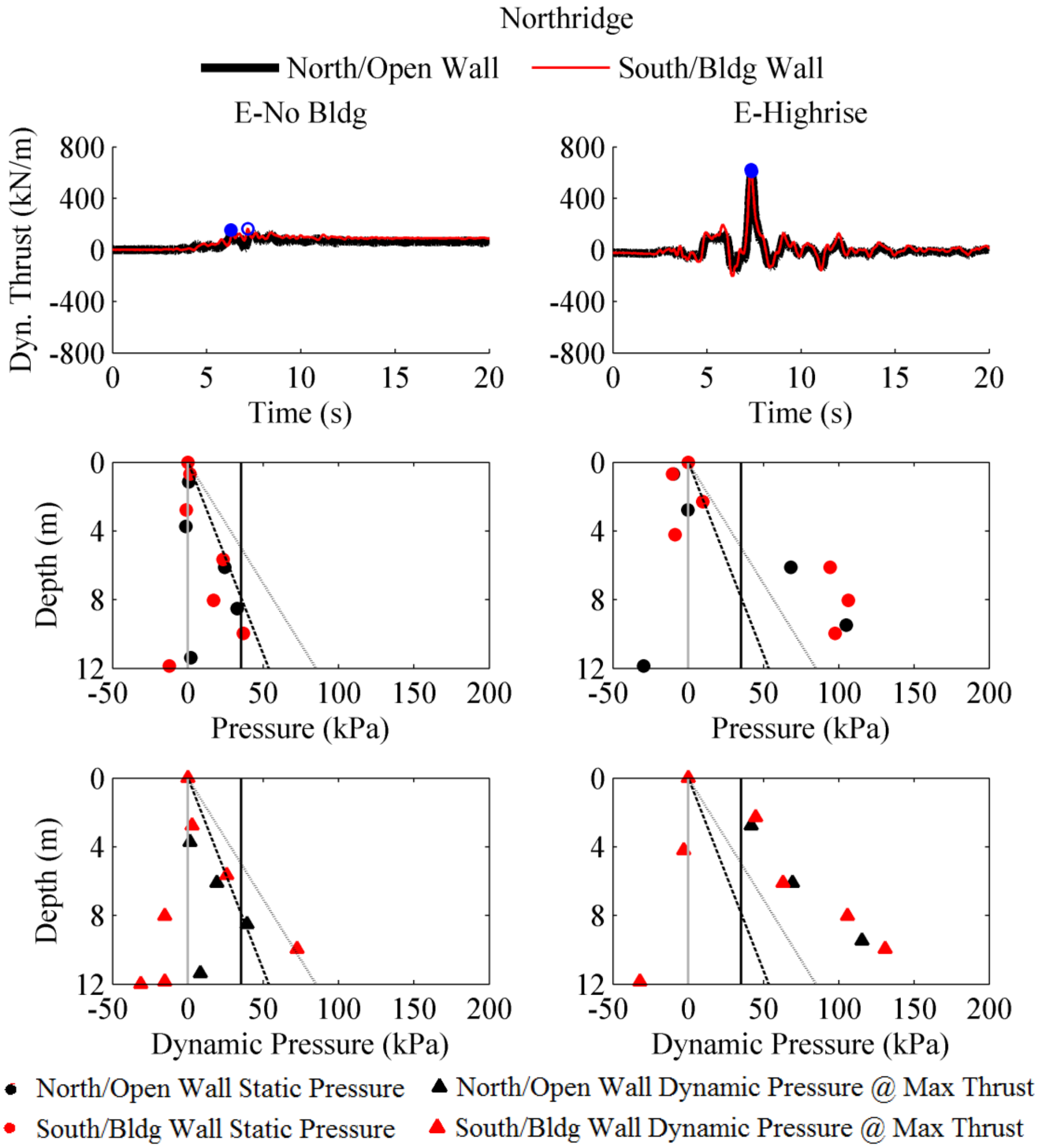

Figure 4-34. Dynamic thrust time histories as calculated from strain gauges on both excavation walls during Northridge in E-No Bldg and E-Highrise, and static and dynamic earth pressure profiles shown at the time of maximum thrust on each wall.

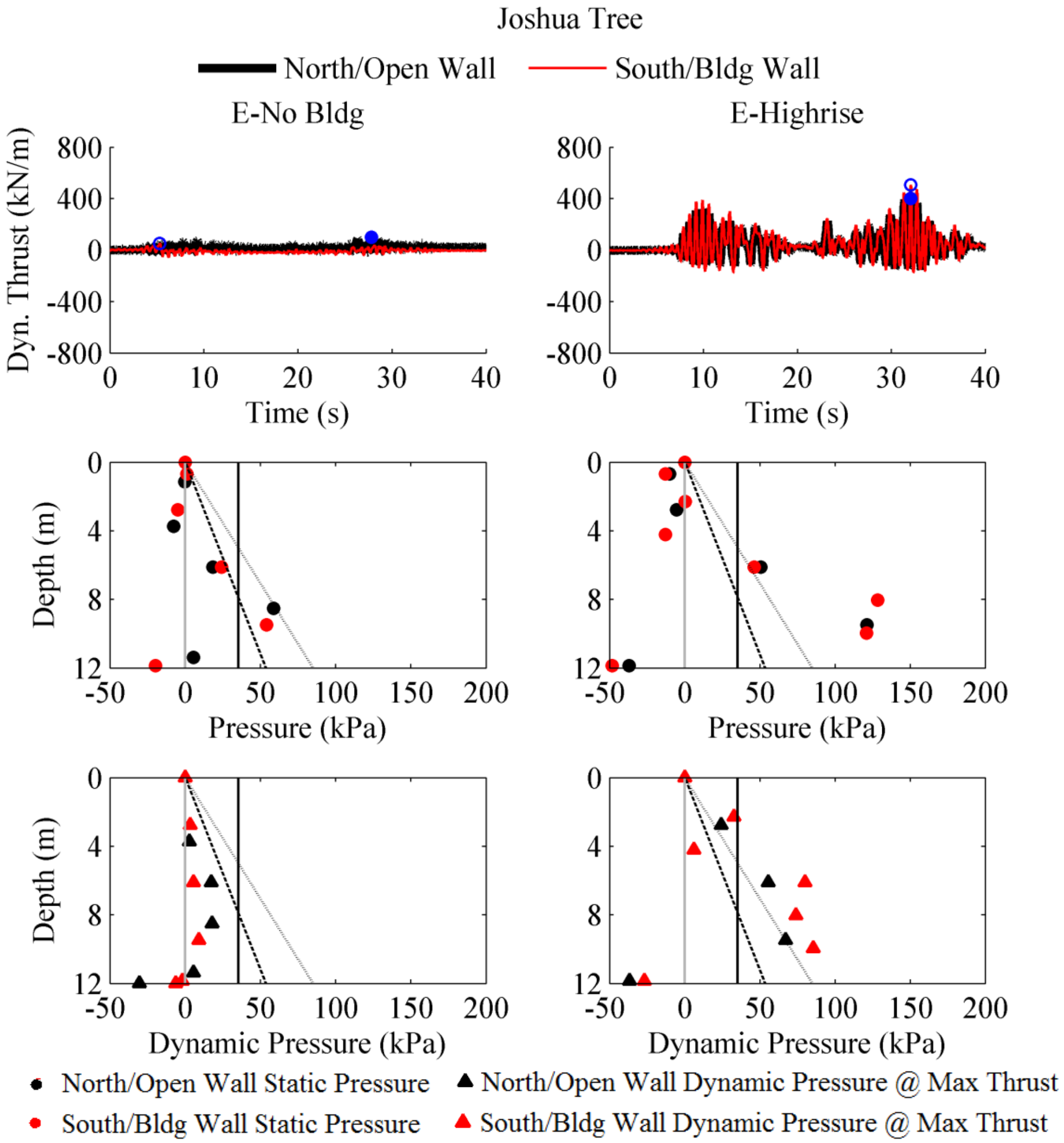

Figure 4-35. Dynamic thrust time histories as calculated from strain gauges on both excavation walls during Joshua Tree in E-No Bldg and E-Highrise, and static and dynamic earth pressure profiles shown at the time of maximum thrust on each wall.

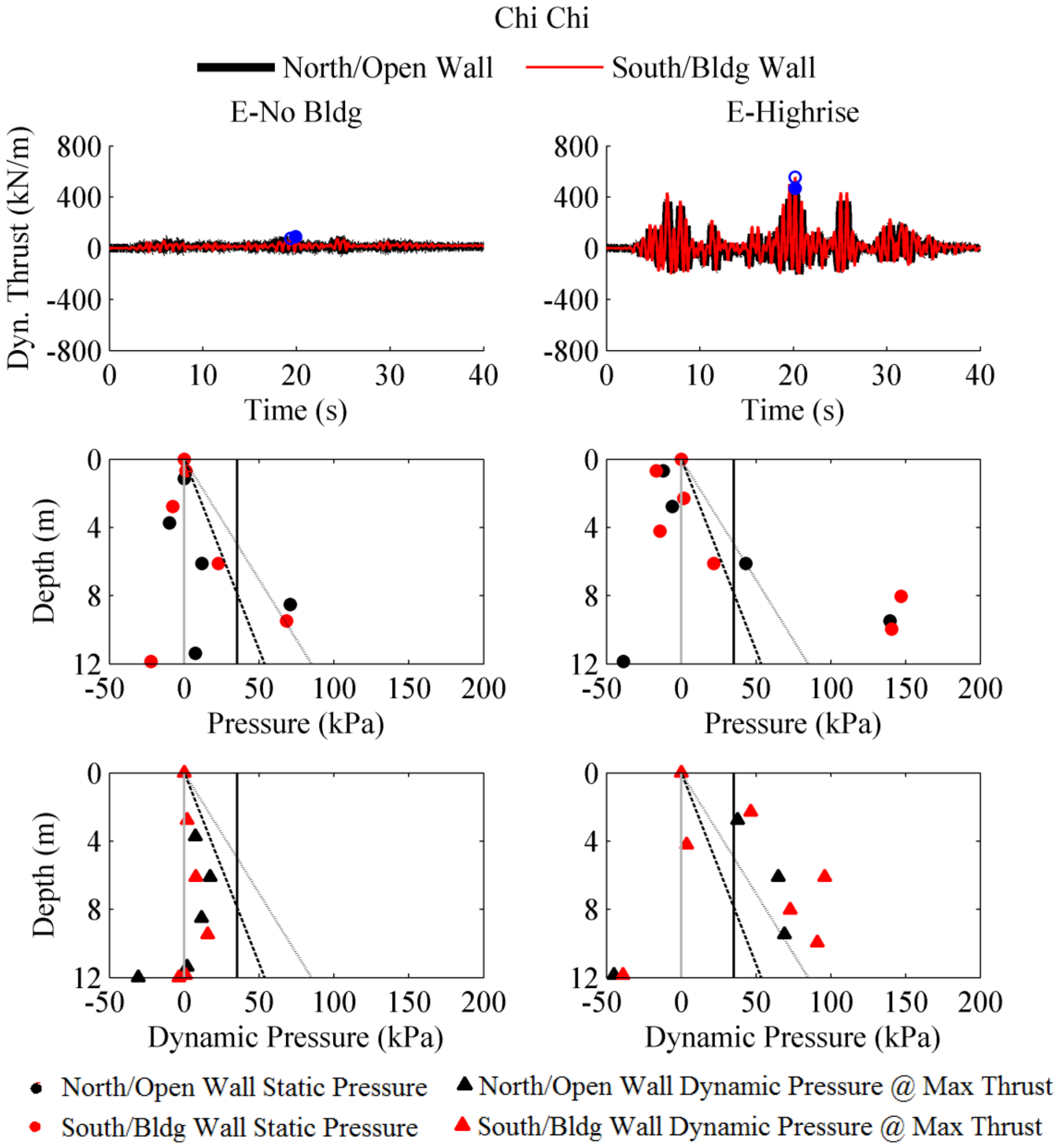

Figure 4-36. Dynamic thrust time histories as calculated from strain gauges on both excavation walls during Chi Chi in E-No Bldg and E-Highrise, and static and dynamic earth pressure profiles shown at the time of maximum thrust on each wall.

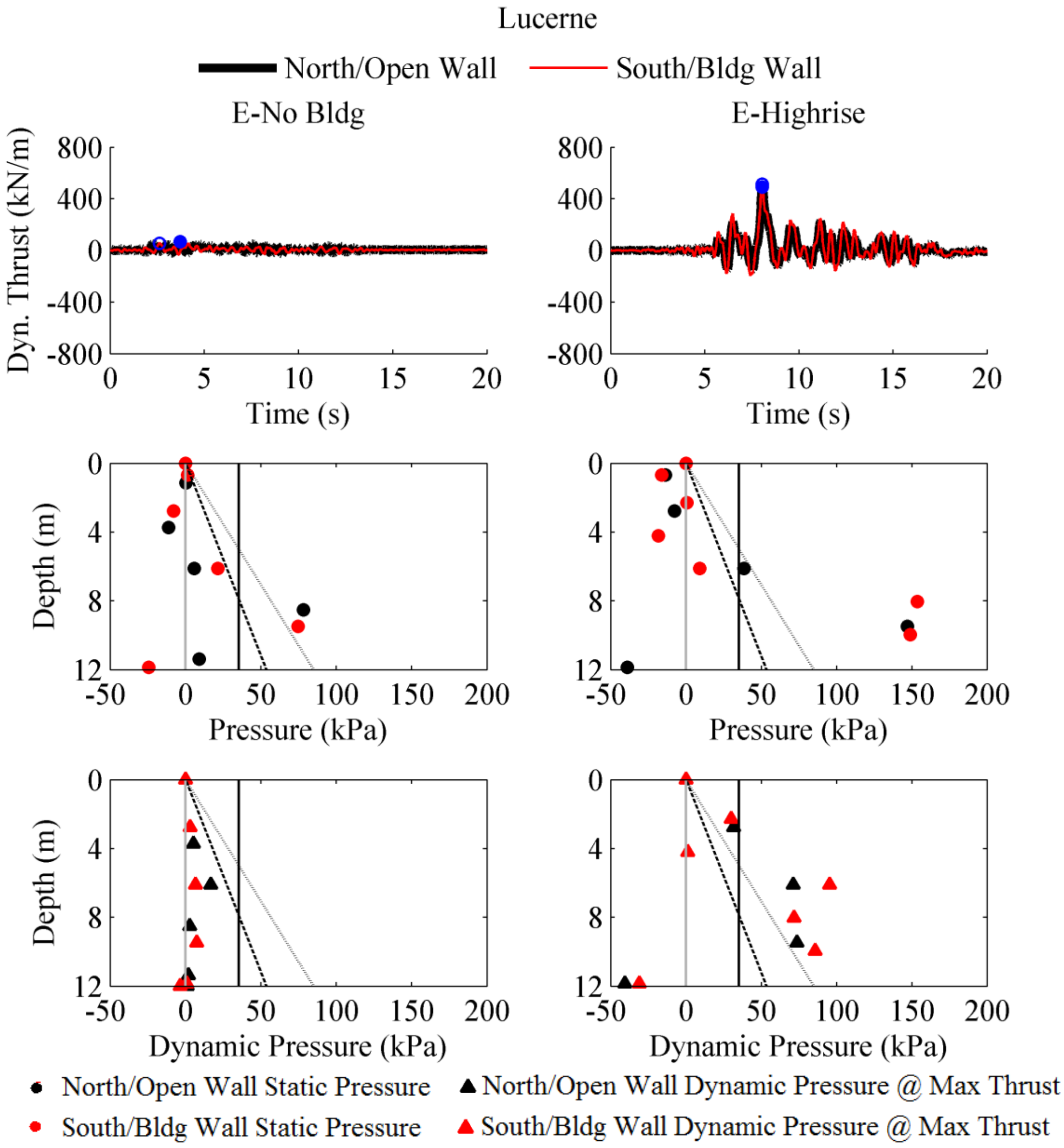

Figure 4-37. Dynamic thrust time histories as calculated from strain gauges on both excavation walls during Lucerne in E-No Bldg and E-Highrise, and static and dynamic earth pressure profiles shown at the time of maximum thrust on each wall.

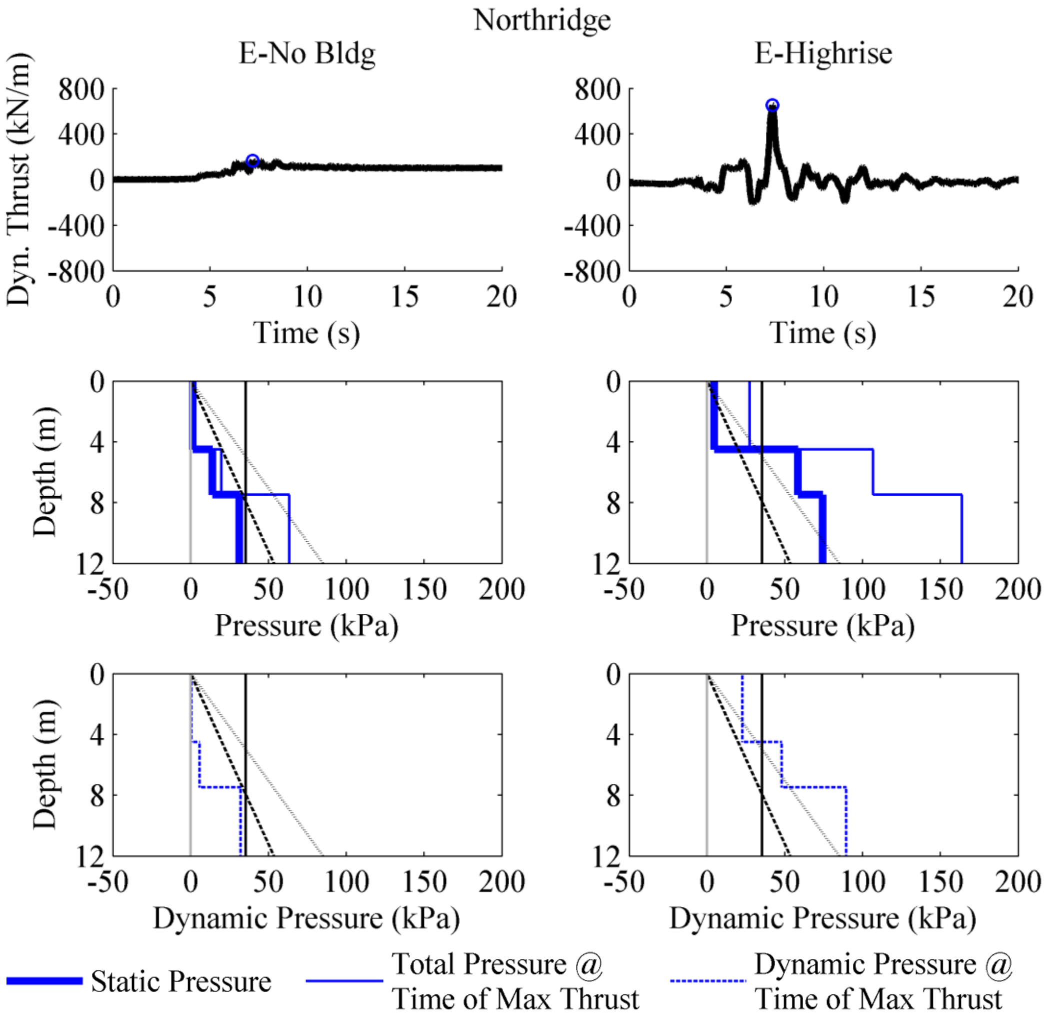

Figure 4-38. Dynamic thrust time histories calculated from strut loads during Northridge in E-No Bldg and E-Highrise, and static, total, and dynamic earth pressure profiles shown at the time of maximum thrust.

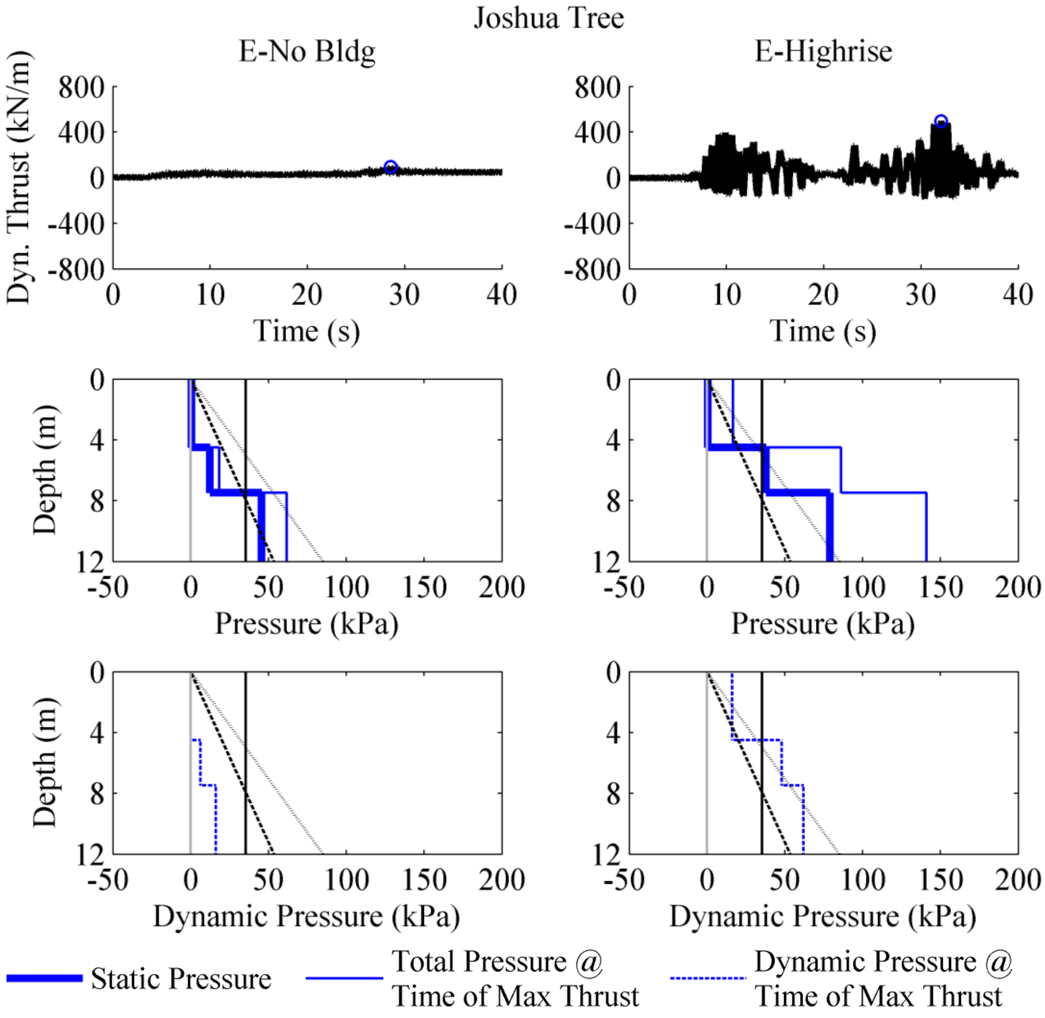

Figure 4-39. Dynamic thrust time histories calculated from strut loads during Joshua Tree in E-No Bldg and E-Highrise, and static, total, and dynamic earth pressure profiles shown at the time of maximum thrust.

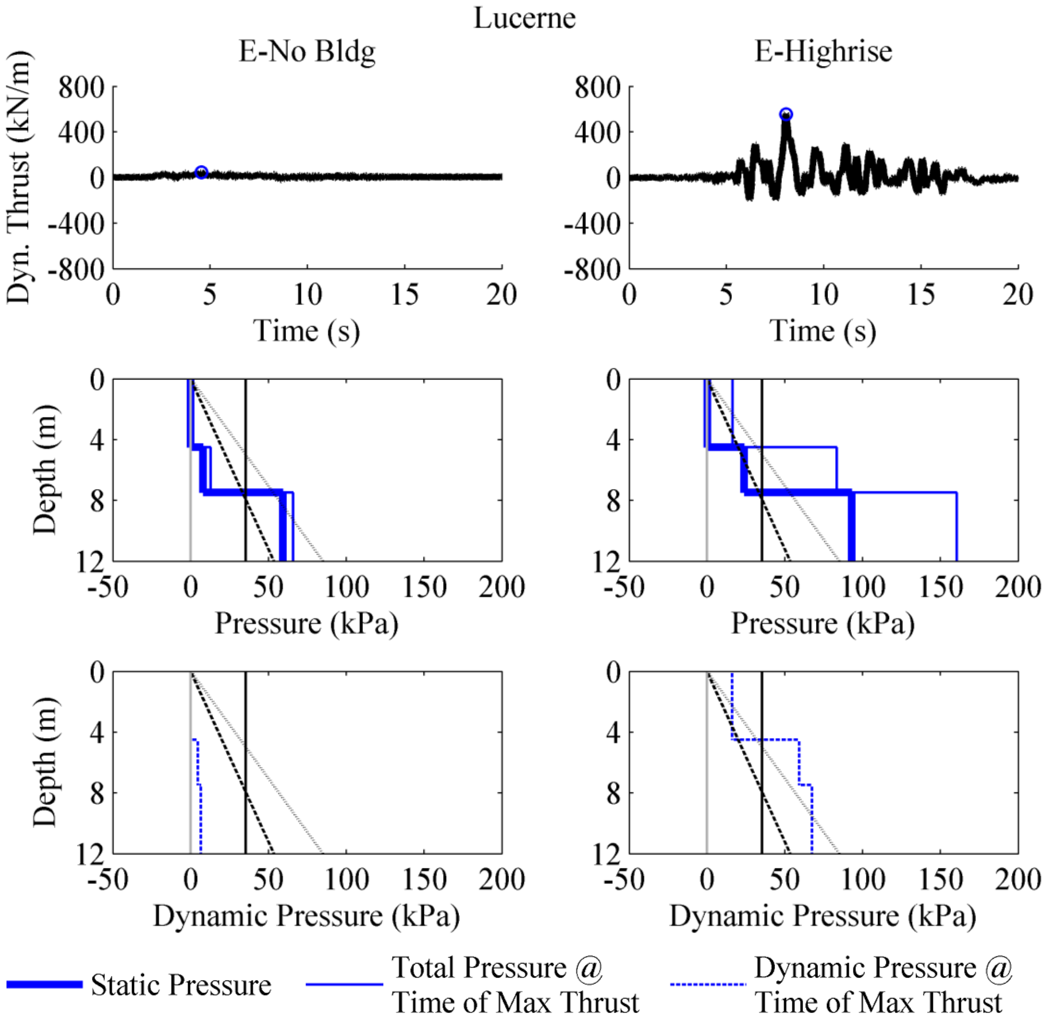

Figure 4-40. Dynamic thrust time histories calculated from strut loads during Lucerne in E-No Bldg and E-Highrise, and static, total, and dynamic earth pressure profiles shown at the time of maximum thrust.

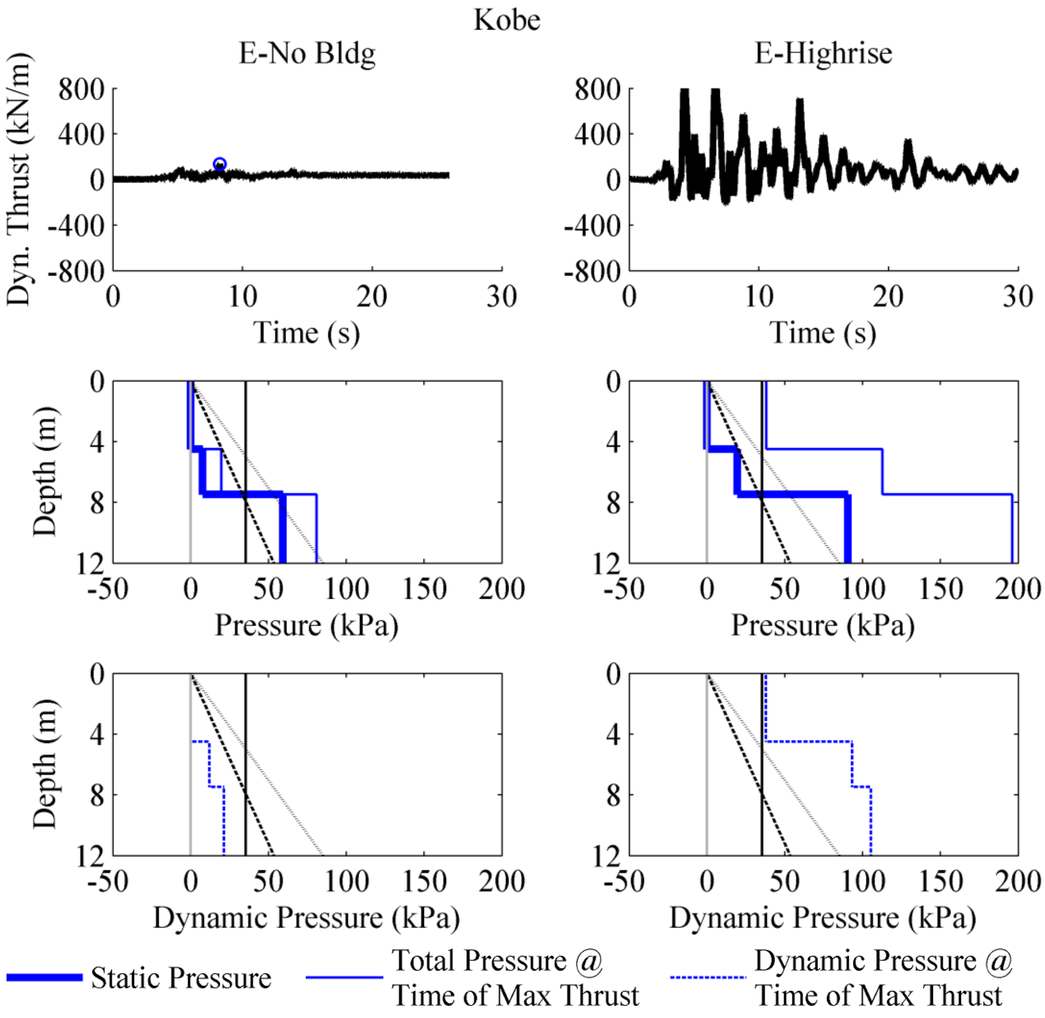

Figure 4-41. Dynamic thrust time histories calculated from strut loads during Kobe in E-No Bldg and E-Highrise, and static, total, and dynamic earth pressure profiles shown at the time of maximum thrust.

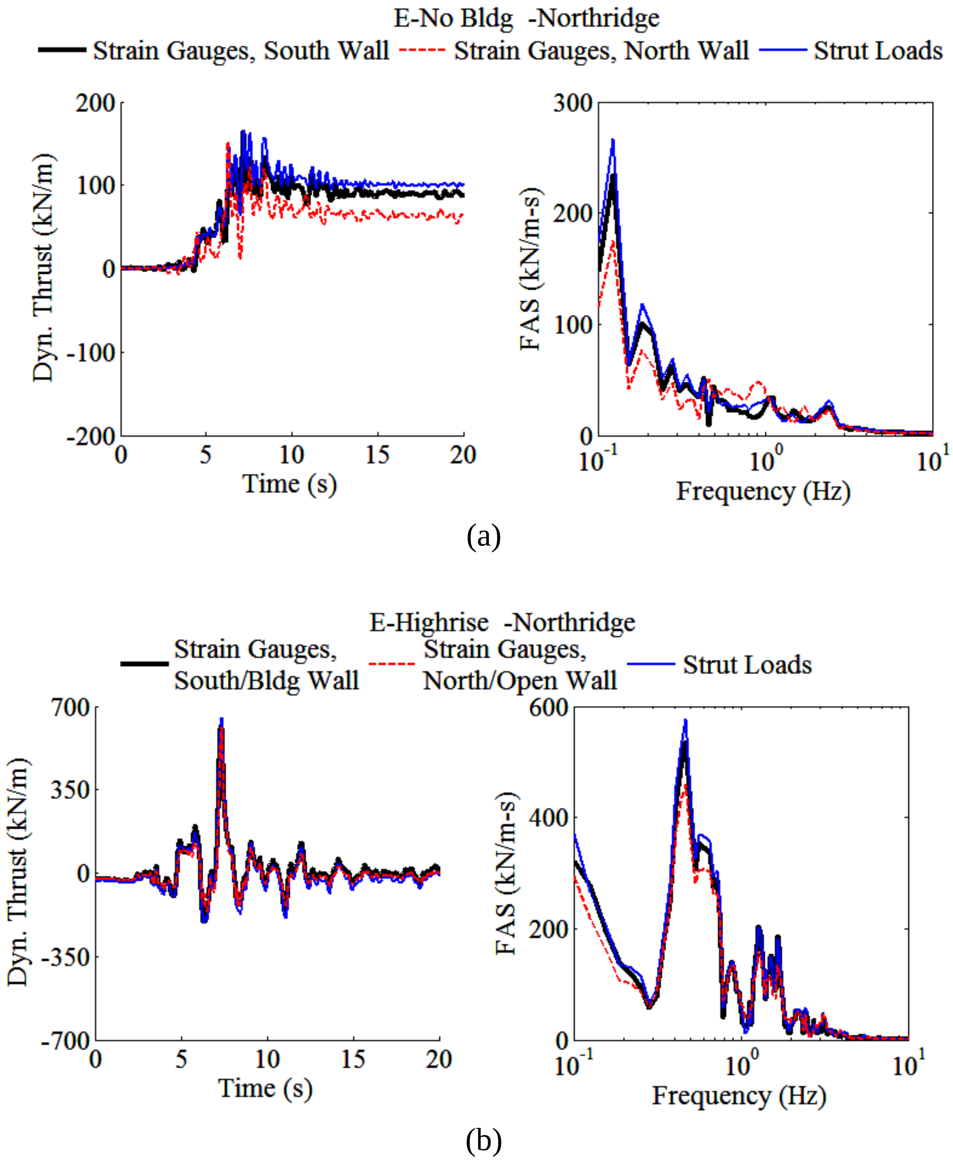

Figure 4-42. Dynamic thrust estimated from strain gauges on both excavation walls and from strut loads during Northridge in: (a) E-No Bldg, and (b) E-Highrise represented in the time and frequency domains.

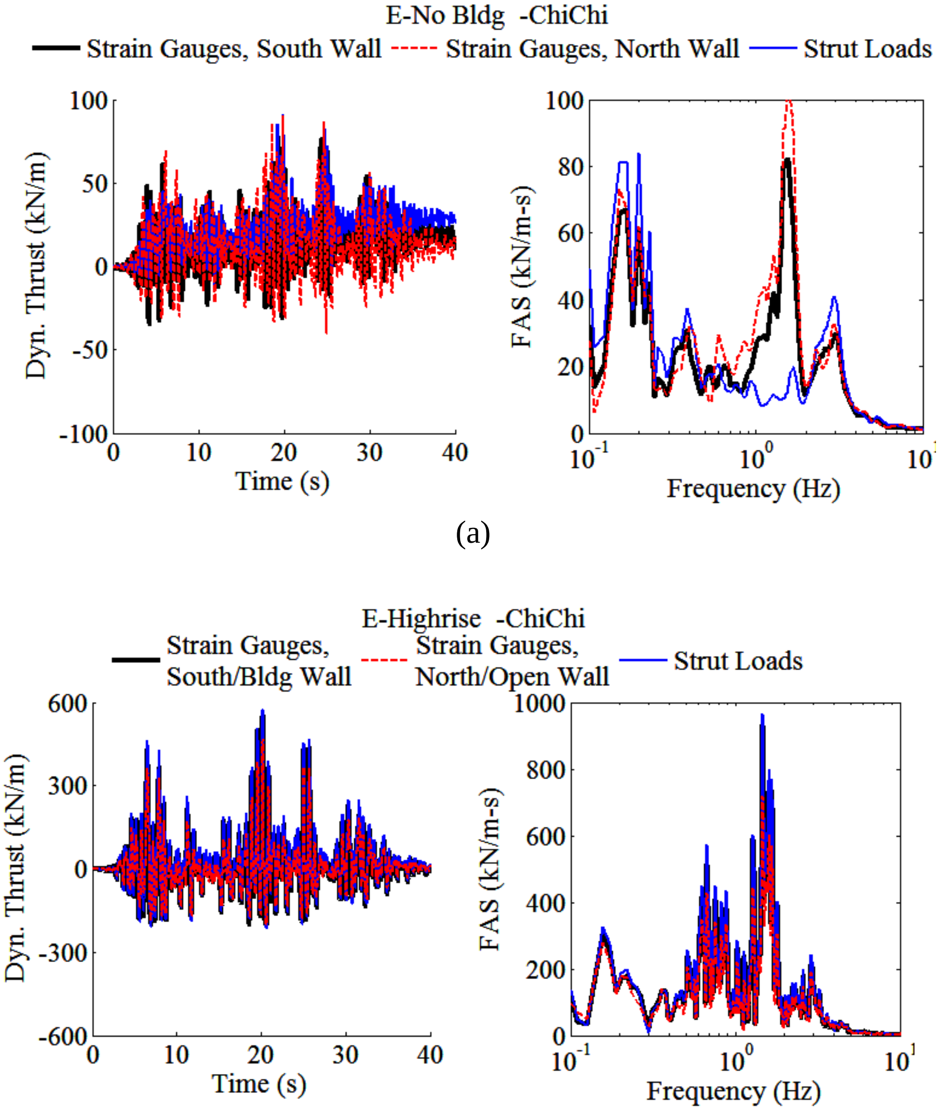

(a)

(b)

Figure 4-43. Dynamic thrust estimated from strain gauges on both excavation walls and from strut loads during Chi Chi in: (a) E-No Bldg, and (b) E-Highrise represented in the time and frequency domains.

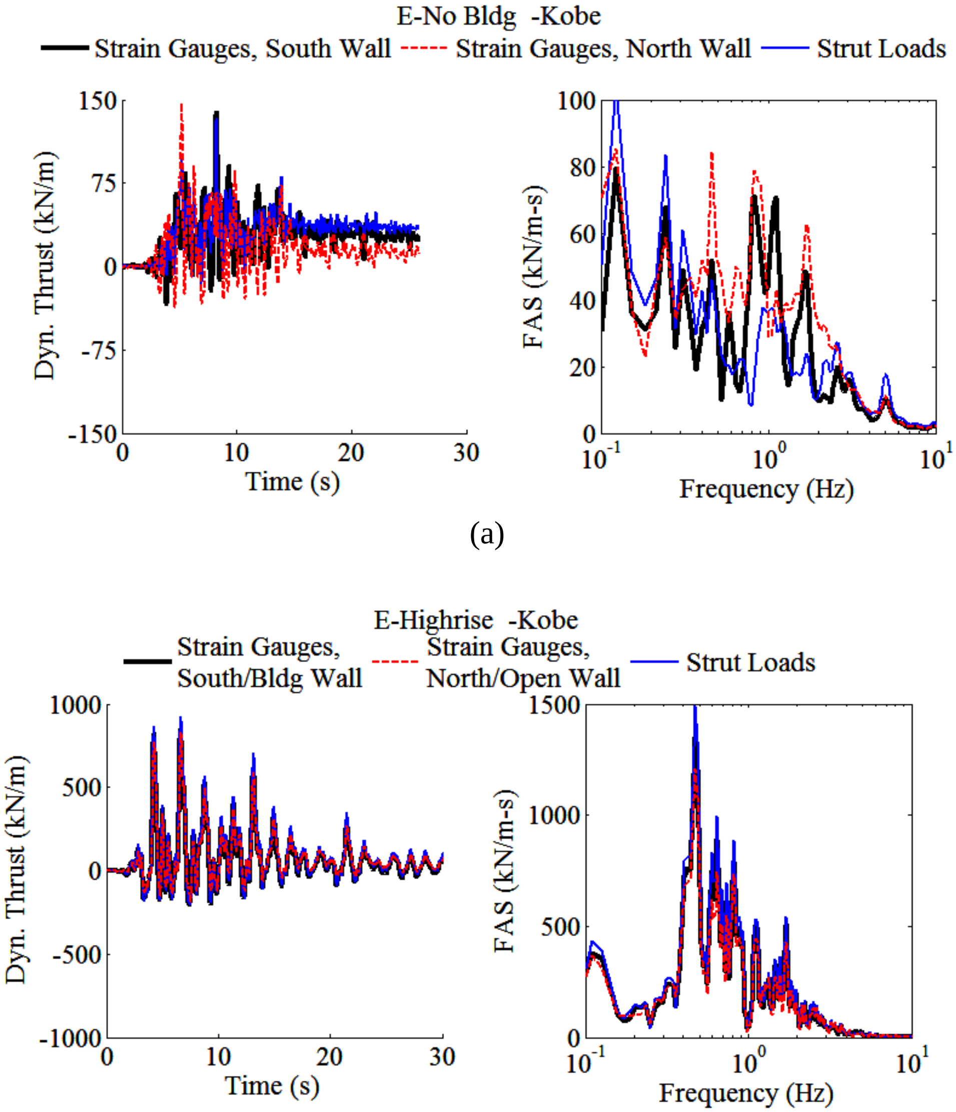

(a)

(b)

Figure 4-44. Dynamic thrust estimated from strain gauges on both excavation walls and from strut loads during Kobe in: (a) E-No Bldg, and (b) E-Highrise represented in the time and frequency domains.

4.4.3 Comparison of Methods

The three methods, one direct and two indirect, of obtaining lateral earth pressures and dynamic thrust discussed in previous sections are compared in this section. Both static measurements and dynamic lateral earth pressures in the form of dynamic thrust are compared among methods and the three excavation tests.

Figures 4-45 and 4-46 show the comparison of static lateral earth pressures measured by the three methods during E-No Bldg and E-Highrise, respectively. Both excavation walls are shown before two earthquake events during the tests. The profiles measured by the different methods are compared to Rankine's active and at-rest earth pressure profiles assuming a friction angle of 33^o and Peck's apparent earth pressure of a braced excavation in sand. During E-No Bldg, the tactile pressure sensor is shown on the North/Open Side only because the sensors on the South/Bldg side malfunctioned.

During E-No Bldg, the static lateral earth pressures measured before the Northridge motion, the first motion, were estimated reasonably well by Rankine's active pressure profile and Peck's apparent earth pressure that is assumed to be constant with depth. After multiple earthquake events, the static pressure profile changed as is seen in Figure 4-45(b), which shows the profiles before Lucerne, the fifth event in the series. These changes were due to changing soil conditions and permanent deformations experienced by the braced excavation. As discussed before, the top strut lost load while the bottom strut gained load throughout the earthquake events. Soil densification also increases the unit weight of soil and hence, the applied pressures on the wall.

Peck's apparent pressure diagram for a braced excavation in sand predicts a constant earth pressure with depth. This constant earth pressure with depth is meant to predict earth pressures at the top of the excavation because of the presence of a top strut holding the soil in place. It also accounts for the deformation shape of the braced excavation wall that relieves pressure below the bottom strut. The measured pressures from pressure sensors and strain gauges showed this decrease in earth pressure below the depth of the bottom strut (i.e., 9m). The pressure from strain gauges was able to capture the pressure at the bottom of the excavation, which was measured to be close to zero while the pressure sensors captured the initial decrease in pressure after a depth of 9m. Due to the simplifying assumptions behind the strut load method, this decrease in pressure below the bottom strut was not captured. However, overall, all three methods were roughly consistent in terms of static earth pressures.

Figure 4-46 shows a similar comparison of static earth pressures from the various methods during E-Highrise. Overall, similar observations can be made. The addition of the highrise building increased earth pressures on both walls of the excavation. Rankine and Peck's predicted profiles underestimated the static pressures experienced by the system, as was expected, but they are shown for ease of comparison. Overall, the three methods of estimating static earth pressures compared well to each other and showed expected trends.

The three methods of estimating earth pressures were also compared dynamically. Figures 4-47 through 4-49 compare the dynamic thrusts from the three methods during three representative motions in E-No Bldg. In order to compare all three methods, the thrust time histories were filtered using a 4th order Butterworth bandpass filter with corner frequencies of 0.1 and 5 Hz in all three methods. The recordings from the tactile pressure sensors are known to show a low frequency response at times that needed to be removed for comparison to other pressure measurements. Any permanent change in thrust was, as a result, removed from the time histories in this comparison, and only the transient thrust is considered. For the case of E-No Bldg, the tactile pressure sensor recording on the north wall was taken to be the same on the south wall assuming symmetry. Overall, the three methods compared well, given all the uncertainties in the process of estimating dynamic earth pressures in the high frequency environment of the centrifuge. However, the dynamic thrusts measured by the pressure sensors were observed to be slightly greater than those measured by the strain gauges or strut loads in E-No Bldg.

The same comparisons were made during E-Highrise. As discussed earlier, the tactile pressure sensor on the South/Bldg Wall was a high capacity sensor, and dynamic recordings were faulty due to a very low SNR. Because dynamic thrust obtained from strain gauges showed similar thrusts on both excavation walls in E-Highrise, the recordings from the tactile sensors were also assumed to be similar on the two walls in E-Highrise for the purpose of comparing the three different methods in Figures 4-50 through 4-51. Filtering of the dynamic thrust time histories was performed to compare the three methods under similar conditions. The dynamic thrust obtained from the three methods in E-Highise compared well, similar to E-No Bldg. These comparisons provided more confidence in using the recordings from any of these procedures when evaluating the dynamic forces acting on an underground structure in centrifuge (more so than for static earth pressures).

In addition to the amplitude of dynamic earth pressures, it is important to evaluate their distribution and centroid, which translate into bending moment calculations in design. Figure 4-53 summarizes the depth to the centroid of dynamic earth pressures along both excavation walls. The dynamic earth pressures were obtained from tactile sensors and bending strain gauges on each wall, experiment, and ground motion, at the time corresponding to maximum thrust, and the centroid of the pressure was estimated. The results are plotted against the PGA of the base motion. The different colors represent the three centrifuge tests, the different shapes represent the two different walls, and the solid versus empty symbols represents the two methods of measuring thrust. The height of the wall is taken as the height above the base of excavation (i.e., 12m)

The centroid of the dynamic pressure profile was located between a depth to height (D/H) ratio of 0.5 to 0.8. In general, in most cases, the presence of the adjacent building moved the location of dynamic thrust up along the wall (closer to the soil surface). Further, the location of the dynamic thrust was estimated to be lower on the wall when using tactile sensors compared to strain gauges. There was no clear pattern between the location of thrust and the intensity of shaking in these experiments.

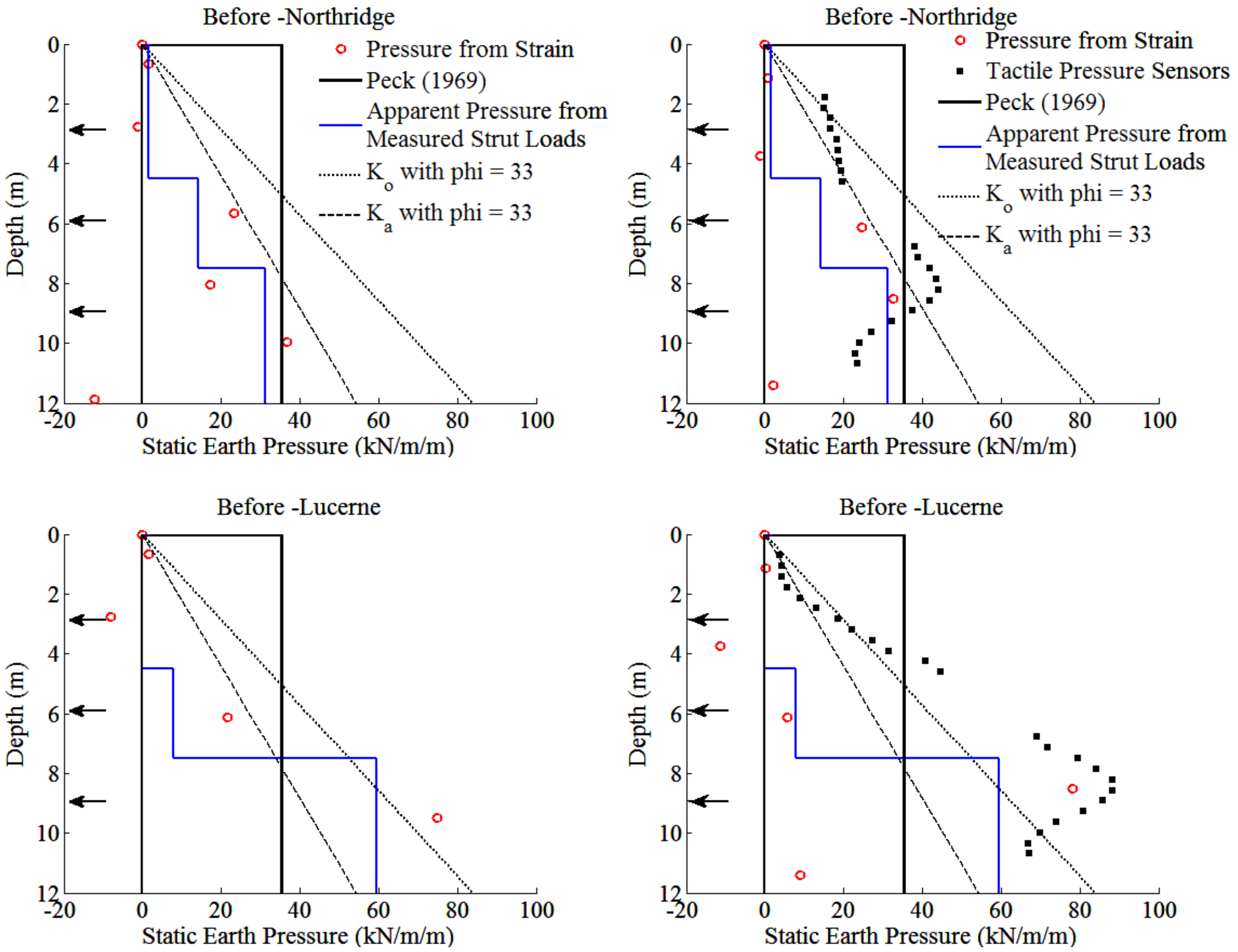

(a) (b)

Figure 4-45. Static earth pressure profiles measured on: (a) the south wall, and (b) the north wall of the excavation by three methods: directly measured with tactile pressure sensors, obtained from bending strain gauges, and from axial strut loads. The profiles shown before two motions in E-No Bldg.

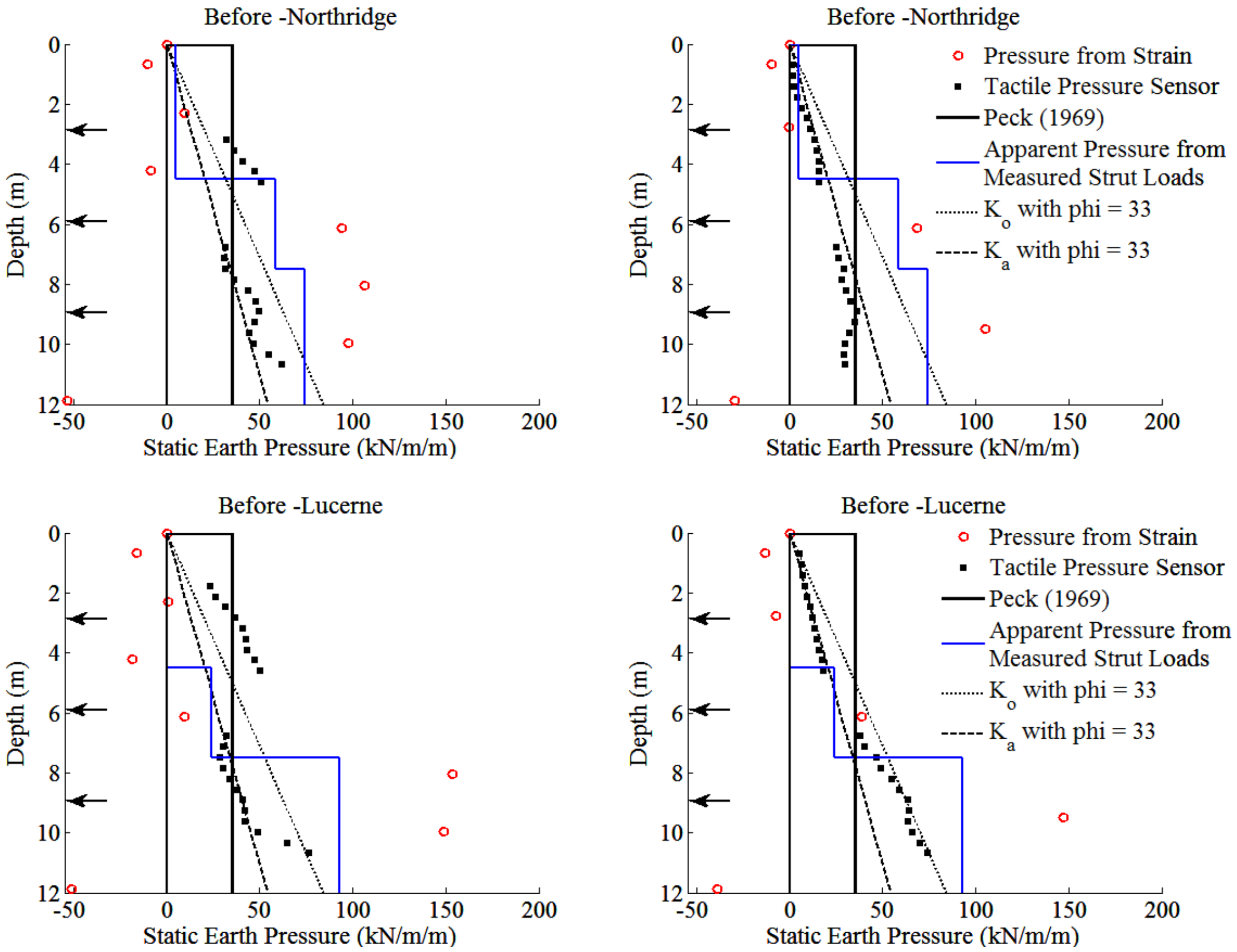

(a) (b)

Figure 4-46. Static earth pressure profiles measured on: (a) the south wall, and (b) the north wall of the excavation by three methods: directly measured with tactile pressure sensors, obtained from bending strain gauges, and from axial strut loads. The profiles shown before two motions in E-Highrise.

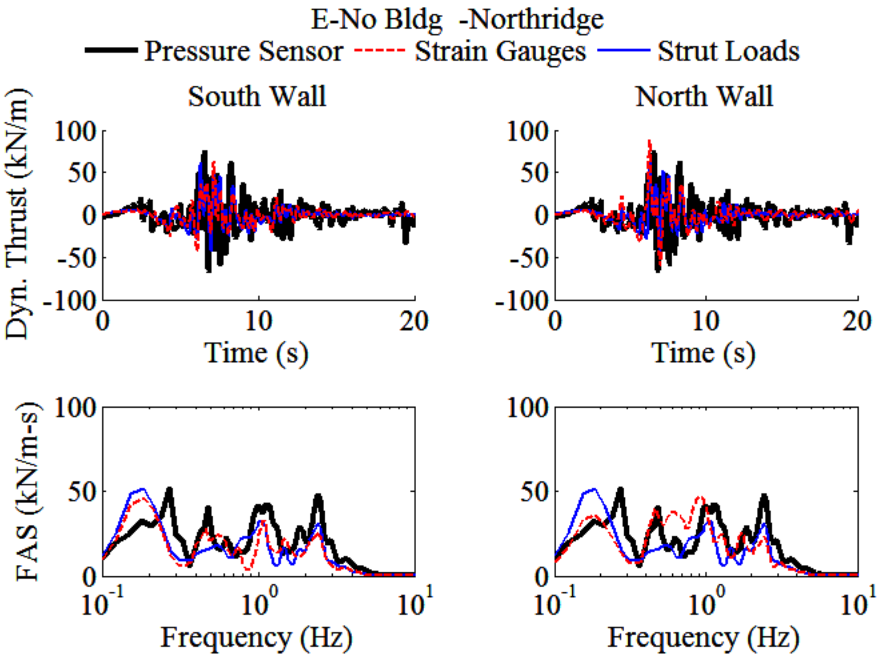

Figure 4-47. Dynamic thrust estimated from pressure sensors, strain gauges, and strut loads shown on both excavation walls during Northridge in E-No Bldg represented in the time and frequency domains.

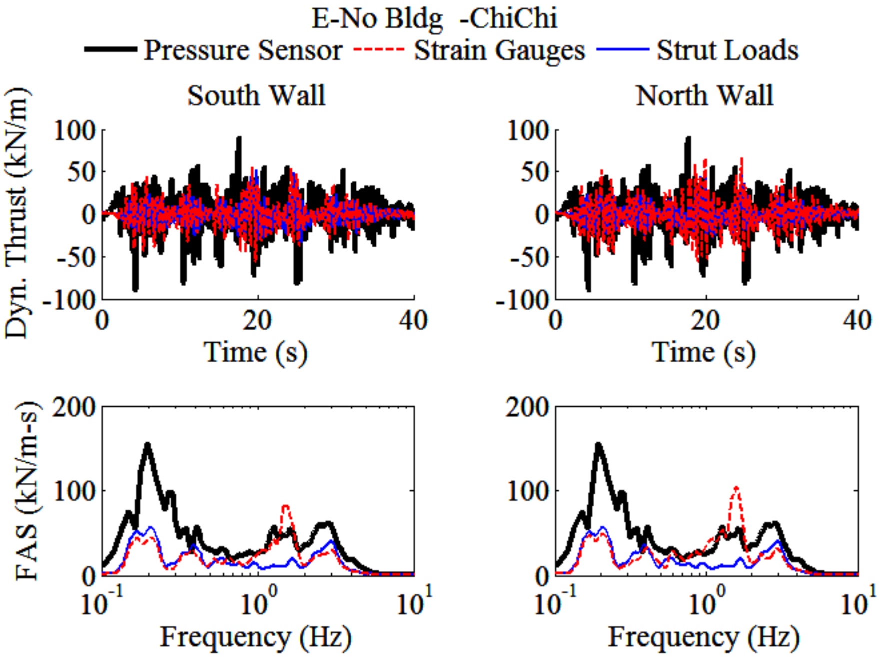

Figure 4-48. Dynamic thrust estimated from pressure sensors, strain gauges, and strut loads shown on both excavation walls during Chi Chi in E-No Bldg represented in the time and frequency domains.

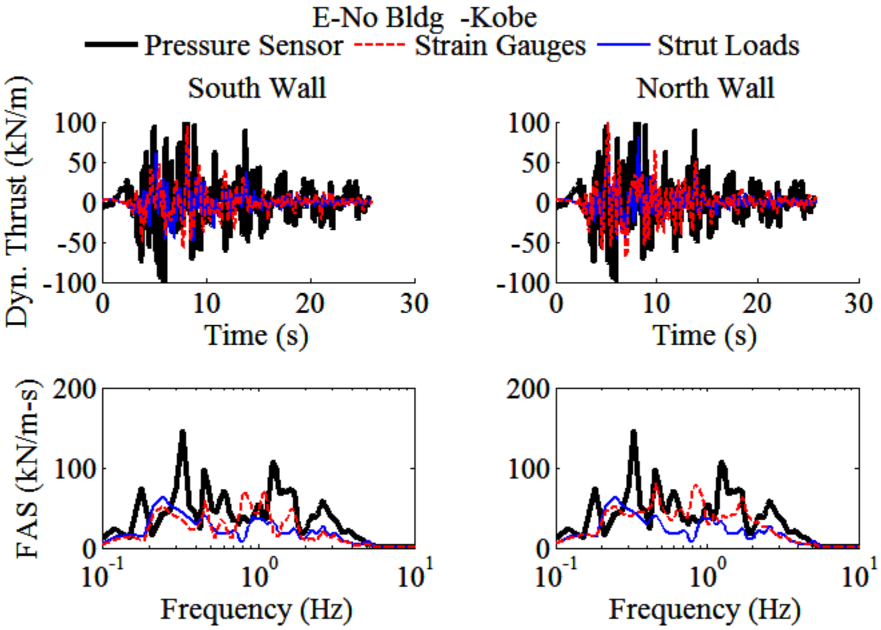

Figure 4-49. Dynamic thrust estimated from pressure sensors, strain gauges, and strut loads shown on both excavation walls during Kobe in E-No Bldg represented in the time and frequency domains.

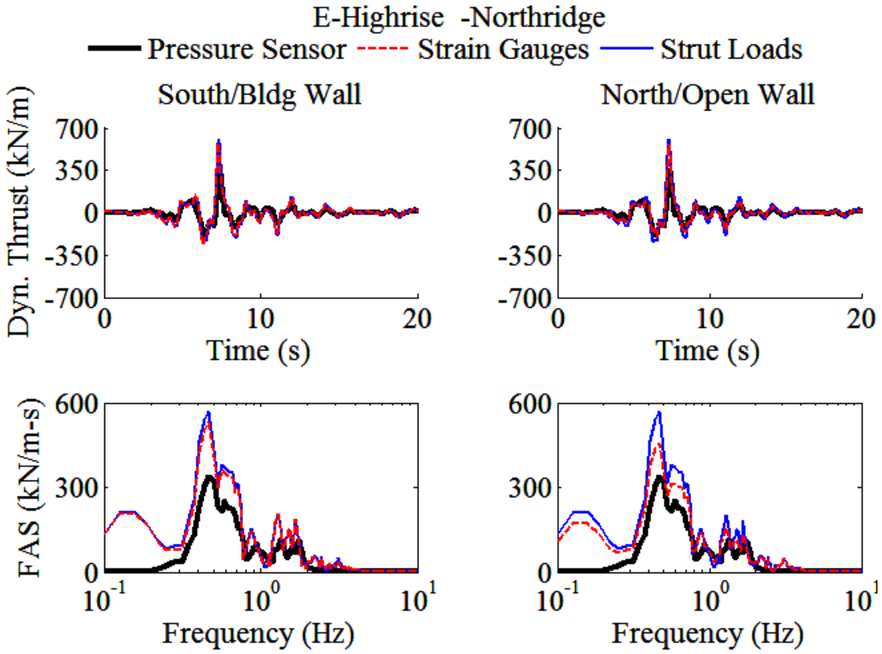

Figure 4-50. Dynamic thrust estimated from pressure sensors, strain gauges, and strut loads shown on both excavation walls during Northridge in E-Highrise represented in the time and frequency domains.

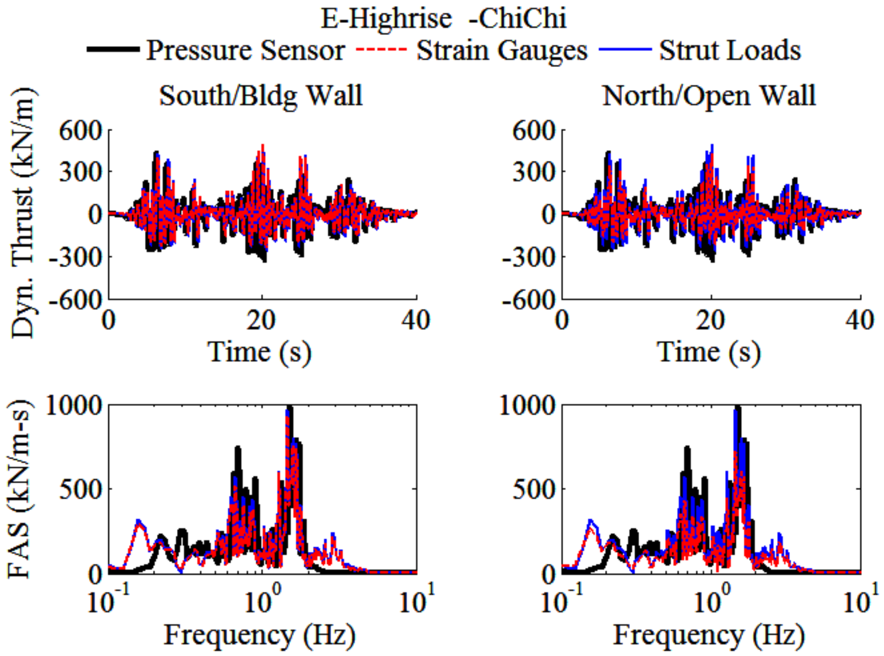

Figure 4-51. Dynamic thrust estimated from pressure sensors, strain gauges, and strut loads shown on both excavation walls during Chi Chi in E-Highrise represented in the time and frequency domains.

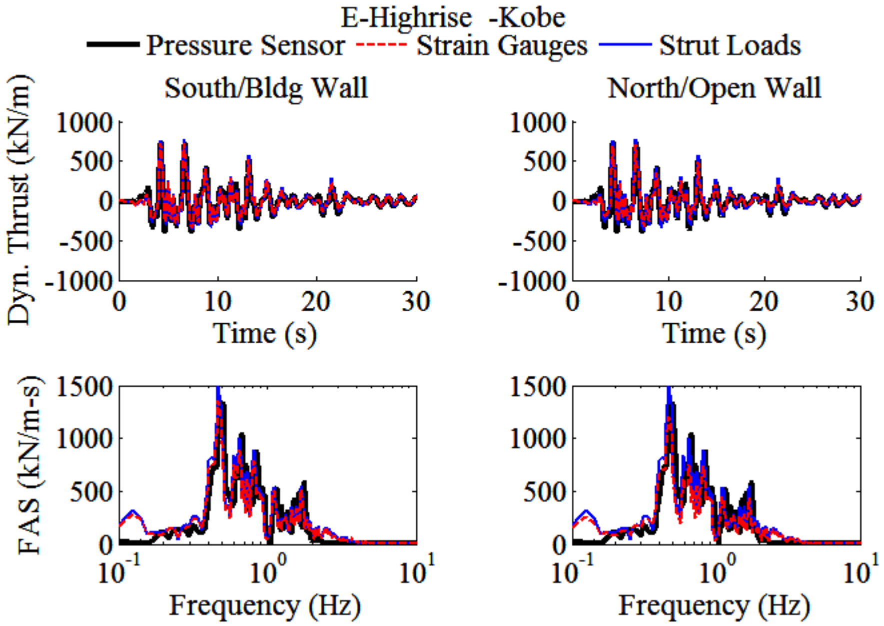

Figure 4-52. Dynamic thrust estimated from pressure sensors, strain gauges, and strut loads shown on both excavation walls during Kobe in E-Highrise represented in the time and frequency domains.

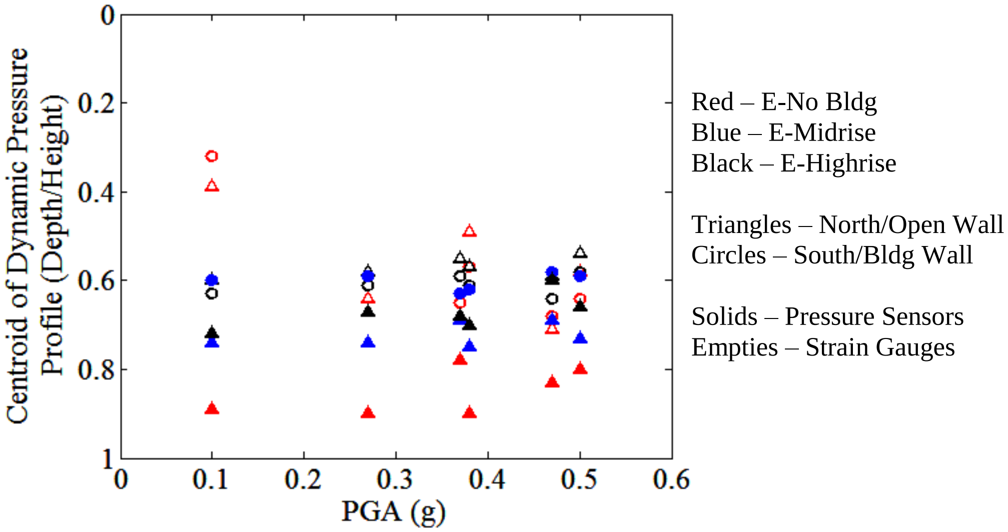

Figure 4-53. Location of the centroid of dynamic pressure profile on both excavation walls, from two methods: tactile pressure sensors and strain gauges, and during the three centrifuge experiments versus base PGA of the input motion.

4.4 Bending and Axial Strains

As shown in the previous sections, the addition of an adjacent building increased lateral earth pressures and total horizontal displacements, while racking displacements were measured to decrease. While these observations were insightful, the bending strains along the excavation walls and the axial strains in the excavation struts are measurements that characterize the overall demand in terms of bending moments and axial forces as well as the overall deflections along the walls.

The strain gauges presented in this section are the same as those used for estimating dynamic thrust in the previous section. Referring back to Figures 3-4, 3-7, and 3-10, SGs 1-20 are used from E-No Bldg, E-Midrise, and E-Highrise along the excavation walls. SGs 32-34 are used to represent the excavation struts in E-No Bldg and SGs 31, 35, 37 in E-Highrise. Again, unfortunately the axial strain gauges in E-Midrise did not save data and are therefore not presented.

Figures 4-54 through 4-57 show bending moment profiles measured along the excavation walls, from the soil surface to the bottom of the walls. Static bending moment profiles are shown before the motion along with the total (static + dynamic) and the dynamic increment of bending moment profiles at the time of maximum dynamic moment on that particular wall. These profiles are shown for E-No Bldg, E-Midrise, and E-Highrise.

The static bending moment profiles were observed to be S-shaped due to the forces from the excavation struts. The bending moments at the top and bottom of the walls were measured to be close to 0. The largest absolute bending moment was measured at a depth near the bottom strut, 9m. The total and dynamic moment profiles were observed to hold a similar shape as the static profiles.

An increase in static bending moment profiles was observed from E-No Bldg to E-Midrise and again from E-Midrise to E-Highrise. The profiles also showed an increase in total and dynamic moment profiles with the addition of an adjacent midrise and highrise buildings. The braced excavation experienced larger demands in terms of bending strains along the excavation walls due to increased thrusts on the excavation walls during the tests with a building. Further, the profiles were roughly similar (symmetric) on the two walls in E-No Bldg. Yet, larger dynamic bending moments were measured above the excavation on the south (building) side compared to the north (open) side with the addition of an adjacent building. These observations and trends are consistent with those from pressure measurements.

Figure 4-58 shows the measurements from axial strain gauges in the excavation struts during E-No Bldg and E-Highrise both in terms of time histories and Fourier amplitude spectra. Axial strain was converted to axial force using Eq 4-13 presented in Section 4.4. Larger static and dynamic axial forces were measured in E-Highrise than E-No Bldg due to the presence of the adjacent tall building. As expected, the bottom strut experienced the largest initial and dynamic forces when compared with the middle and top struts during the same test.

Profiles of axial forces measured on the excavation struts are also presented in Figures 4-59 through 4-61 as static, total, and dynamic increment at the time of maximum axial force during different motions and experiments. Similar conclusions may be made from these plots. In terms of maximum axial forces, the struts in E-Highrise experienced larger demands than E-No Bldg due to the increased load from the adjacent building. The dynamic increment of force was measured to be the largest in the bottom strut and the smallest in the top strut. For many motions, the dynamic force alone seen by the strut was close to the static force, therefore doubling the total force on the strut. This was observed specially on the bottom strut during the stronger motions (e.g.,Northridge and Kobe).

Overall, the bending moments measured on the excavation walls and the axial forces on provide a more holistic story of the seismic response of the braced excavation compared to earth pressures or racking deformations alone. The addition of an adjacent building increased the lateral earth pressures on the underground structure but reduced the deflection of the top of the wall with respect to the base of the foundation (i.e., racking). However, even though insightful, the racking of the braced excavation did not fully describe the deformation shape experienced by the walls and is perhaps not sufficient for design. The excavation walls did not deform completely rigidly or linearly according to the measured bending strains. An adjacent building increased the static and dynamic forces measured on the struts and the excavation walls, showing a greater demand of the retaining system.

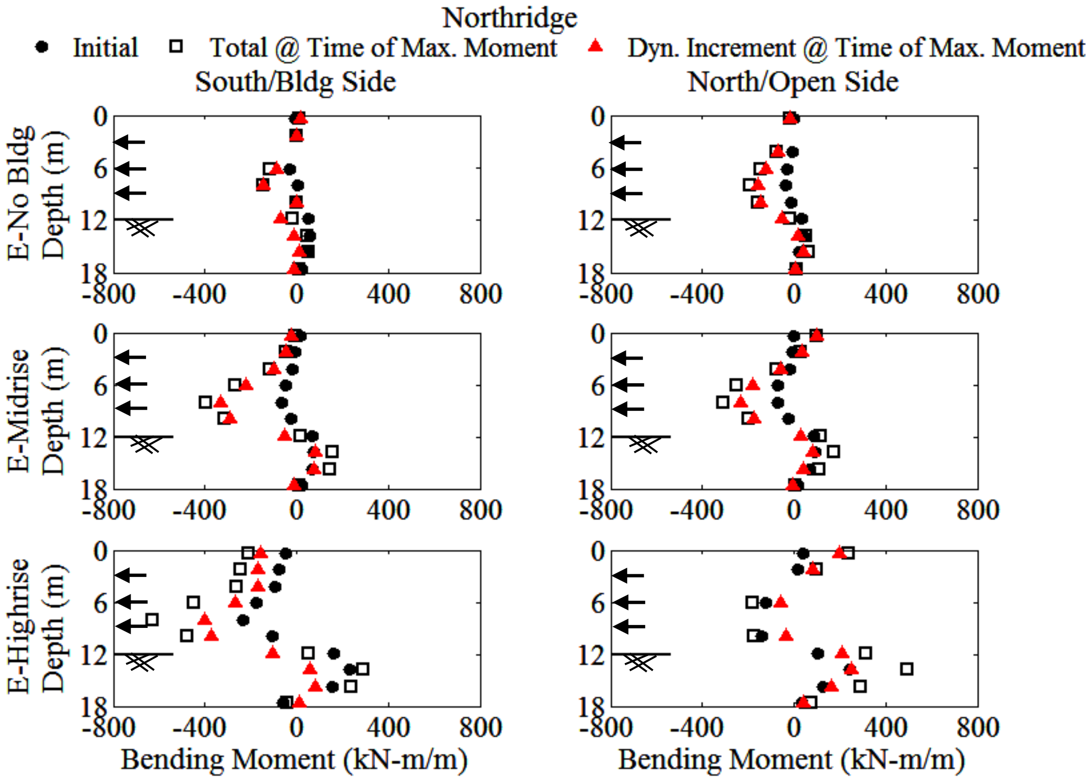

Figure 4-54. Static (before shake), total (static + dynamic), and dynamic increment of bending moment profiles at the time of maximum dynamic moment measured along the two excavation walls during the Northridge motion in E-No Bldg, E-Midrise, and E-Highrise.

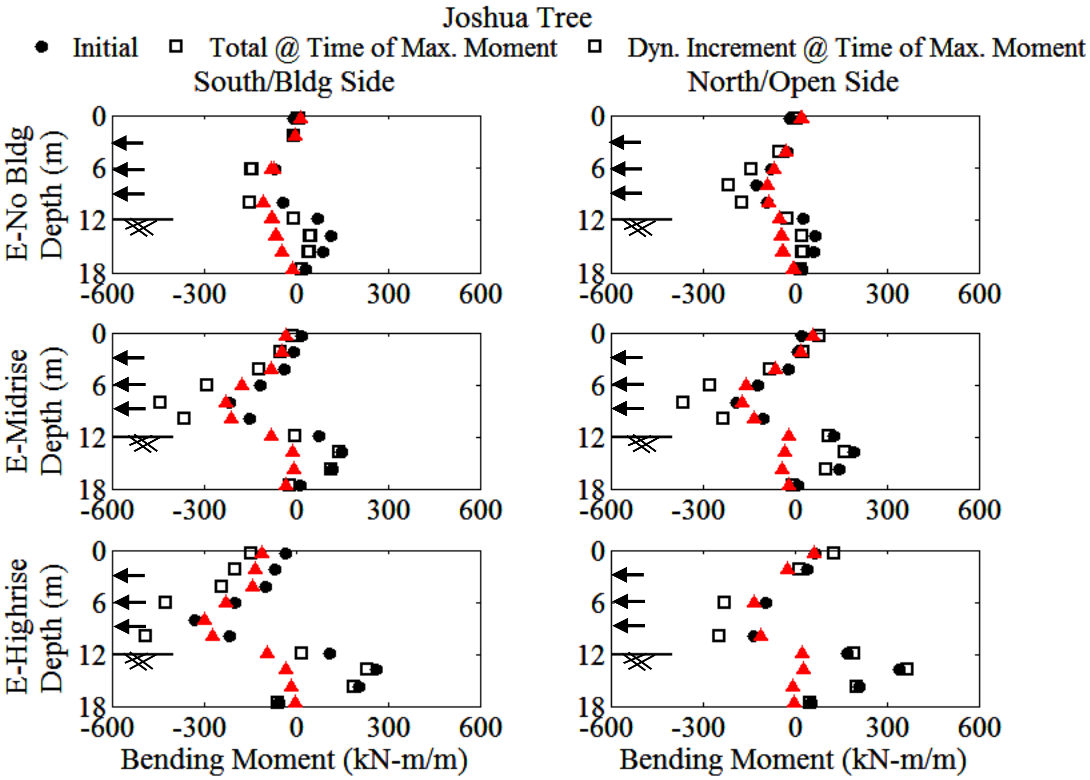

Figure 4-55. Static (before shake), total (static + dynamic), and dynamic increment of bending moment profiles at the time of maximum dynamic moment measured along the two excavation walls during the Joshua Tree motion in E-No Bldg, E-Midrise, and E-Highrise.

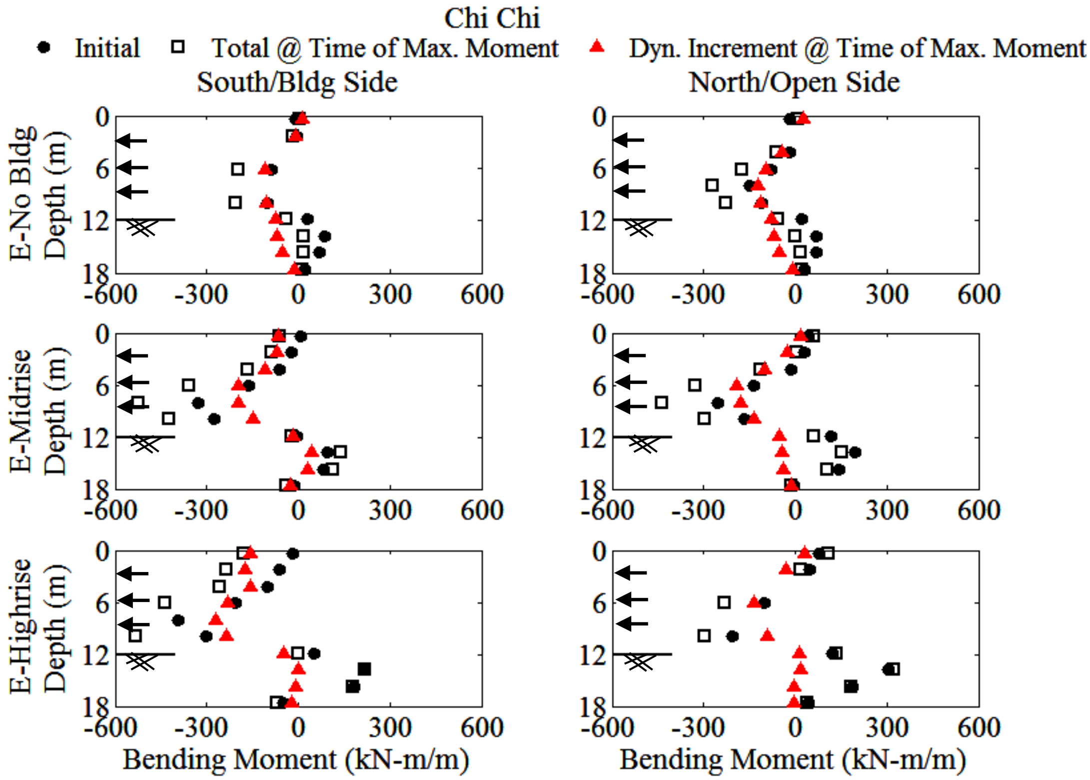

Figure 4-56. Static (before shake), total (static + dynamic), and dynamic increment of bending moment profiles at the time of maximum dynamic moment measured along the two excavation walls during the Chi Chi motion in E-No Bldg, E-Midrise, and E-Highrise.

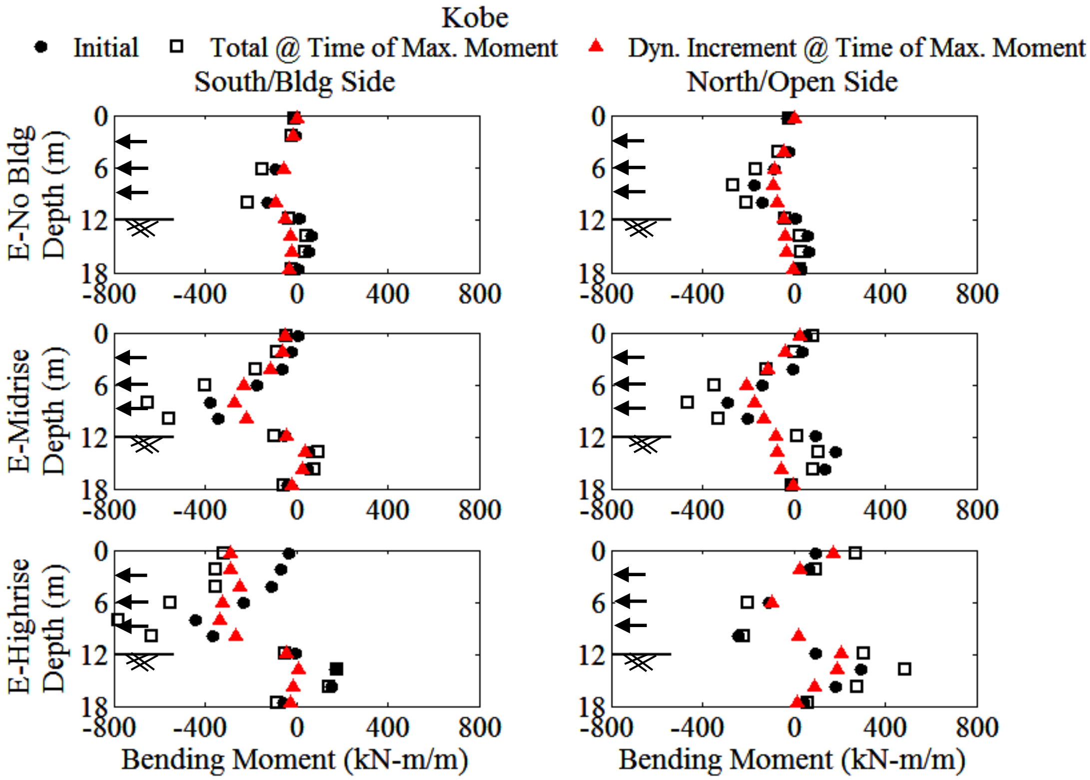

Figure 4-57. Static (before shake), total (static + dynamic), and dynamic increment of bending moment profiles at the time of maximum dynamic moment measured along the two excavation walls during the Kobe motion in E-No Bldg, E-Midrise, and E-Highrise.

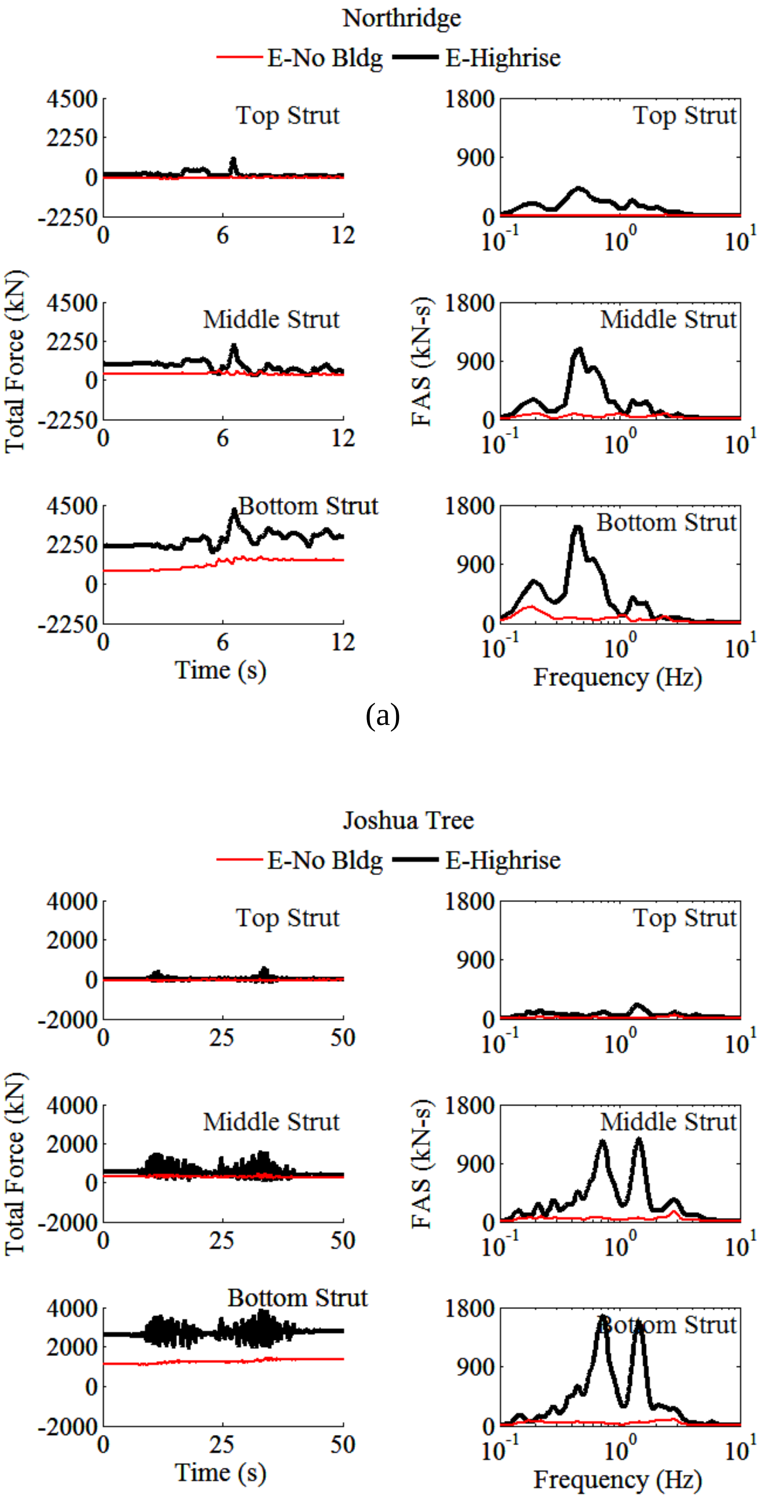

(a)

(b)

Figure 4-58. Total forces measured in the excavation struts: the top, middle and bottom strut, in the time and frequency domains during (a) Northridge and (b) Joshua Tree for E-No Bldg and E-Highrise.

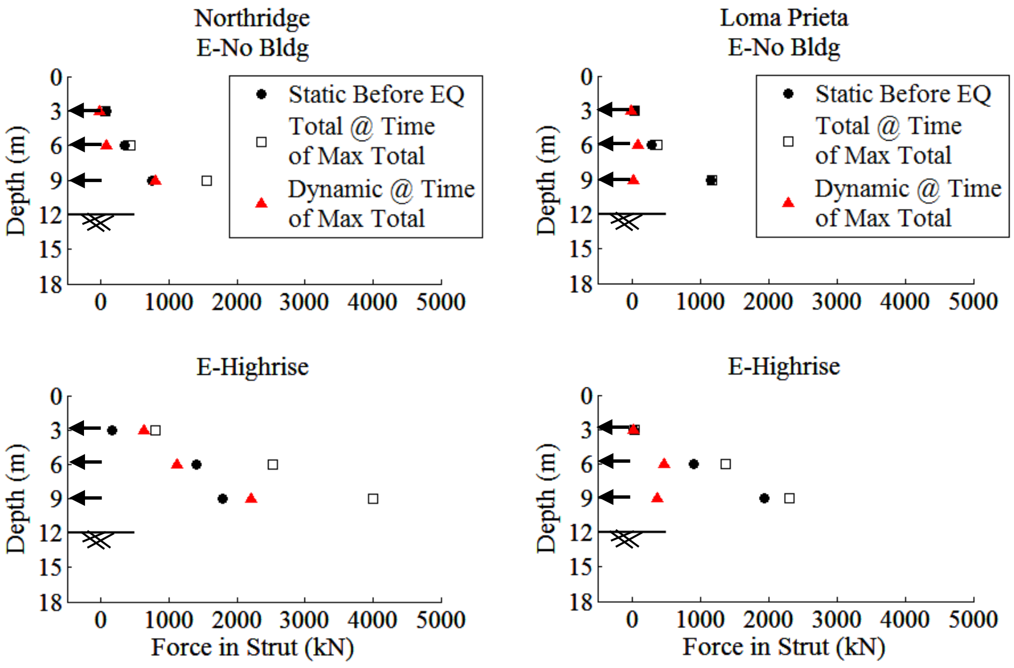

(a)

(b)

Figure 4-59. Static, total (static + dynamic), and dynamic increment of axial forces measured on struts at the time of maximum total force during the: (a) Northridge and (b) Loma Prieta motions in E-No Bldg and E-Highrise

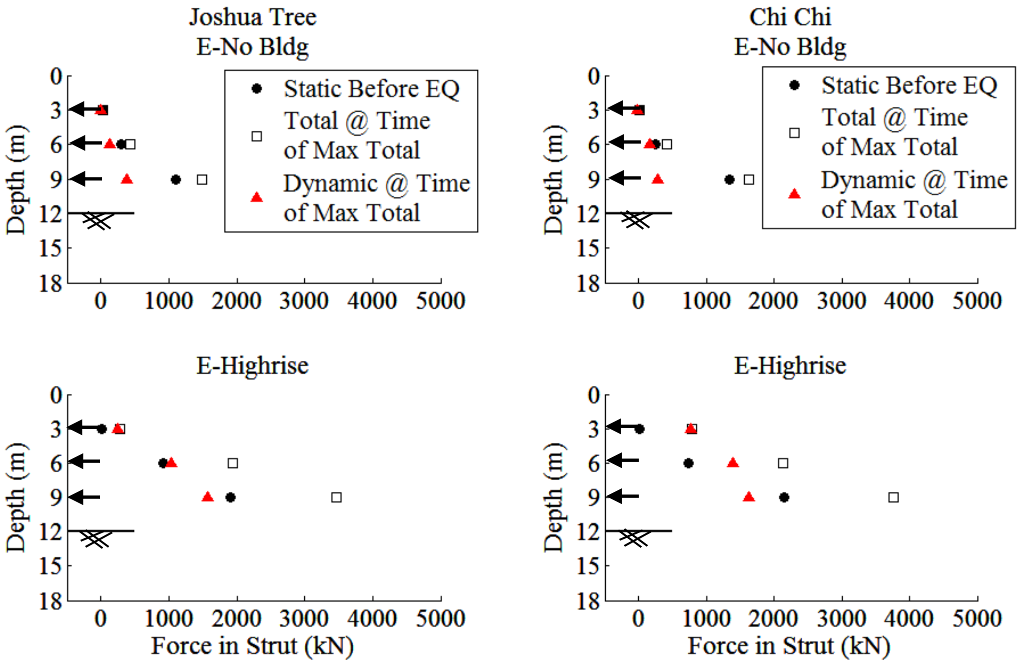

(a) (b)

Figure 4-60. Static, total (static + dynamic), and dynamic increment of axial forces measured on struts at the time of maximum total force during the: (a) Joshua Tree and (b) Chi Chi motions in E-No Bldg and E-Highrise

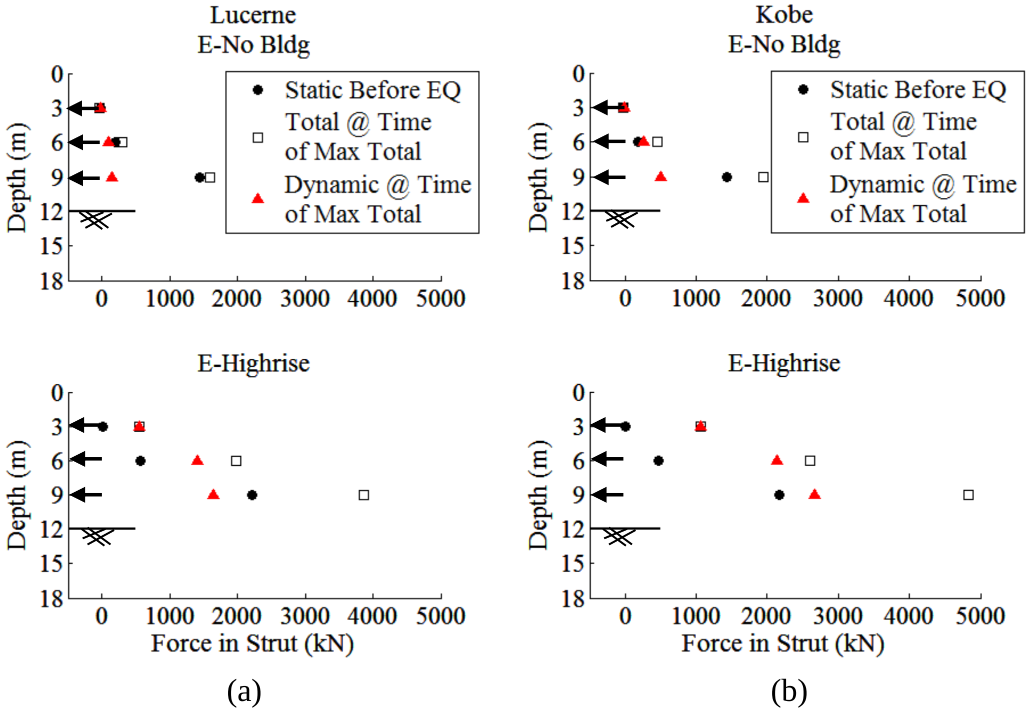

Figure 4-61. Static, total (static + dynamic), and dynamic increment of axial forces measured on struts at the time of maximum total force during the: (a) Lucerne and (b) Kobe motions in E-No Bldg and E-Highrise

5 - DISCUSSIONS AND OBSERVATIONS

5.1 Dynamic Thrust and Building Base Shear

Dynamic thrust on the braced excavation was measured to increase with the addition of the adjacent buildings, especially the highrise building, both when obtained directly from tactile pressure sensors and when computed indirectly from strain gauges. The base shear of the adjacent tall building was hypothesized to be responsible for the majority of this increase in lateral earth pressures. The dynamic thrust calculated from strain gauges and tactile pressure sensors on the south (building) side of the excavation was compared to the base shear of the highrise building to test this hypothesis. Building base shear was calculated from accelerometer recordings of various parts of the building. The highrise building was assumed to carry the majority of its weight in three locations: 1) the basement, 2) the baseplate, and 3) the top mass as shown in Figure 5-1(a). A sum of the acceleration of each part multiplied by the part weight gave the building base shear. For the calculation, A35 was used to represent the basement acceleration, A36 the baseplate, and A38 the top mass, shown in Figure 3-9.

Figures 5-2 through 5-4 compare the base shear of the highrise building to dynamic thrust on the South/Bldg Side of the excavation calculated from strain gauges and pressure sensors for several motions. The comparison is shown in both the time and frequency domains. It must be noted that all records were band-pass filtered for consistency using the same corner frequencies (hence removing any permanent change in the forces), and the inertia of the soil inside the basement was not considered for this comparison. The magnitudes of the two sets of measurements (i.e., dynamic thrust and base shear) were found to be comparable in both time and frequency domains. In other words, the dynamic thrust experienced by the braced excavation in E-Highrise, which was greater than in E-No Bldg, was primarily attributed to the base shear of the adjacent building. The distance between the building and the excavation wall was only 4 m and this transfer of energy was expected.

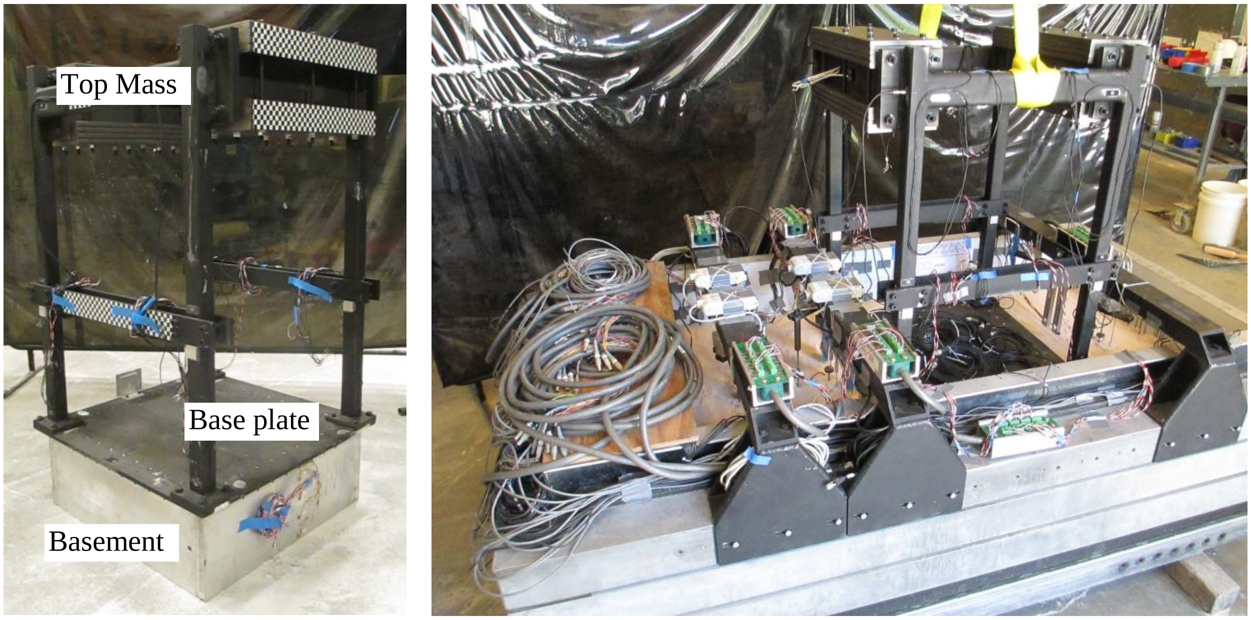

(a) (b)

Figure 5-1. (a) Parts of the highrise building used to calculate building base shear and (b) completed model construction of E-Highrise with the instrumentation in place (including accelerometers used to calculate base shear).

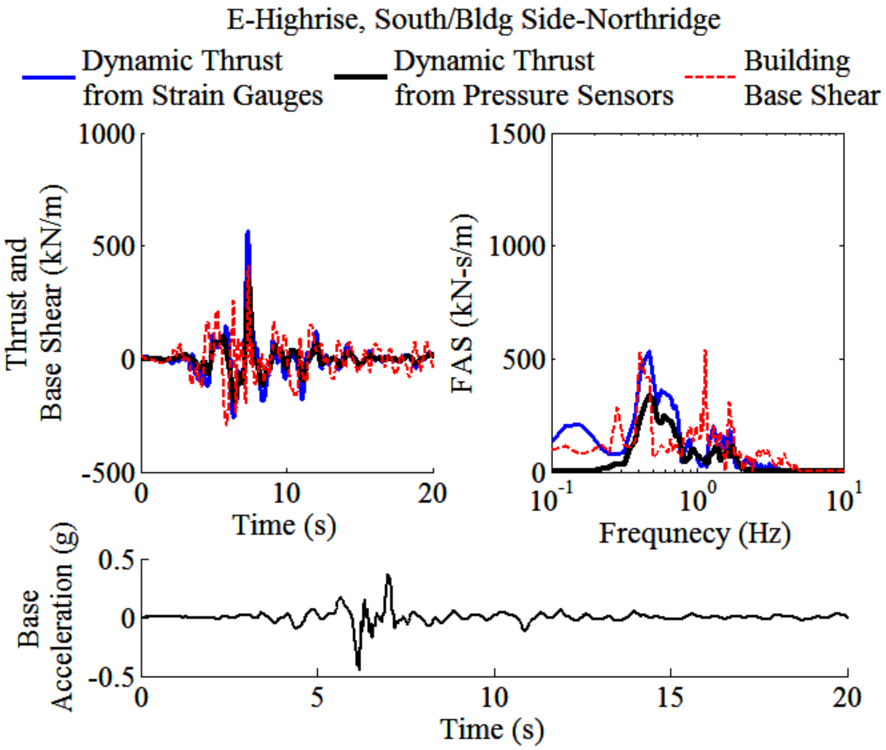

Figure 5-2. Dynamic thrust on the South/Bldg excavation wall measured by pressure sensors and strain gauges compared to the calculated building base shear during Northridge of E-Highrise.

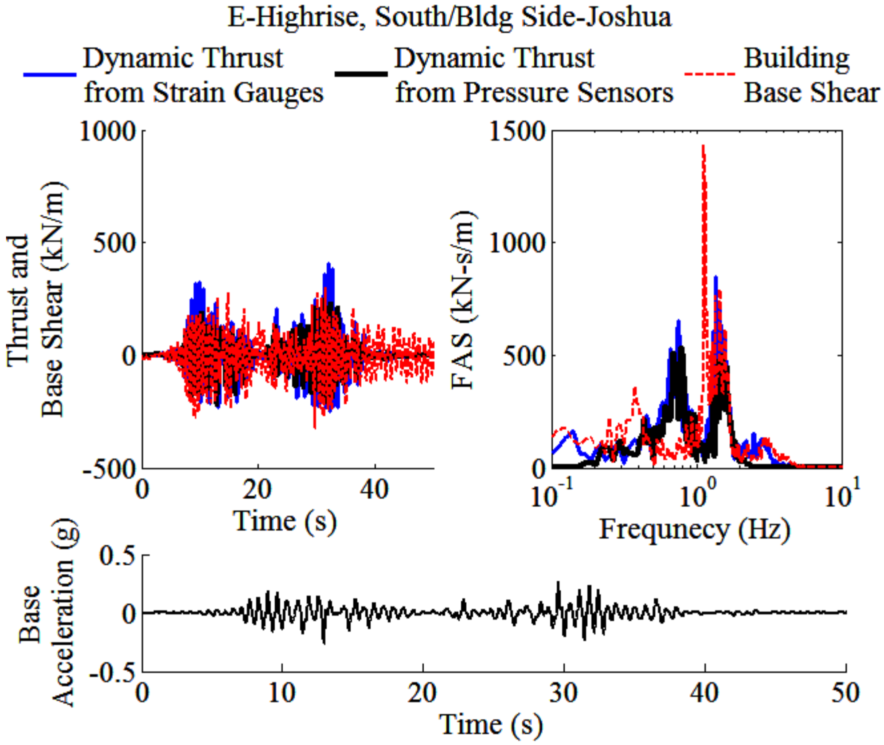

Figure 5-3. Dynamic thrust on the South/Bldg excavation wall measured by pressure sensors and strain gauges compared to the calculated building base shear during Joshua Tree of E-Highrise.

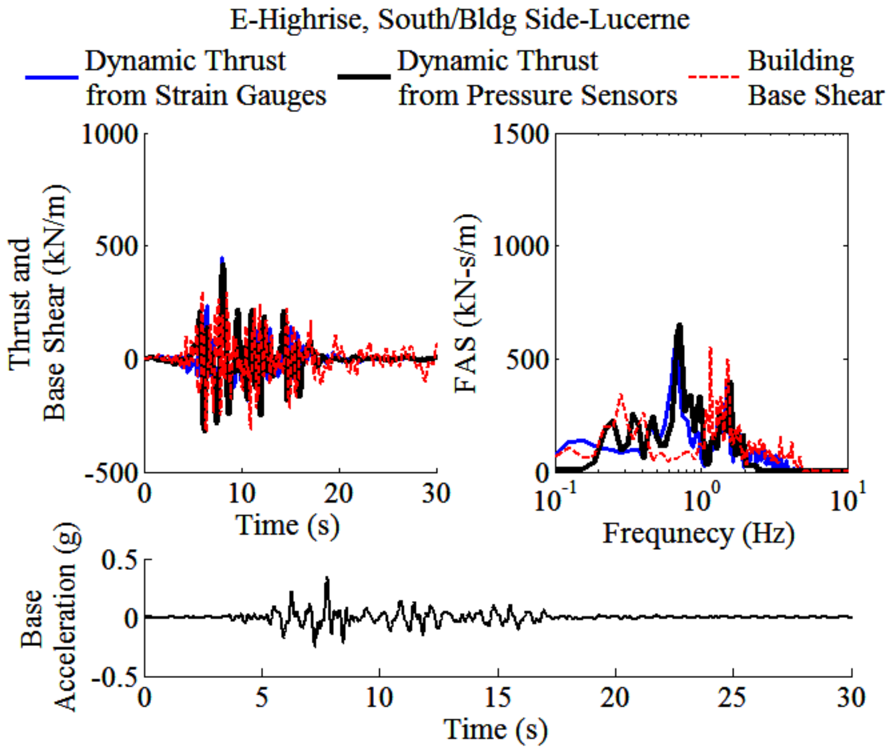

Figure 5-4. Dynamic thrust on the South/Bldg excavation wall measured by pressure sensors and strain gauges compared to the calculated building base shear during Lucerne of E-Highrise.

5.2 Dynamic Thrust and Relative Displacement of the two Structures

To better evaluate SSUSI effects on the observed trends in dynamic thrust, the relative displacement was measured between the two structures and compared with dynamic thrust on the excavation walls in timing and amplitude. The highrise building and excavation did not move all together as a single, in-phase system, and the separation between the two structures varied throughout a given event. Accelerometer recordings were converted to displacement to measure the relative displacement between the excavation wall and the basement of the structure. Accelerometers placed at the mid-height of the highrise basement (A35) and the middle of the South/Bldg excavation wall (A43), shown in Figure 3-9, were used to calculate the average relative displacement between the two structures. In this calculation of displacement, a positive relative displacement implies a movement of the two structures toward each other, decreasing the distance between them, and a negative relative displacement implies the formation of a gap. This relative displacement was compared to dynamic thrust estimated from strain gauges during E-Highrise only. The strain gauge method of obtaining dynamic thrust was selected for this comparison because their data acquisition was time synched with those of accelerometers used to calculate displacement. The results for several motions are shown in Figures 5-12 through 5-15. As expected, the dynamic thrust on the excavation was seen to increase when the distance between the two structures decreased (a positive relative displacement) and decrease when the distance between the structures increased. The comparisons were not as clear during the Northidge motion, however, likely due to the pulse-like nature of this motion.

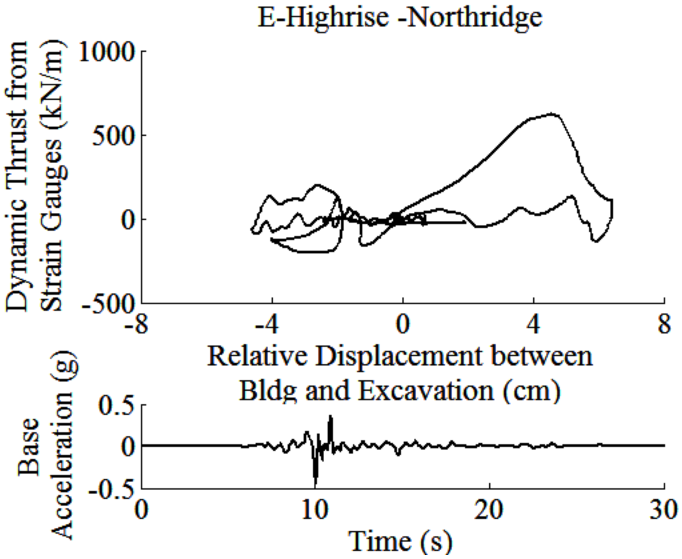

Figure 5-5. Dynamic thrust estimated from strain gauges plotted versus the relative displacement between the basement and excavation wall (mid-depth) during the Northridge motion of E-Highrise (positive rel. displacement implies a decrease in the distance between the two structures).

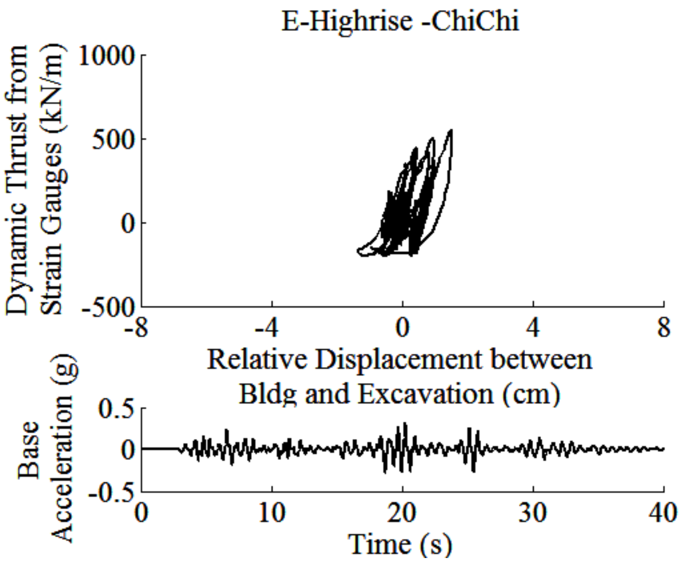

Figure 5-6. Dynamic thrust estimated from strain gauges plotted versus the relative displacement between the basement and excavation wall (mid-depth) during the Chi Chi motion of E-Highrise (positive rel. displacement implies a decrease in the distance between the two structures).

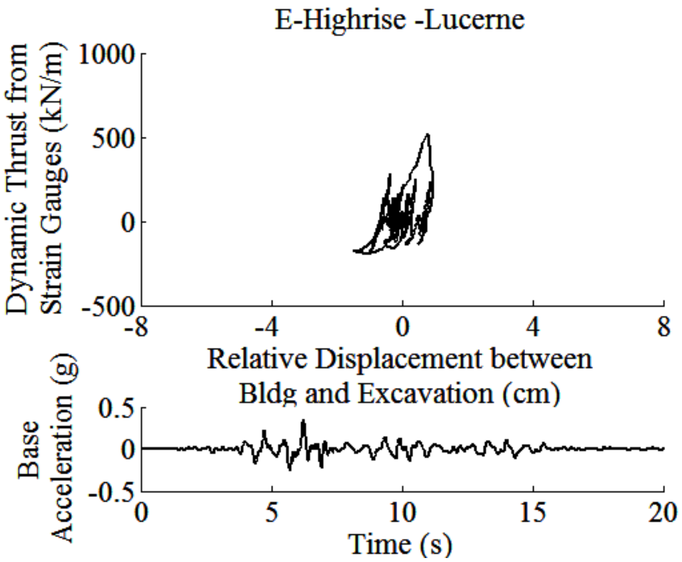

Figure 5-7. Dynamic thrust estimated from strain gauges plotted versus the relative displacement between the basement and excavation wall (mid-depth) during the Lucerne motion of E-Highrise (positive rel. displacement implies a decrease in the distance between the two structures).

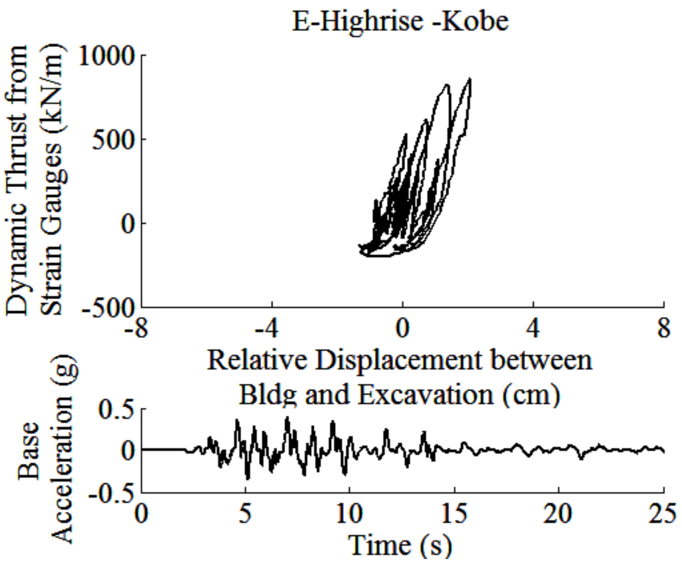

Figure 5-8. Dynamic thrust estimated from strain gauges plotted versus the relative displacement between the basement and excavation wall (mid-depth) during the Kobe motion of E-Highrise (positive rel. displacement implies a decrease in the distance between the two structures).

5.3 Dynamic Thrust and Racking Displacements

Even though the dynamic thrust was measured to increase with the addition of the adjacent building, racking displacement was measured to actually decrease. This was especially observed for the South/Bldg wall that was constrained by the adjacent tall building. Figures 5-5 through 5-8 show how racking displacements vary with dynamic thrust estimated by strain gauges during several motions in E-No Bldg and E-Highrise. Positive racking corresponds to movement to the north or away from the building. The cyclic plots show an accumulation of thrust when the wall experienced a racking displacement toward the adjacent building. When the wall racked away from the building, dynamic thrust was measured to decrease. Many of the other previous observations are confirmed in these figures also. Dynamic thrust is shown to have increased from E-No Bldg to E-Highrise. Racking decreased with the addition of the building, especially on the South/Bldg Side of the excavation.

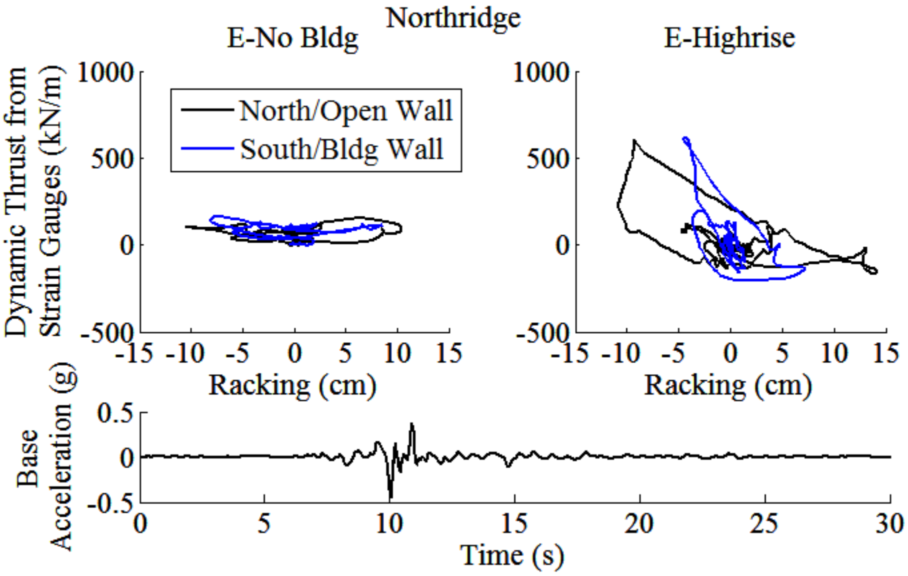

Figure 5-9. Dynamic thrust estimated from strain gauges plotted versus excavation racking on the two excavation walls during the Northridge motion of E-No Bldg and E-Highrise.

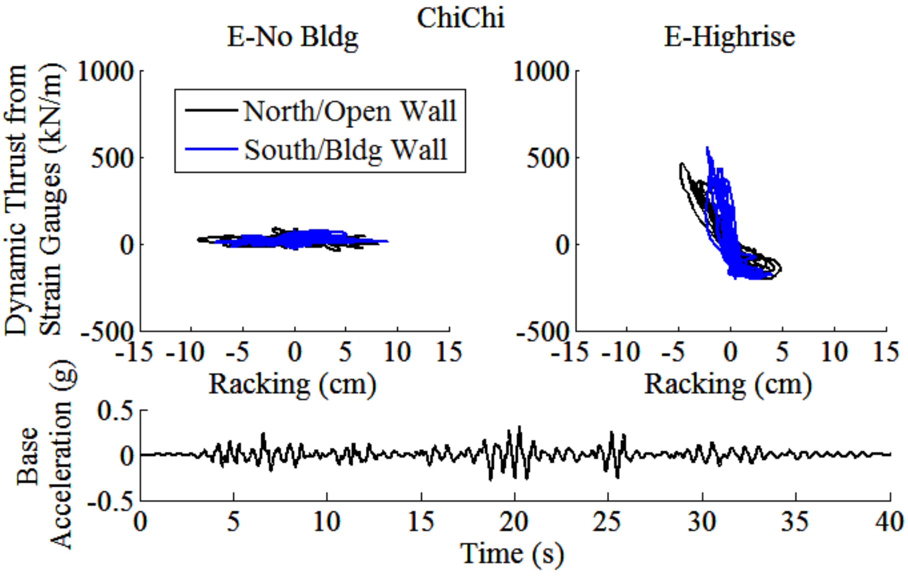

Figure 5-10. Dynamic thrust estimated from strain gauges plotted versus excavation racking on the two excavation walls during the Chi Chi motion of E-No Bldg and E-Highrise.

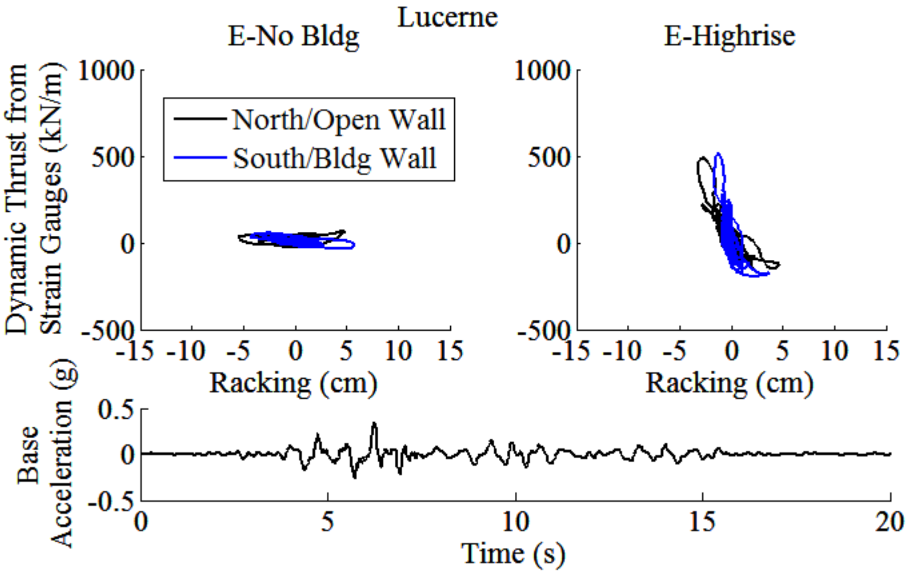

Figure 5-11. Dynamic thrust estimated from strain gauges plotted versus excavation racking on the two excavation walls during the Lucerne motion of E-No Bldg and E-Highrise.

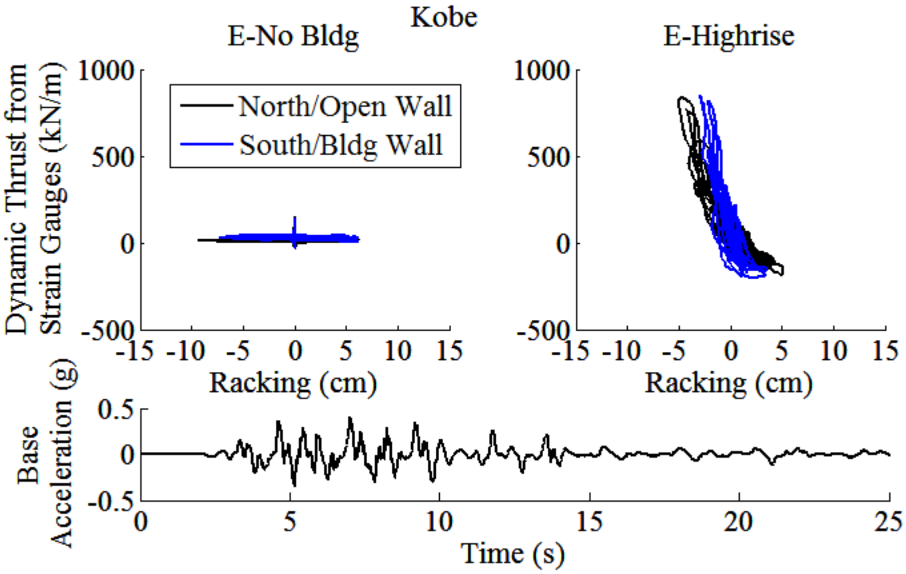

Figure 5-12. Dynamic thrust estimated from strain gauges plotted versus excavation racking on the two excavation walls during the Kobe motion of E-No Bldg and E-Highrise.

5.4 Dynamic Thrust and Bending Moments

As discussed previously, racking displacements maybe more insightful when the wall undergoes a nearly rigid-body rotation. It may therefore not be a sufficient measurement of the performance of braced excavations when they undergo S-shaped deflections. Bending strains in the walls and axial strains in the struts measured larger demands and deflections with the addition of the building while the simplistic racking displacements alone showed an overall improved seismic performance of the retaining system. Figures 5-9 through 5-11 compare absolute dynamic bending moments on the South/Bldg Wall at a sensitive depth of 10 m with dynamic thrust estimated from strain gauges on the same wall. These figures also compare the measured dynamic axial forces on the bottom strut with dynamic thrust during several motions in E-No Bldg and E-Highrise. Absolute dynamic bending moment and dynamic axial forces generally increased in the braced excavation with the addition of the building, in phase with the increase in dynamic thrust.

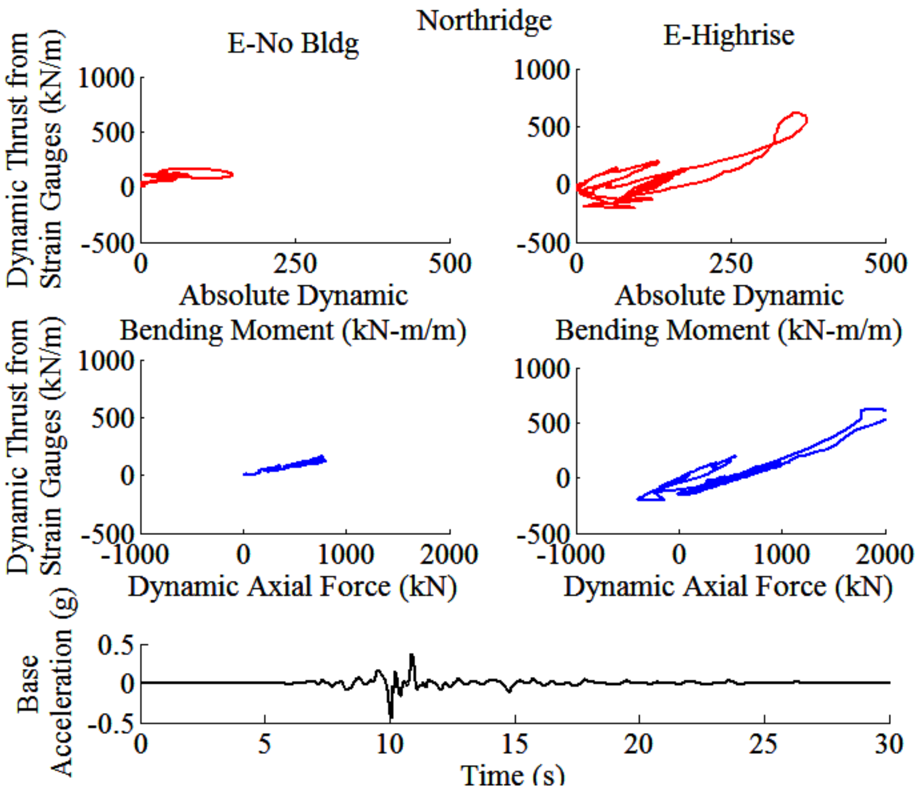

Figure 5-13. Dynamic thrust estimated from strain gauges plotted versus absolute dynamic bending moments on the South/Bldg excavation wall at a sensitive depth of 10m and versus the dynamic axial force on the bottom strut during the Northridge motion E-No Bldg and E-Highrise.

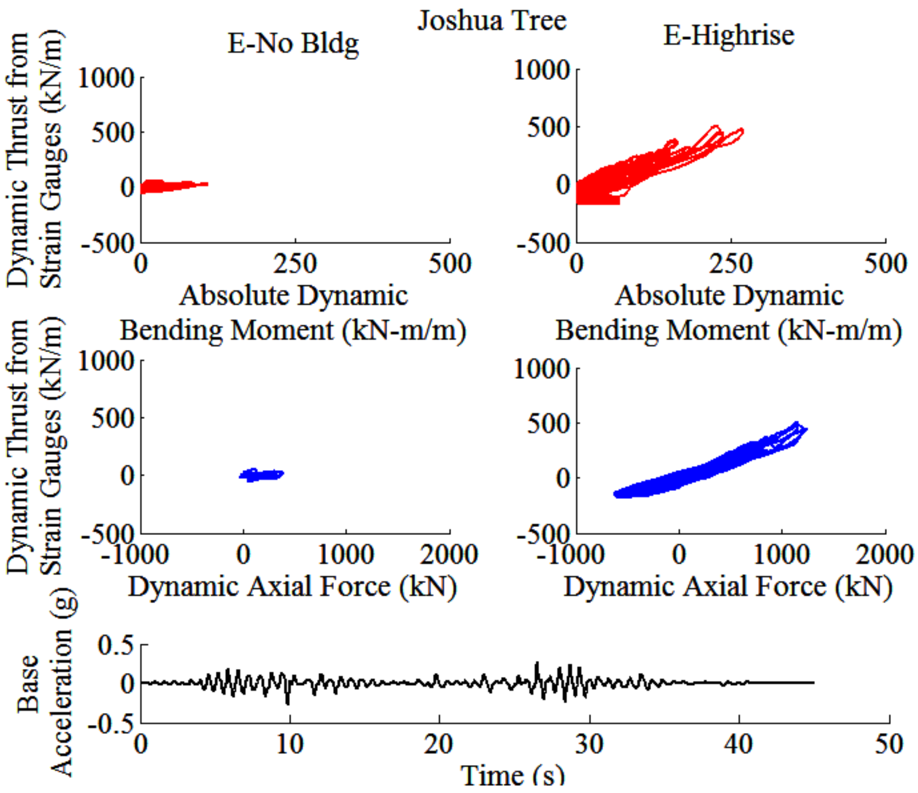

Figure 5-14. Dynamic thrust estimated from strain gauges plotted versus absolute dynamic bending moments on the South/Bldg excavation wall at a sensitive depth of 10m and versus the dynamic axial force on the bottom strut during the Joshua Tree motion E-No Bldg and E-Highrise.

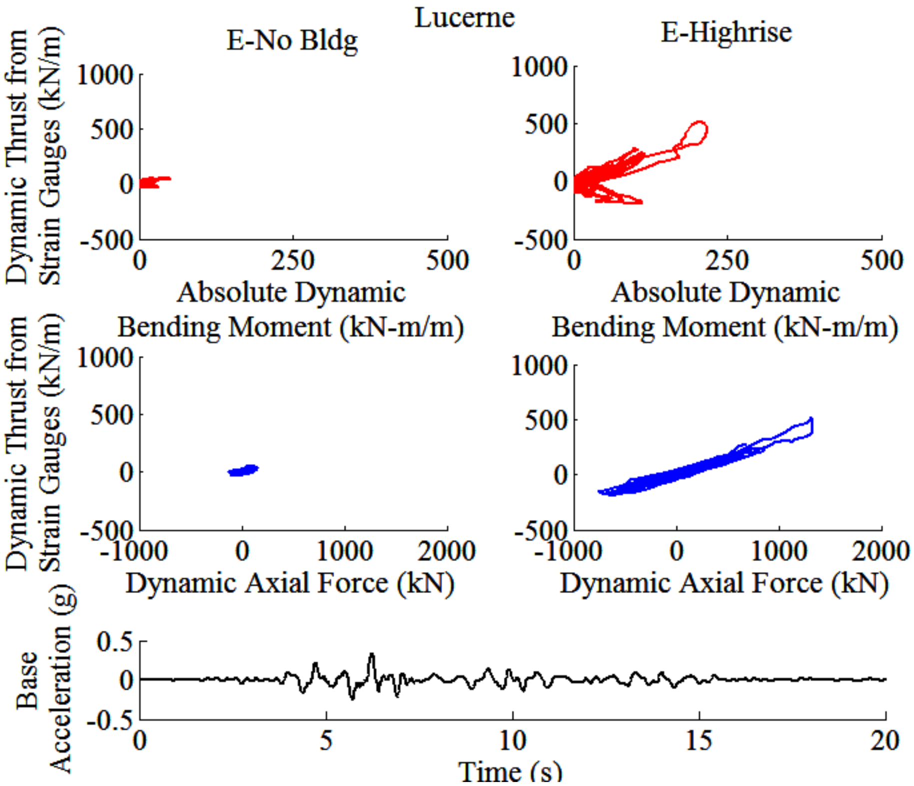

Figure 5-15. Dynamic thrust estimated from strain gauges plotted versus absolute dynamic bending moments on the South/Bldg excavation wall at a sensitive depth of 10m and versus the dynamic axial force on the bottom strut during the Lucerne motion E-No Bldg and E-Highrise.

6 - CONCLUSIONS AND FUTURE RESEARCH NEEDS

The primary objective of this MS thesis is to experimentally investigate the influence of an adjacent mid to highrise building on the seismic performance of a braced excavation. The current state of practice for the seismic design of underground structures relies either on simplified procedures that do not consider an adjacent building or advanced numerical tools that have not been validated against physical model studies. The goal of this research is to address this gap and evaluate soil-structure-underground structure-interaction (SSUSI) via centrifuge modeling for the specific case of temporary braced excavations near tall buildings founded in medium-dense, dry sand. It must be noted that recommendations for design should not exclusively look at experimental data. Results from numerical simulations currently being performed by University of Illinois will be considered in conjunction with these experimental observations to provide recommendations to be used in practice.

The first centrifuge test conducted in this study, E-No Bldg, provided a baseline experiment to study the response of a braced excavation in isolation undergoing a sequence of 1D earthquake motions with varying characteristics. In the second two experiments, E-Midrise and E-Highrise, a midrise and a highrise building was added adjacent to the excavation, respectively, while keeping other parameters the same. For a proper comparison of results across the three tests, the achieved base motions and the far-field, small-strain properties of medium-dense sand were compared among the three tests and were found to compare reasonably well.

The seismic performance of the braced excavation was evaluated in terms of three design parameters during the three experiments: 1) racking and average wall displacements, 2) seismic lateral earth pressures on the walls, and 3) dynamic bending moments on the walls and axial strains on the struts. Racking deformation was defined as the horizontal displacement of the top of the wall with respect to the base of the excavation. Total earth pressures were measured directly using tactile pressure sensors and indirectly using bending strain gauges along the wall and axial strain gauges on the struts. Observations were made in terms of these three design parameters, in order to evaluate the influence of an adjacent building.

It was shown that absolute average displacements along the two excavation walls were roughly similar with and without the adjacent building, with a slight increase observed during E-Highrise. However, racking displacements of both excavation walls decreased with the addition of the midrise building and decreased again with the adjacent highrise building. Further, the presence of an adjacent building made the deformation patterns along the two walls asymmetric (more deflection occurring on the open side compared to the building side of the excavation). Even though the overburden pressure had increased, the underground structure was constrained from racking-type deformations in E-Midrise and E-Highrise compared to E-No Bldg due to the presence of the building.

The static earth pressures obtained from one direct method (i.e., tactile sensors) and two indirect methods (i.e., bending strain gauges and axial strain gauges) were seen to increase with the addition of a building, especially during E-Highrise. Although there was more variation and scatter in static earth pressures obtained from the three methods, the dynamic pressures compared well. Dynamic earth pressures increased with the addition of an adjacent midrise or highrise building. The dynamic thrust measured from strain gauges was roughly similar on the two walls even when a building was present on one side creating asymmetric loading. The location of the resultant dynamic thrust varied between 0.2H and 0.5H from the bottom of the excavation, where H is the height of the excavation. The location of this centroid was observed to be independent of the intensity of shaking, but the presence of the adjacent building seemed to move the centroid up, closer to 0.4H.

Racking deformations are an important measure of the deflection and seismic performance of the underground structure, particularly when it undergoes a nearly rigid-body rotational movement. However, these relatively flexible excavation walls with struts were not observed to deform completely rigidly, as shown by strain gauges. The dynamic bending moments along both walls and the axial forces experienced on the struts increased with the addition of the adjacent buildings. Also, during the tests with a building, larger dynamic bending moments were measured on the South/Bldg Side compared to the North/Open Side, particularly in E-Highrise during events toward the end of the earthquake series. Even though racking decreased with the presence of a building, dynamic earth pressures increased, and these increased earth pressures were translated into greater bending along the entire wall and greater axial forces on the struts. Therefore, the results indicate that racking deformations, although useful, are not sufficient measures of the performance of these types of underground structures.

The insight from the series of centrifuge experiments presented in this thesis is useful in evaluating the influence of tall buildings on the seismic performance of shallow underground structures. Parallel numerical simulations are currently underway by the research team which will help solidify these conclusions so design recommendations can be made. Further, this study focused on simplistic soil, structure, and underground structure configurations in order to evaluate SSUSI fundamentally for the first time in centrifuge. Future studies are needed to evaluate the influence of variations in soil properties and saturation in addition to the impact of more complex loading conditions (e.g., multidirectional seismic loading) on SSUSI.

7 - REFERENCES

Al Atik, L. F. (2008). “Experimental and Analytical Evaluation of Seismic Earth Pressures on Cantilever Retaining Structures,” Ph.D. Dissertation, Department of Civil and Environmental Engineering, University of California, Berkeley.

Arango, Ignacio (2008). "Earthquake engineering for tunnels and underground structures. A case history.," In: David Zeng, Majid T. Manzari, and Dennis R. Hiltunen, Eds., Geotechnical Earthquake Engineering and Soil Dynamics IV. Sacramento, CA: ASCE.

Baldi, G, R Bellotti, VN Ghionna, M Jamiolkowski, and DCF LoPresti (1989). “Modulus of sands from CPTs and DMTs,” Proc., 12th International Conference of Soil Mechanics and Foundation Engineering, Vol. 1, Rio de Janeiro, pp. 165-170.

Bardet, J.P., Huang, Q., and Chi, S.W. (1993). “Verification of Numerical Procedures for the Analysis of Soil Liquefaction Problems,” Proceedings, Verification of Numerical Procedures for the Analysis of Soil Liquefaction Problems ’93, Davis, Californica.

Darendeli, M. B. (2001). "Development of a new family of normalized modulus reduction and material damping curves," Civil Engineering. Austin: University of Texas at Austin, 395.

Dashti, S., Gillis, K., Ghayoomi, M., and Hashash, Y. (2012). “Sensing of Lateral Seismic Earth Pressures in Geotechnical Centrifuge Modeling.” Proceedings of the 15th World Conference on Earthquake Engineering, Lisbon, Portugal, 1-10.

Gillis, K., Dashti, S., Hashash, Y. (2015). “Dynamic Calibration of Tactile Sensors for Measruement of Soil Pressures in Centrifuge,” ASTM Geotechnical Testing Journal, 38(3), 1-14.

Hardin, B.O. and Drnevich, V.P. (1972). “Shear modulus and damping in soils: measurement and parameter effect.” Journal of the Soil Mechanics and Foundations Division, ASCE, Vol. 98, No. SM 6, pp. 603-624.

Hashash, Y. M. A., J.J. Hook, B Schmidt, and J. I-C. Yao (2001). "Seismic design and analysis of underground structures," Tunneling and Underground Space Technology, Vol. 16, 247-293.

Hashash, Y.M.A., Karina, K., Koutsoftas, D., O’Riordan, N. (2010). “Seismic Design Considerations for Underground Box Structures.” Engineering Research. University of Illinois at Urbana-Champaign.

Jamiolkowski, M.,Leroueil, S., and LoPresti, D.C.F.(1991). “Theme lecture: Design parameters from theory to practice.” Proceedings, Geo-Coast ’91, Yokohama, Japan, pp. 1-41.

Menq, F. –Y. (2003). “Dynamic properties of sandy and gravely soils,” Ph.D. Dissertation, Department of Civil and Environmental Engineering, University of Texas at Austin.

Mikola, R. G., (2012). “Seismic earth pressures on retaining structures and basement walls in cohesionless soils”. Ph.D. Dissertation, Dept. of Civil and Environmental Engineering, University of California, Berkeley.

Nakamura, S., Yoshida, N., Iwatate, T., 1996. Damage to Daikai Subway Station During the 1995 Hyogoken-Nambu Earthquake and Its Investigation. Japan Society of Civil Engineers, Committee of Earthquake Engineering, pp. 287

Piratheepan, P. (2002). “Estimating shear wave velocity from SPT and CPT Data. Master of Science Thesis, Clemson University.

Peck, R.B. (1969) “Deep excavations and tunneling in soft ground”, in Proc. 7th Internation Conference SMFE, Mexico (State of the Art Volume), Mexican Society SFME, pp. 225-281

Romero Arduz, M.I., Hashash, Y., Dashti, S., Ghayoomi, M. (2015). “Evaluation of 1-D Seismic Site Response Modeling of Sand using Centrifuge Experiments.” Soil Dynamics and Earthquake Engineering Journal (under review).

Seed, H.B. and Idriss, I.M. (1970). “Soil moduli and damping factors for dynamic response analyses,” Report EERC 70-10, Earthquake Engineering Research Center, University of California, Berkeley.

Wang, J.N. (1993). "Seismic sesign of tunnels: a state-of-the-art approach," Monograph 7. New York, NY: Parsons Brinckerhoff Quade & Douglas, Inc.

Wu, C. L., and J. Penzien (1994). "Seismic design of muni metro turnback project," Fifth U. S. National Conference on Earthquake Engineering. Chicago, IL, 799-808.